NON-INVASIVE CARDIOVASCULAR HEALTH MONITORING FOR PATIENTS WITH HEART FAILURE USING SEISMOCARDIOGRAPHY

A Dissertation
Presented to
The Academic Faculty

By

Md Mobashir Hasan Shandhi

In Partial Fulfillment
of the Requirements for the Degree
Doctor of Philosophy in the
School of Electrical and Computer Engineering

Georgia Institute of Technology

December 2020

NON-INVASIVE CARDIOVASCULAR HEALTH MONITORING FOR PATIENTS WITH HEART FAILURE USING SEISMOCARDIOGRAPHY

Approved by:

Dr. Omer T. Inan, Advisor
School of Electrical and Computer Engineering
Georgia Institute of Technology

Dr. Farrokh Ayazi
School of Electrical and Computer Engineering
Georgia Institute of Technology

Dr. David Anderson
School of Electrical and Computer Engineering
Georgia Institute of Technology

Dr. Liviu Klein
School of Medicine
University of California, San Francisco

Dr. Thomas Plötz
School of Interactive Computing
Georgia Institute of Technology

Date Approved: November 25, 2020

Nothing goes unpaid.

To my parents, my brother, my wife and my kid

ACKNOWLEDGEMENTS

Almost all the achievements in my life are a direct and indirect contribution from my parents, Md Yeakub Hossain Mia and Meherun Nessa. Their support and encouragement throughout my lifelong journey so far have given me the courage and motivation to pursue my lifelong dreams. Apart from my parents, my brother, Muhammed Mubashir Hossain, has always supported me in my life in thick and thin. I would like to thank my extended family members and in-laws for their constant support and understanding.

It is said that a Ph.D. is not just a degree but a journey to become an independent researcher, thinker, or, to be more precise, an independent human being. The mentor during this journey is as or even more important than the journey itself, as he/she can guide you through this incredible journey of self-reckoning, learning, and maturing your thoughts. I was fortunate to have Dr. Omer T. Inan as my Ph. D. supervisor and learn how to be a good researcher and a good human being overall. His support, empathy, welcoming nature, encouragement, understanding, and multi-tasking abilities have no bounds. I have been very blessed to work with him in person since the start of my Ph.D. back in 2016. He has taught me from a very small thing of preparing a figure for research presentation to critical thinking of the overall aspect of the research projects. I could not have asked for a better environment and a better person to work with during my Ph.D.

I would also like to thank Dr. Liviu Klein, the clinical supervisor in most of the research projects that I was involved in during my Ph.D. His clinical guidance and interests in the technical side of the sensor and machine learning algorithm development helped me pursue different routes in research during my Ph.D. I would like to thank my other committee members, Dr. Farrokh Ayazi and Dr. David Anderson, for their valuable feedback for both my proposal and final thesis. I was lucky to work with Dr. Ayazi in a couple of projects with the MEMS sensors from his lab in our biomedical research projects. I would like to thank Dr. Thomas Plötz for his time to serve in my thesis committee and his guidance on the machine learning aspects of the collaborative works I have been doing with him. I would definitely miss the witty group meetings I had with him.

I wish to thank all the current and past members of the Inan Research Lab (IRL), who made this group such a friendly and supportive environment altogether. I would like to thank especially Dr. Sinan Hersek, who taught me with hands-on experience in my initial years in the lab and to be a place to discuss my under-developed ideas to get his constructive feedback. I was blessed to work with a bunch of superstars from the IRL, Dr. Caitline Teague, Dr. Hazar Ashouri, Dr. Maziyar Pouyan, Dr. Daniel Whittingslow, Dr. Nick Bolus, Dr. Andrew Carek, Dr. Nil Gurel, Dr. Jon Zia, Dr. Mohsen Safaei, Beren Semiz, Hewon Jung, Hyeong Ki Jeong, Varol Burak Aydemir, Venu Ganti, Jacob Kimball, Oludotun Ode, Sevda Gharenhbagi, Kristy Scott Richardson, Asim Gazi and the newer members of the lab. Our lab would not have been such an epitome of research and innovation without your presence and contribution.

I would also like to thank my other collaborators Dr. Mazziyar Etemadi and Alex Heller, from Northwestern University, Joanna Fan and Sean Dowling from the University of California San Francisco, and my clinical collaborators from the Emory University. I was very privileged to work in multiple interdisciplinary, innovative works due to this incredible group of people.

Outside of my professional works during my Ph.D., I was lucky to be involved with the Bangladesh Student Association at Georgia Tech, who became my friends and family out of Bangladesh. We enjoyed planning, organizing, and performing in various cultural events and outdoor activities. Also, my life here in Atlanta will forever be engraved in my mind due to the birth of our first kid, Auronya Mobashir. He grew up seeing his mother and father going through graduate studies and research without any other family members taking care of him in the foreign land. The journey of fatherhood and my Ph.D. journey was symbiotic to one another for the last four years of my life.

Lastly, I would like to thank my lovely wife, Nusrat Asrafi, without whose relentless support, my Ph.D. would not have been possible. Going through pregnancy, raising our son, looking after our family's needs, and on top of that continuing her graduate studies and research show that she is superhuman, and I am very lucky to have her in my life in my best and in my worst as well. Though Ph.D. is a journey of a graduate student, my journey was not mine alone. It was an unforgettable journey for all three of us: my kid, wife, and me.

TABLE OF CONTENTS

LIST OF TABLES

LIST OF FIGURES

SUMMARY

Heart failure (HF) is the leading cause of hospitalization and hospital readmission for patients aged over 65 and older in the United States, with roughly one in five individuals hospitalized with heart failure being readmitted within 30 days of discharge. HF affects 6.2 million Americans with health care costs of almost $31 billion per year. Management of HF is a complicated process that requires frequent clinic visits and outpatient management systems for hemodynamic monitoring and patient-reported symptoms. Hemodynamically guided HF management via tracking pulmonary congestion and taking proactive care have shown efficacy in reducing HF-related readmission significantly. However, the cost-prohibitive nature of such pulmonary congestion monitoring systems precludes their usage in the large patient population affected by HF. For that reason, an inexpensive alternative is necessary to bring hemodynamic monitoring systems to the large patient population affected by HF, not only in the United States but also around the world.

Advancement of novel biomedical sensor technologies and advanced signal processing and machine learning algorithms have merit in tracking health parameters unobtrusively. A promising sensing modality is seismocardiography (SCG), defined as the measurement of local chest wall vibrations associated with the cardiac cycle. SCG has shown efficacy in tracking changes in cardiac contractility via the cardiac timing intervals it yields, such as the pre-ejection period (PEP). However, different sensing modalities of SCG acquisition exist using accelerometer and gyroscope based sensors, and inter-subject variability of these acquired signals has made it challenging to develop a robust hemodynamic monitoring system using SCG. Accordingly, most researches in the field of SCG focus on advancing the understanding and processing of the signal in healthy individuals. The translation of the SCG-based hemodynamic monitoring approaches into the actual patient population, for example, in patients with HF, is necessary to validate such a system for both inpatient and outpatient HF management.

This work addresses some of these key aspects. First, the two sensing techniques for acquiring SCG, accelerometer and gyroscope sensors, are compared in their ability to track cardiac contractility changes via PEP estimation. Second, general time, frequency, and amplitude features are extracted from the SCG signals and used in a population level machine learning regression algorithm to estimate key cardiovascular features for healthy subjects and patients with HF, by overcoming the inter-subject variability of the signals. Third, the SCG sensing system, along with the signal processing and machine learning algorithm, is verified and validated with two gold-standard clinical procedures: cardiopulmonary exercise test (CPX) and right heart catheterization (RHC). Gas exchange variables from the CPX and changes in pulmonary congestion from the RHC procedures were estimated using features from simultaneously recorded SCG signals to demonstrate the efficacy of such a sensing system and algorithm to track relevant hemodynamic parameters in patients with HF.

The algorithms and methods presented in this work can enable remote cardiovascular health monitoring for patients with HF to enable personalized titration of care, and improving medication adherence in a hemodynamically-guided HF management system. The inexpensive wearable sensing technology has the potential to be a viable and ubiquitous alternative to the already-proven hemodynamic congestion monitoring systems, which can improve the quality of life and outcome in patients with HF by reducing hospitalization and reducing the overall health care costs.

CHAPTER 1

INTRODUCTION

1.1 Motivation and Background

As an outcome of improved health care systems and lower mortality rates, life expectancy is growing rapidly worldwide. The aging population (aged 65 or older) is projected to grow from an estimated 524 million in 2010 to nearly 1.5 billion in 2050, with most of the increase in developing countries [1]. This growing aging population needs frequent and longitudinal health care for various diseases such as cardiovascular diseases (CVDs), respiratory complications, cancers, and neurological disorders. CVDs, including heart failure (HF), are consistently ranked as the number one cause of death in the United States (US) and contribute to approximately 6 million deaths per year [2] with an annual cost of \$30.7 billion, mainly due to hospitalization costs [3]. The difficulty of HF management is attributed not only to a high rate of HF-related admissions—approximately 1 million per year in the US [4]—but also as the leading cause of hospital readmission for patients aged 65 and older [5]. It is projected that the total direct medical costs due to HF with all CVDs will increase from \$396 billion in 2012 to \$918 billion in 2030 [6].

Due to the high 30-day readmission rate and associated health care cost related to HF, the Hospital Readmissions Reduction Program (HRRP), under the Affordable Care Act (ACA) passed in March 2010, identified HF among the three targeted conditions (acute myocardial infarction and pneumonia being the other two) to reduce hospitalization. The HRRP program sought to penalize hospitals with higher rates of readmission for these three targeted conditions to reduce unnecessary hospital costs [5]. While this policy may have led to a reduction in HF 30-day readmissions (readmissions for HF declined from 23.5% in 2008 to 21.4% in 2014) [7, 8], much of that reduction may have been due to administrative re-classification or upcoding of patients [8]. In addition, early independent studies suggest that penalizing hospitals for higher 30-day HF readmissions led to an increase in 30-day, 90-day, and 1-year risk-adjusted HF mortality [9]. Finally, two large randomized trials, one with only HF patients and the other with medically and socially complex patients with a history of hospitalization, failed to demonstrate the utility of care transition programs to decrease hospital admissions [10, 11]. For this reason, the health care systems and cardiologists are exploring novel implanted or wearable technologies to assist in HF management in addition to hospital readmission reduction penalties and hospital-to-home care transitions [12].

HF management is a unique and critical task that requires frequent hospital visits and recurrent monitoring from clinicians. However, frequent monitoring by clinicians is not enough to mitigate the impact of HF. For this reason, clinicians are exploring implantable and non-invasive biosensors to monitor these affected patient populations both in hospital and at home [13, 12]. Clinicians have explored different outpatient home monitoring techniques for patients with HF that include daily weight monitoring and telemonitoring of patient-reported symptoms [11, 14], implantable bioimpedance monitors [15, 16], non-invasive bioimpedance monitors [17], natriuretic peptides [18], implantable hemodynamic sensors [19, 20, 21], and non-invasive lung fluid congestion monitoring [22]. Unfortunately, except for the direct measurement of intracardiac filling pressures and non-invasive lung fluid congestion monitoring, no other approaches for outpatient HF monitoring has successfully shown improvement in outcomes for patients with HF in large randomized controlled trials [13, 23, 15, 22].

An implantable pressure sensor, CardioMEMS (CardioMEMS HF System, Abott, Chicago, IL, USA), was one of the first hemodynamic monitoring systems for tracking the pulmonary artery pressure and volume status in HF patients, and has shown efficacy in reducing HF-related rehospitalization by 30% [24] and was approved by the FDA in 2014. CardioMEMS has shown the importance of tracking filling pressure (via tracking changes in pulmonary congestion) of the heart as an early predictor of the progression of compensated hemodynamically stable HF patient to a symptomatic acute decompensated HF patient, as shown in Fig. 1.1. For that reason, by sensing the increased filling pressure of the heart, the clinicians can have more time to titrate the necessary set of medications to reduce the underlying congestion and alternate the course of decompensation in affected the individuals.

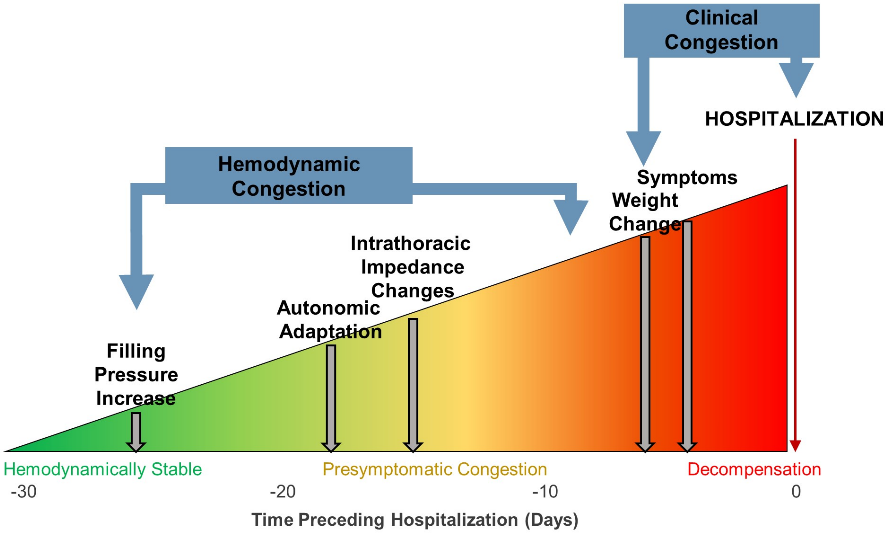

Figure 1.1: Progression of Heart Failure Pathophysiology. Adapted from [25]

Another pulmonary congestion monitoring system that has shown efficacy in HF management is the Remote Dielectric Sensing Technology (ReDS, Sensible Medical Innovations Ltd.; Netanya, Israel), a non-invasive technology that uses a wearable vest with tissue dielectric measurement capabilities to quantify lung fluid concentration [22]. Similar to CardioMEMS, ReDS technology aims to identify worsening pulmonary vascular congestion prior to the development of overt clinical symptoms. It uses the differences and ratios of dielectric coefficients in pulmonary tissue (i.e., the ratio of fluid to air) to create a sensitive and direct indicator of fluid concentration in the lungs [26]. A study of 50 patients showed that ReDS-guided HF management may reduce readmissions for patients discharged after acute decompensated HF [22]. The results of a larger randomized study of 268 patients were presented in 2019 and showed that ReDS-guided HF management prevented 48% of HF readmissions [27]. Furthermore, there are current studies underway to examine whether ReDS technology can guide inpatient decision-making regarding readiness for the discharge of HF patients [28].

Although both CardioMEMS and ReDS systems have shown efficacy in reducing HF-related readmission, the high-cost associated with each technology (> \$25,000 for CardioMEMS and \$43,000 for ReDS) make them financially infeasible solutions of HF management for the large population affected with HF, both in the US and around the world. Thus, the development of inexpensive cardiovascular health monitoring devices, which can track hemodynamic parameters effectively in the hospital and at home, can help in HF management, improve the quality of life of the affected individuals and potentially reduce the costs of care. Fig. 1.2 illustrates a wearable sensor ecosystem that can enable remote cardiovascular health monitoring system for patients with HF.

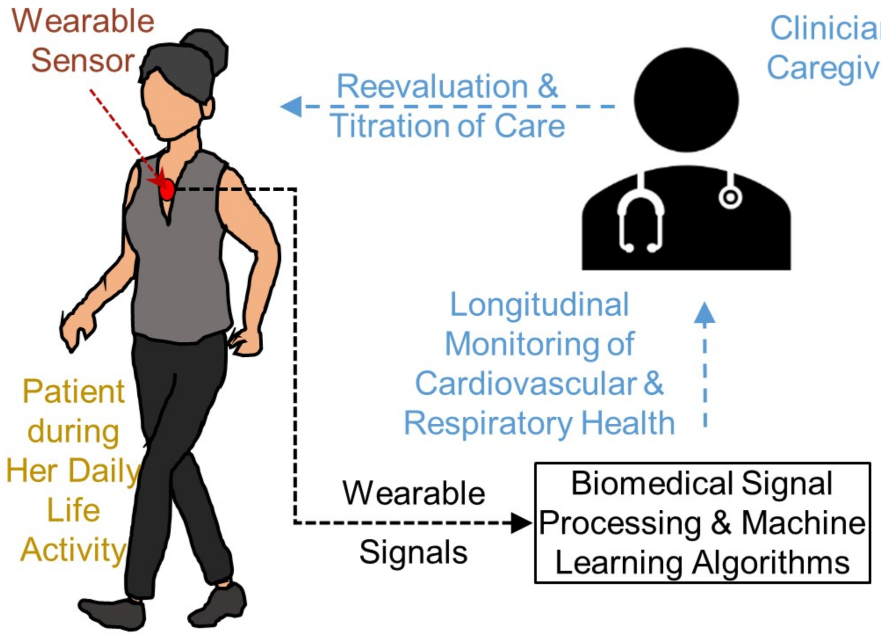

Figure 1.2: Concept of a wearable cardiovascular health monitoring system to enable remote longitudinal monitoring of patients with cardiovascular and respiratory diseases, and cancer survivors by: (1) recording wearable signals during daily life activities and exercise, (2) processing the signals and estimate relevant physiological variables and (3) enabling physicians/caregiver to intervene based on the longitudinal assessment of cardiovascular health.

1.2 Specific Aims and Contributions

The ultimate goal of this work is to develop and validate a wearable sensor to monitor cardiovascular health for patients with HF by (1) investigating different modalities of wearable sensing systems to track changes in hemodynamics with physiological and pharmacological perturbation, (2) developing robust signal processing and machine learning algorithm to extract clinically relevant features from these wearable signals by overcoming the inter-subject variability of the signals, and (3) validating the wearable sensor and algorithms to track clinical parameters in patients with HF against gold-standard clinical procedures. To achieve these goals in a systematic way, the work has three specific aims:

1. To analyze the performance of different wearable sensors and robust population-level regression model in estimating changes in cardiac contractility via pre-ejection period (PEP) estimation.
2. To estimate exercise capacity and exercise intolerance using a wearable sensor in patients with HF to stratify risks associated with HF.
3. To track changes in intracardiac and pulmonary pressures with pharmacological perturbation using a wearable sensor in patients with HF to track hemodynamics non-invasively.

1.3 Thesis Organization

Chapter 2 and 3 provide the scientific background of the work while **Chapters 4-6** present original research. Finally, **Chapter 7** presents the conclusions and future direction of the work. Specifically, **Chapter 2** provides the physiological background of the cardio-pulmonary system and the pathophysiological changes of the heart with HF. **Chapter 3** provides a brief overview of different wearable sensing systems to monitor cardiovascular health. **Chapter 4-6** are organized in order of the specific aims of the work mentioned above. Last of all, **Chapter 7** presents the conclusions and future direction of the work.

CHAPTER 2

CARDIOVASCULAR PHYSIOLOGY

2.1 Anatomy of the Heart

The heart is located in the middle of the chest, slightly to the left of the sternum, and it has four chambers and four valves, as shown in Fig. 2.1. The two upper chambers are the two atria, and the two lower chambers are the two ventricles. Out of the four valves, two are atrioventricular (AV), and two are semilunar (pulmonary and aortic) valves. The valve between the right atrium and right ventricle is the tricuspid valve, and the valve between the right ventricle and pulmonary artery is the pulmonary valve. The valve between the left atrium and left ventricle is the mitral valve, and the valve between the left ventricle and aorta is the aortic valve.

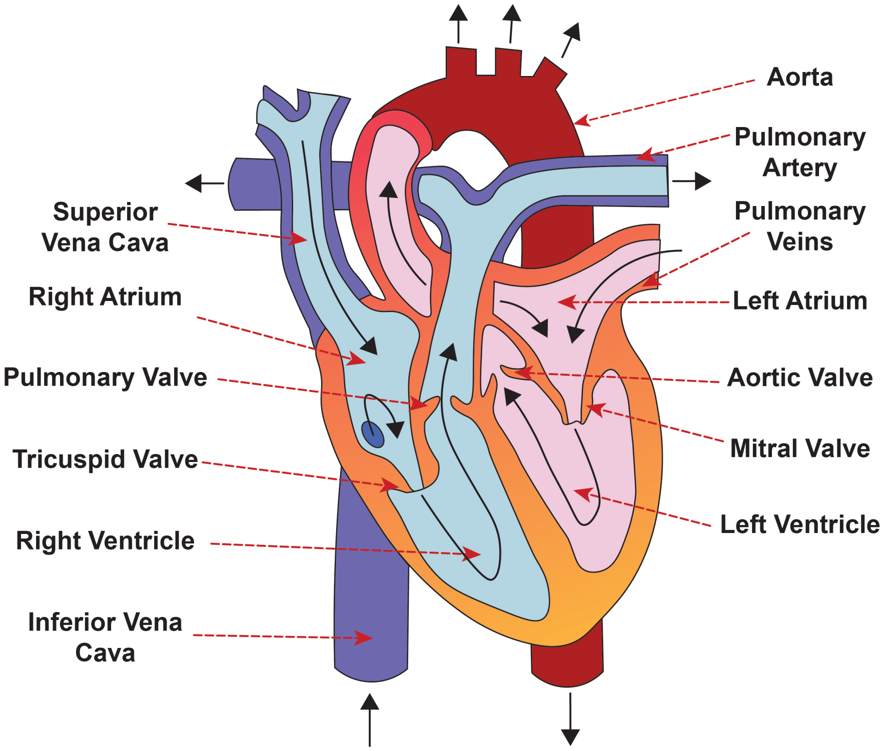

Figure 2.1: Anatomy of the heart with black arrows showing the blood flow.

The heart pumps blood to different organs of the body through an intricate network of arteries, capillaries, and veins, known as the cardiovascular system. It is connected to the lungs through the pulmonary artery and veins, known collectively as the pulmonary circulation. The right side of the heart (right atrium and right ventricle) receives blood from the venae cavae (the largest veins of the body) and sends the blood to the lungs. The blood returns back to the left side of the heart (left atrium and left ventricle) and flows to other parts of the body except for the lungs. The circulation from the left side of the heart flows to the whole body and its return back to the right side is known as the systemic circulation. Fig. 2.2 shows the systemic and pulmonary circulation of the blood. The blood with low O_2 concentration and high CO_2 concentration returns back to the right atrium of the heart through the superior and inferior venae cavae, which goes through the right ventricle to the lungs through the pulmonary artery. The blood receives oxygen from the alveoli in the lungs and returns back to the left atrium through pulmonary veins. It travels through the mitral valve to the left ventricle, and when the left ventricle contracts, it pumps out through the aortic valve to the aorta and the other organs of the body.

2.2 Cardiac Cycles and Cardiac Timing Intervals

The cardiac cycle of the heart is broadly divided into two phases: diastole, the filling phase, and systole, the ejection phase. Diastole and systole may be subdivided into four phases: 1) Isovolumetric relaxation, 2) Ventricular filling (further subdivided into two sub-phases: passive and active filling), 3) Isovolumetric contraction, and 4) Ventricular Ejection. The cardiac cycle is depicted in Fig. 2.3.

The cardiac cycle begins with the isovolumetric relaxation (diastole) phase when both the ventricles are relaxed, and both the AV and semilunar valves are closed. During the second phase of ventricular filling, blood starts to flow from the atria to the ventricles passively since the pressure in the ventricles is lower than the ventricles. This early phase of ventricular filling is also known as the rapid filling/inflow phase. As the ventricles are

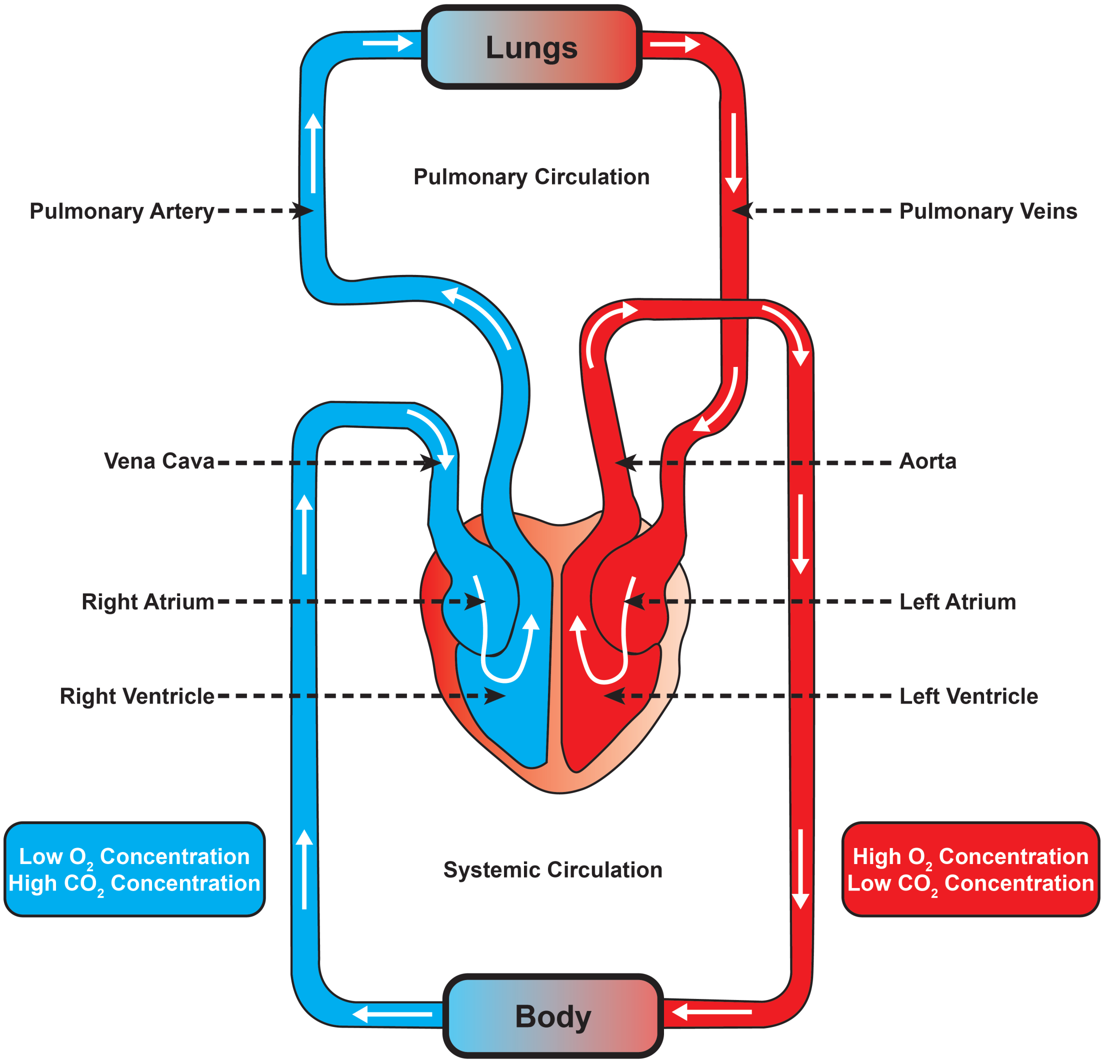

Figure 2.2: Systemic and pulmonary circulation of blood, with white arrows showing the direction of blood flow.

filling, the pressure in the ventricles increases and the flow of the blood decreases, which is known as diastasis. At the end of the ventricular filling phase, the atria contracts and the remaining blood flows to the ventricles, which is known as atrial systole or atrial “kick”. At the end of this ventricular filling phase, the AV valves close, and the heart enters into the isovolumetric contraction (IVC) phase. In the IVC phase, the ventricles start to contract. The pressure increases to match the pressure of the aorta/pulmonary artery. When it reaches the pressure, the semilunar valves open, and blood flows to the aorta and pulmonary artery

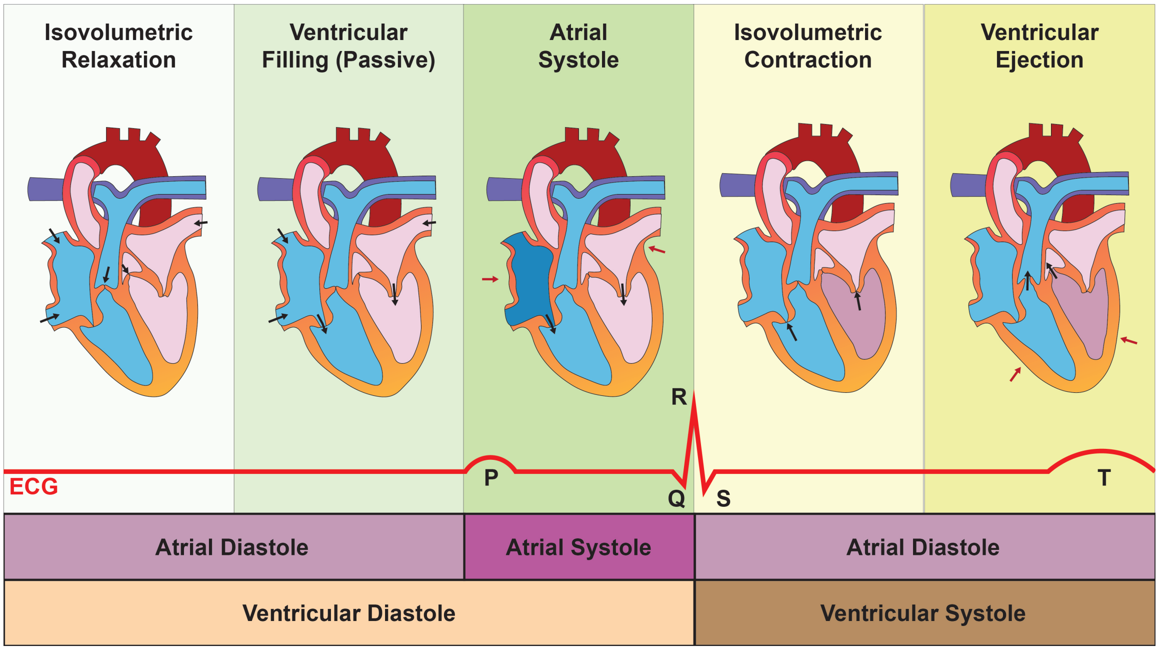

Figure 2.3: The cycle diagram depicts one heartbeat of the continuously repeating cardiac cycle, namely: ventricular diastole followed by ventricular systole, etc.—while coordinating with atrial systole followed by atrial diastole, etc. The cycle also correlates to key electrocardiogram tracings: the P wave (atrial systole), the QRS complex (ventricular systole), and the T wave (which indicates ventricular diastole);—all shown as color red.

from the left and right ventricles, respectively. As the blood ejects from the ventricles, the pressure decreases. When it decreases below the pressure in the aorta/pulmonary artery, the semilunar valves close and the heart enters into the isovolumetric relaxation phase again. Isovolumetric relaxation and ventricular filling comprise the “Diastole” period, whereas IVC and ventricular ejection comprise the “systole” period of the cardiac cycle.

The IVC time period is an important indicator of cardiac contractility, and is also known as the pre-ejection period (PEP) [29, 30]. Multiple studies have shown that PEP is inversely correlated with cardiac contractility [29, 30, 31]. The time for the left ventricular ejection is another important metric for left ventricular health, and the ratio of PEP and the left ventricular ejection time (LVET) (PEP/LVET) is also shown to be inversely correlated with cardiac contractility [32].

Other important cardiovascular parameters include stroke volume (SV), cardiac output (CO), and ejection fraction (EF). SV is the volume of blood that the heart pumps out in each heartbeat. It is measured as the difference between the end-diastolic volume (EDV) and the end-systolic volume (ESV). CO is the average volumetric flow rate of blood from the heart in liters per minute, and is calculated by multiplying SV with heart rate (HR). EF is the measurement of the fraction of blood the heart pumps in each heartbeat, and is calculated as the ratio of SV over EDV. The equations to calculate the parameters are given below as well.

$$SV = EDV - ESV \tag{2.1}$$

$$CO = SV \times HR \tag{2.2}$$

$$EF = \frac{SV}{EDV} \tag{2.3}$$

2.3 Heart Failure Pathophysiology

HF is a syndrome caused by structural or functional abnormalities of the heart, which result in impairmed myocardial contractility (systolic dysfunction) or impairmed ventricular filling (diastolic dysfunction) that lead to reduced CO and elevated intracardiac pressure [33, 7]. HF is often characterized by symptoms such as dyspnea, edema and fatigue [34] and signs such as elevated left ventricular filling pressure and peripheral edema [35, 36]. Fig. 2.4 shows a pictorial demonstration of the two cases of HF in contrast to a healthy heart.

2.3.1 Systolic Heart Failure

In the case of systolic HF, the heart muscle becomes weak and enlarged. It cannot pump enough oxygen-rich blood forward to the rest of the body when the ventricles contract. In systolic heart failure, the EF is lower than normal ($<45\%$). This can cause blood to back up

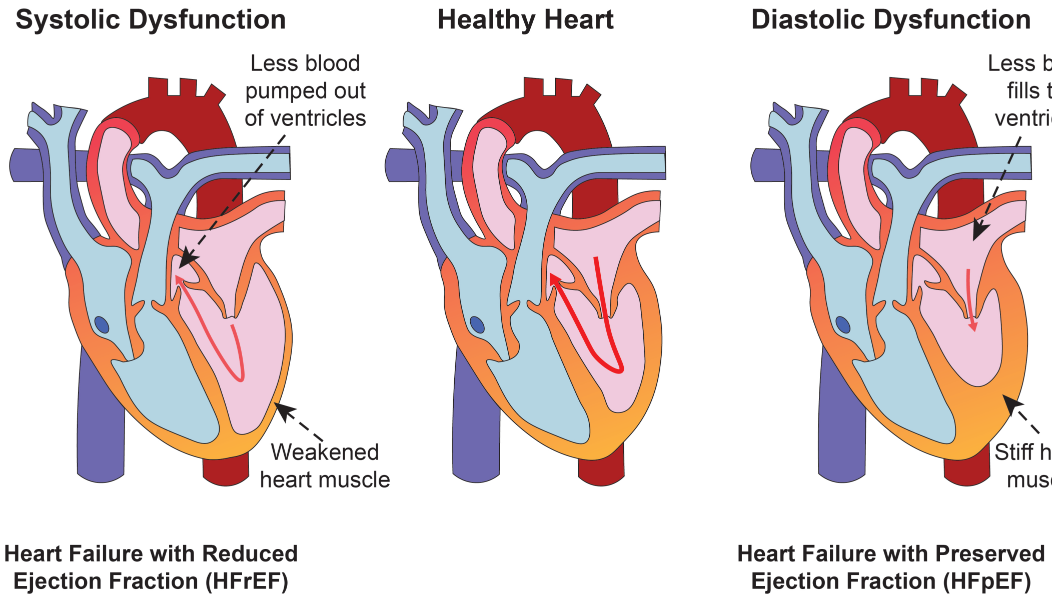

Figure 2.4: Comparison of systolic and diastolic heart failure with a normal healthy heart. Adapted from [37].

into the lungs and cause shortness of breath and eventually ankle swelling (edema). This phenotype of HF is commonly referred to as HF with reduced ejection fraction (HFrEF).

2.3.2 Diastolic Heart Failure

In the case of diastolic HF, the heart muscle becomes stiff (low compliance). It does not relax normally between contractions, which keeps the ventricles from filling with blood. EF is often in the normal range ($>45\%$), but preload is diminished thus leading to reduced CO. This can still lead to the backup of blood into the body and affect the organs such as the liver. This phenotype of HF is commonly referred to as HF with preserved ejection fraction (HFpEF).

CHAPTER 3

WEARABLE CARDIOVASCULAR HEALTH MONITORING

Advancement of sensing systems, digital technologies, and advanced data processing technologies have shown an increase in the wearable health care monitoring systems to monitor the health of an individual both for self-health tracking (fitness/activity monitoring) and for medical level monitoring for relevant patient populations (hemodynamic monitoring) by monitoring vital signs[38]. These vital signs include heart rate, respiration rate, body temperature, blood pressure, blood glucose, and oxygen saturation. Wearable sensors for measuring these parameters comprise various shapes and form factors, including smartwatches, wearable chest patches, chest belts, earworn sensors, finger clip sensors, wrist bands, and instrumented vests. [38]. To monitor these vital signs for both healthy individuals and patients with various diseases, myriad sensing modalities have been explored and researched, including electrocardiogram, impedance cardiogram, seismocardiogram, ballistocardiogram, photoplethysmogram, and galvanic skin response. [39, 38]. Out of these different sensing modalities, some can record the central cardiovascular parameters (electrical and mechanical activity of the heart), and some can record the peripheral parameters related mainly to the vasculature or sympathetic activity (vasoconstriction, vasodilation, and skin conductance). Table. 3.1 and Fig. 3.1 (a) illustrate representative signals that can measure central hemodynamic parameters of the cardiovascular system noninvasively. The following sections will explain these sensing modalities briefly and discuss their usability in remote HF management.

3.1 Electrocardiogram

The electrocardiogram (ECG) signal captures the propagation of action potentials in the heart. The ECG can be measured as the potential difference between various points on

Table 3.1: Noninvasive Biosignals for Monitoring Central Hemodynamic / Electrophysiologic Parameters Indicative of Cardiovascular Health.

Signals	**Aspect**	**Unit**	**Obtrusive/Portable**
Electrocardiogram	Measures electrical activity of the heart by recording electrical potentials	mV	No/Yes
Impedance Cardiogram	Measures thoracic impedance which is modulated by the pulsatile blood flow	ohm/ ohms^{-1}	Yes/Yes
Seismocardiogram	Measures local chest vibration associated with the movement of the heart and pumping of blood through the vasculature	mg	No/Yes
Ballistocardiogram	Measures the forces acting on the body associated with movement of blood through the vascular tree	N	No/ Maybe

the body with skin-mounted electrodes. By different configurations of these electrodes, the ECG projection at different directions can be measured [40]. The ECG shown in Fig. 3.1(a) is recorded in a Lead II configuration as demonstrated in Fig. 3.1(b).

The characteristic feature points depict the depolarization (starting of contraction of the heart muscles) and repolarization (starting of relaxation of the heart muscles) of the heart muscle, as also explained in Fig. . The P wave represents the start of depolarization of the atria (atrial systole/kick), the QRS complex represents the depolarization of the ventricles (ventricular systole) with q-wave as the start of the ventricular systolic phase, and the T wave represents the repolarization of the ventricles.

The ECG has been used to monitor the rhythm of the heart and for detecting abnormal rhythm or abnormalities in the heartbeats (or shape of the signals or peaks), which are known as arrhythmias, and ST-segment elevation for myocardial infarction (heart attack). In the hospitals, the clinicians generally use a 12-lead ECG system as an early diagnostic tool [40]. ECG can be measured using a Holter-type ambulatory monitor or patch, a modality that is very common for arrhythmia detection in outpatient monitoring [41, 42].

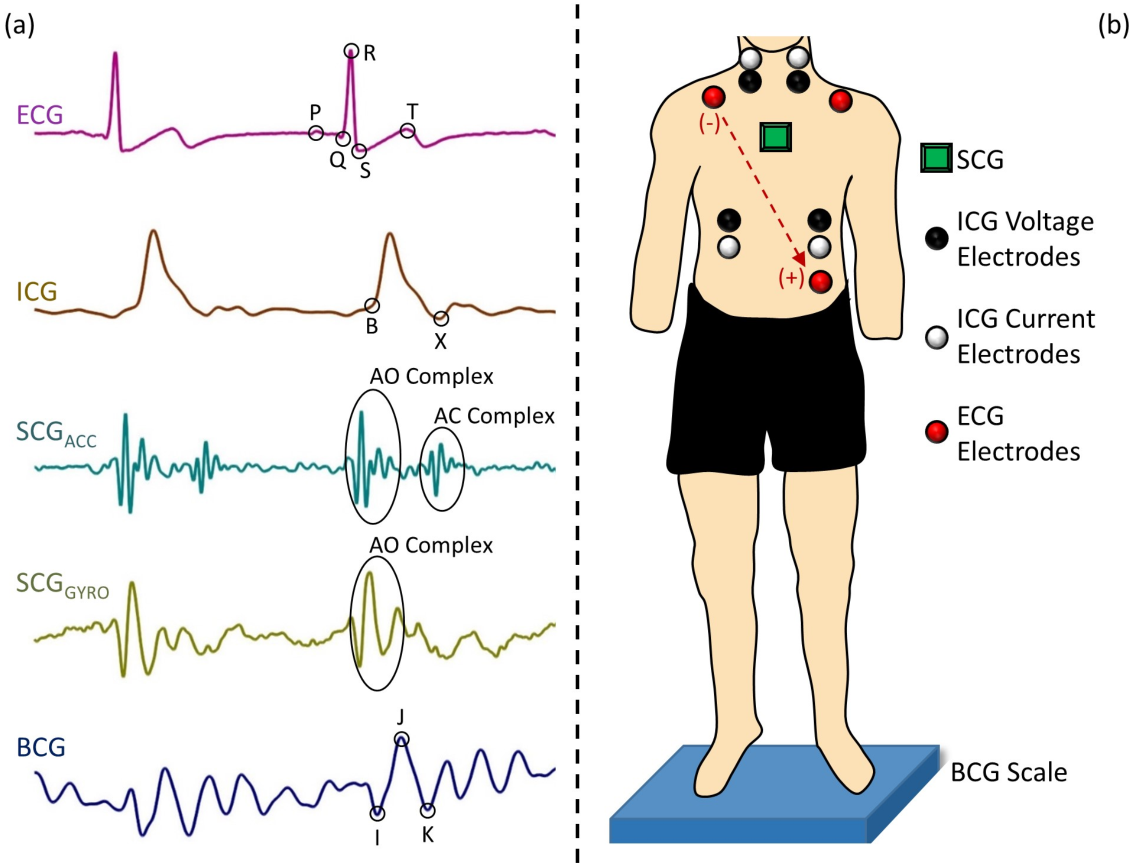

Figure 3.1: (a) Representative wearable signals with characteristic feature points. (b) Typical sensor placements for ECG, ICG, SCG and BCG with the red arrow and +/- sign showing the lead II configuration for the ECG.

3.2 Impedance Cardiogram

The impedance cardiogram (ICG) signal captures the electrical conductivity (impedance) of the thorax that changes with the pulsatile flow of the blood ejected from the heart with each heartbeat [43]. The ICG sensing system consists of four pairs of electrodes, as shown in Fig. 3.1(b), two pairs on the neck, and two pairs near the diaphragm, The outer pair of electrodes are current electrodes, and the inner pair of electrodes are voltage electrodes. An electrical current is passed between the current electrodes, and the potential difference between the voltage electrodes is measured, and the thoracic impedance is estimated using Ohm's law [44].

The ICG is used to measure several hemodynamic parameters and cardiac timing intervals, such as SV, cardiac output CO, PEP, and LVET [44]. As shown in Fig. 3.1(a), the B and X points represent the aortic valve opening (AO) and aortic valve closing (AC) respectively [45]. The B-point is defined as the inflection point of the waveform, or point of maximum second-derivative; the X-point is defined as the minimum point of the signal following the global maximum. The ICG has been often used as a reference standard for AO and AC estimation due to its convenience compared to echocardiography, an imaging modality to view the heart in a noninvasive way. However, recent studies have shown that ICG derived PEP (time difference between the Q or R peak of the ECG and the B-point of the simultaneously recorded ICG) overestimates the PEP extracted from echocardiography [46, 45, 47].

3.3 Seismocardiogram

The seismocardiogram (SCG) signal is the local vibration of the chest wall due to heartbeat, and it was first discovered and characterized by Bozhenko [48], and first applied clinically by Salerno and Zanetti, using an accelerometer placed on the mid sternum [49]. In 1994, Crow used concurrently recorded echocardiogram images to identify fiducial points in the SCG waveform corresponding to CTIs [50]. As research in this field grew, researchers delved more deeply into the correlation between specific SCG features and events seen on echocardiography [51, 52]. Such studies showing the correlation between SCG features and known CTIs provide the most concrete basis for the use of SCG to monitor cardiac function. For the last decade, the SCG signal has been studied extensively where amplitudes and timing intervals of different peaks of the SCG signal have been used to derive cardiovascular parameters in daily life activities [53] and to detect various diseases [54, 55, 56].

The majority of the research on SCG signals [39, 57, 58] focuses on the linear acceleration of the chest wall in the dorso-ventral axis, with the underlying assumption that chest vibrations due to the heartbeat are mainly comprised of linear motion. However, a recent study by Migeotte, et al. has shown that the rotational component represents more than 60% of the total kinetic energy transferred from the heart to the body in both healthy subject, and persons with CVDs [59]. This study suggests that the rotational component of chest wall vibrations may provide more information regarding the mechanical aspects of the heart, in addition to the linear component. Recently Tadi, et al. used a gyroscope on the mid sternum to record the mechanical activity of the heart [60]. They found that time intervals between the ECG R-wave and some peaks within the gyroscope signal correlated well with AO and AC, measured using echocardiography. Fig. 3.1(a) shows two typical SCG signals from the accelerometer ($\mathrm{SCG}_{\mathrm{ACC}}$) and gyroscope ($\mathrm{SCG}_{\mathrm{GYRO}}$) sensor, where the AO and AC complexes are marked. Researchers typically use the specific peaks in these AO and AC complexes to obtain CTIs from SCG with the help of concurrently recorded ECG R-peak as a reference [39, 58, 51].

Recent studies have demonstrated the utility of SCG in monitoring cardiovascular health for persons with CVDs [39, 23, 58, 61, 55, 62]. As SCG can be recorded using an unobtrusive portable sensor placed on the chest wall [39, 58], it has shown promise in monitoring cardiovascular health during exercise and daily life activities and has the potential in remote home management for patients with HF.

3.4 Ballistocardiogram

The ballistocardiogram (BCG) signal is a measurement of the recoil forces of the body in reaction to the cardiac ejection of blood into the vasculature [63], which was first observed by Gordon in 1877 [64]. The BCG is generally recorded in the longitudinal (head-to-foot) direction [39] using a modified weighing scale [65], bed or table-based systems [63] and modified toilet seats [66]. The bottom picture of Fig. 3.1(a) shows the longitudinal BCG recorded using a modified weighing scale [65].

Researchers have been used the characteristic features points in the BCG signal to track hemodynamics in healthy subjects [67, 68] and patients with CVDs [69]. Researchers have shown the changes in intervals between simultaneously recorded ECG R-peak and BCG I and J peak (R-I and R-J intervals) are correlated with cardiac contractility (PEP) [67, 70]. Aydemir, et al. has shown that the features of a modified weighing scale based BCG signal can be used to assess the clinical state of patients with HF [71]. Another recent study has shown the application of bed-based BCG in detecting sleep stages [72].

Though BCG has proven its merits in monitoring cardiovascular health both in healthy subjects and patients with CVDs, it can be corrupted by motion artifacts, its morphology can be affected by gravity, and any contact of the body with external objects can affect the repeatability of the measurement [39]; it has been proved that the ideal environment for assessing the BCG would be in microgravity [73, 74, 75]. These limitations may preclude the usage of BCG in cardiovascular health monitoring when a person is moving or exercising.

CHAPTER 4

PERFORMANCE ANALYSIS OF GYROSCOPE AND ACCELEROMETER SENSORS FOR WEARABLE SEISMOCARDIOGRAPHY

4.1 Overview

Systolic time intervals such as the pre-ejection period (PEP) are important parameters for assessing cardiac contractility that can be measured non-invasively using seismocardiography (SCG). Recent studies have shown that specific points on accelerometer and gyroscope based SCG signals can be used for PEP estimation. However, the complex morphology and inter-subject variation of the SCG signal can make this assumption very challenging and increase the root mean squared error (RMSE) when these techniques are used to develop a global model. In this study, we compared gyroscope and accelerometer based SCG signals, individually and in combination, for estimating PEP to show the efficacy of these sensors in capturing valuable information regarding cardiovascular health. We extracted general time domain features from all the axes of these sensors and developed global models using various regression techniques. In single axis comparison of gyroscope and accelerometer, angular velocity signal around head to foot axis from the gyroscope provided the lowest RMSE of 12.63±0.49 ms across all subjects. The best estimate of PEP, with a RMSE of 11.46±0.32 ms across all subjects, was achieved by combining features from the gyroscope and accelerometer. Our global model showed 30% lower RMSE when compared to algorithms used in recent literature. Gyroscopes can provide better PEP estimation compared to accelerometers located on the mid sternum. Global PEP estimation models can be improved by combining general time domain features from both sensors. This work can be used to develop low cost wearable heart monitoring device and to generate a universal estimation model for systolic time intervals using single or multiple sensor fusion.

4.2 Introduction

The pre-ejection period (PEP) of the heart is defined as the time elapsed from the start of ventricular depolarization to the ensuing opening of the aortic valve, and is an important parameter for assessing cardiac health outside of clinical settings [30, 29, 31]. In particular, the changes in PEP resulting from exercise stressors can provide insight into the ability of the heart to respond appropriately to increased sympathetic nervous system activity and increased demand for blood flow to the muscles. An important recent finding was that the clinical status of patients with heart failure (HF) – a disorder in which the heart is unable to supply enough blood to meet the demands of the body – could be assessed using SCG (and PEP) responses to exercise measured with a wearable sensing system [76, 69, 23]. The wearable system used for that study facilitates computation of PEP from electrocardiogram (ECG) and seismocardiogram (SCG) signals [77]. The Q- or R-wave of the ECG signal provides the timing information required for detecting the depolarization of the ventricles (the start of the PEP interval); the Ao "peak" on the SCG signal provides the corresponding timing for the aortic valve opening (AVO) (the end of the PEP interval) [46]. In this system, the ECG is measured using three adhesive-backed gel (Ag/AgCl) electrodes, and the SCG is measured using a low-noise, tri-axial micro-electromechanical systems (MEMS) based accelerometer positioned at the middle of the sternum. Though promising results have been obtained with this system both in healthy subjects and in patients with HF, there are sensing and data analytics advancements that can potentially improve the accuracy with which PEP is measured. First, recent work has shown that gyroscope based measurements of chest wall vibrations may provide improved detection of heart and blood movement activity as compared to accelerometers [78, 79, 60]. A rigorous investigation is needed comparing gyroscope and accelerometer based SCG waveforms and the corresponding accuracy with which PEP can be extracted. Second, while the opening of aortic valve may be readily detectable from SCG signals in supine subjects, high inter-subject variability in SCG waveforms renders Ao peak detection inaccurate and ambiguous in many subjects standing upright or walking. Novel machine learning approaches for combining multiple features of gyroscope, accelerometer, and combined gyroscope and accelerometer based SCG measurements can be employed to address this limitation. In this work we perform, for the first time, a rigorous investigation of gyroscope and accelerometer based SCG measurement in the context of PEP detection accuracy. We use a low-noise MEMS gyroscope with sufficiently wide bandwidth to facilitate SCG measurement. We further leverage state-of-the-art nonlinear and linear regression algorithms [80, 81] to map features of the SCG signal to AVO, as detected by a reference standard signal—the impedance cardiogram (ICG) [82, 43]. In addition to single axis based estimates, we evaluate multi-axis and multi-sensor fusion approaches to assess the possible corresponding improvement in PEP estimation. Finally, we compare our PEP estimation approaches directly against several methods from the existing literature. Fig. 4.1 shows a hypothetical system to estimate systolic timing intervals from wearable sensors' fusion using our estimation method.

4.3 Method

4.3.1 Experimental Protocol

The study was conducted under a protocol approved by the Georgia Institute of Technology Institutional Review Board. A total of 17 healthy subjects (7 females and 10 males) participated in the study (Age: 26.1±4.1 years, Weight: 66.2±13.6 kg and Height: 168.2±8.9 cm). All subjects provided written informed consent before experimentation and reported no heart problems. The purpose of the protocol was to induce changes in PEP non-invasively, and to then measure PEP with a reference standard (ICG) simultaneously with different sensors under test. Regression algorithms were then applied to compare the PEP estimation accuracy for these sensors under test compared to the reference standard. Exercise was selected as the means by which PEP was modulated non-invasively because it is known to change PEP substantially from the resting value in a relatively short period

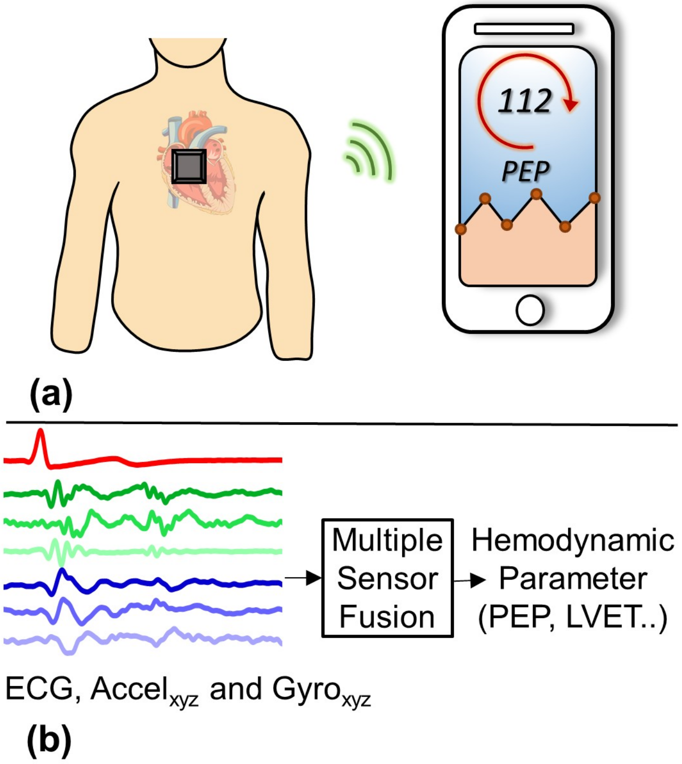

Figure 4.1: (a) Concept of a wearable device to monitor cardiovascular health parameters and (b) proposed sensors and corresponding signals.

of time.

Fig. 5.3 (a) illustrates the placement of sensors on each subject. For each subject, the middle point between the suprasternal notch and xiphoid process was located on the mid-sternal line. The accelerometer was placed on top of the point and the gyroscope was placed below the point. Both the sensors were attached using tape (Kinesio Tex, Kinesio, Albuquerque, NM). After placing the wearable sensors, each subject was asked to step on the modified weighing scale, which is capable of measuring ballistocardiogram (BCG) signal. The subject was asked to stand vertically and motionless for five minutes. Then, the subject performed three minutes of walking exercise at 3 miles per hour (mph) on a treadmill followed by one and a half minutes of squatting exercise. After the full exercise period, the subject stepped on the BCG scale again for monitoring the recovery period for five minutes. The whole procedure was performed continuously, as shown in Fig. 5.3 (f).

PEP decreased due to exercise and returned to baseline value of resting PEP during the recovery.

4.3.2 Sensing Hardware

Linear and angular vibrations of the chest wall due to the heart beat were recorded using a three-axis analog output accelerometer (ADXL354, Analog Devices, Inc., Norwood, MA) and a three-axis differential analog output gyroscope (QGYR330HA, Qualtre Inc., Marlborough, MA) [83] respectively. Both the MEMS accelerometer and gyroscope have very low noise and low drift. Fig. 5.3 (c) shows the linear and angular directions for the accelerometer and gyroscope, respectively. The gyroscope's differential outputs were passed through an instrumentation amplifier (AD8226, Analog Devices, Inc., Norwood, MA) to have one output signal per axis, shown in Fig. 5.3(b). BCG was measured simultaneously using a previously validated modified weighing scale [65]. Seven outputs (three from the accelerometer, three from the gyroscope and one from the scale) were connected to the data acquisition system (MP150, BIOPAC System, Inc. Goleta, CA). ECG and ICG signals were measured concurrently using BN-EL50 and BN-NICO wireless modules (BIOPAC System, Inc., Goleta, Ca). Both signals were transmitted wirelessly to the MP150. The sampling frequency for all the signals was 2 kHz.

4.3.3 Signal Processing and Feature Extraction

Linear Filtering and Pre-Processing: All the raw signals (accelerometer and gyroscope based SCGs, ICG, BCG, and ECG) were filtered with finite impulse response (FIR) Kaiser window band-pass filters (cut-off frequencies: 1-40 Hz for both the accelerometer and gyroscope signals, 0.5-20 Hz for the BCG, 1-30 Hz for the ICG and 0.5-40 Hz for the ECG). These cut-off frequencies were chosen based on the existing literature [77, 65, 84], to remove out-of-band noise without distorting the shape of the signals. The same cutoff frequencies were used for both gyroscope and accelerometer based chest vibration signals.

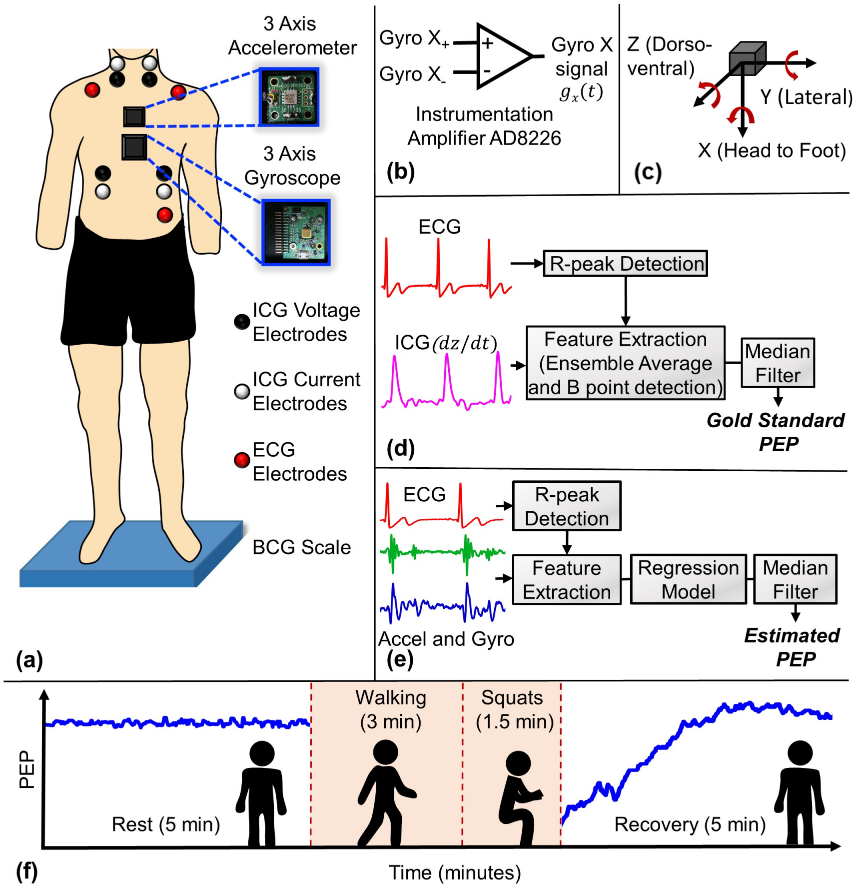

Figure 4.2: (a) The experimental setup with the subject standing on the BCG scale, with all other wearable sensors attached to the body. One accelerometer (ADXL354) and one gyroscope (QGYR330HA) are placed on the mid sternum. ECG and ICG signals are collected simultaneously. (b) Circuit connection for the conversion of differential output of the gyroscope to single output per axis, using an instrumentational amplifier (AD8226). (c) Axis labels used for the accelerometer and gyroscope, with accelerometer X axis in the head to foot direction, Y axis in the side to side (lateral) direction and Z axis in the dorso-ventral direction. Gyroscope X axis angular velocity corresponds to the rotation around head to foot axis, Y axis angular velocity corresponds to the rotation around frontal axis and Z axis angular velocity corresponds to the rotation around sagittal axis. (d) Block diagram of the segmentation for ICG signal with reference R peaks from the corresponding ECG signal, feature extraction from the ICG segments to calculate ground truth PEP. (e) Block diagram of the segmentation for accelerometer and gyroscope signals with reference R peaks from corresponding ECG signal, feature extraction from the segments to estimate PEP. (f) PEP trend with the chronology of the experiment, 5-minute rest standing on BCG scale, 3-minute walk at 3 miles per hour speed, 1.5-minute of squats and 5-minute post exercise standing on the scale. PEP remains fairly stable during the rest period, it decreases due to exercise, and returns nearly to the baseline rest values during the recovery period.

The signal-to-noise ratio (SNR) of the ECG was found to be very poor for one of the subjects due to hardware issues, therefore data from this subject was discarded and data from the other 16 subjects were used for further processing and analysis.

As most physiological measurements are corrupted by motion artifact during exercise, which typically leads to higher noise, the signals recorded during exercise were discarded. Since the goal of this analysis was to determine which features of SCG (accelerometer and gyroscope) signals were most salient in PEP estimation, we decided rather to use only the cleaner portions of the datasets – those corresponding to the initial 5-minute resting and 5-minute post-exercise recovery data. The signal processing and feature extraction were performed in Matlab 2017b with a Macbook Pro Laptop with Core i5 dual core processor and 16 GB of RAM and required approximately 54 minutes of processing time.

Ensemble Averaging: The R-wave peaks were detected on the ECG signal and all the other signals (SCG, BCG, and ICG) were segmented into individual heartbeat frames using the R peaks from the corresponding ECG signals, with a frame length equal to the minimum R-to-R interval. With frame length equal to the minimum R-to-R interval, one frame contained at a maximum one heartbeat by definition. In other cases, one frame contained less than one heartbeat. Multiple frames were ensemble averaged to get averaged frames, which reduced noise [85]. Five frames were averaged together to generate an ensemble averaged frame, with an overlap of four frames between consecutive ensemble averages. This technique of averaging was used to maximize the number of ensemble averaged frames, with a total of 13,993 heartbeat frames from 16 subjects.

Feature Extraction from ICG and BCG: The B-point and X-point of the ICG (dz/dt) frames, were extracted based on [67]. The B-point was then used as the reference standard AVO, and the ground truth PEP was obtained via calculating the R-B interval for every ensemble average frames. A high level block diagram of this process is shown in Fig. 5.3 (d). The X-point of the ICG corresponds to the aortic valve closing (AVC). For BCG frames, I, J and K peaks were extracted following the work of Inan et al. [65].

Feature Extraction from SCG: For the accelerometer and gyroscope signals, initially we extracted and analyzed different time domain, amplitude and frequency domain features. Time domain features performed better in PEP estimation compared to amplitude and frequency domain features as PEP itself is a time domain parameter. A total of 12 time domain features were chosen for detailed analysis in this work. These 12 features per axis were extracted from each averaged frame by an automated algorithm and every frame was visually checked to maintain the accuracy of the feature extraction. Features extracted were as follows: largest and second largest maxima locations (0-250 ms), largest and second largest maxima width (0-250 ms), largest and second largest minima location (0-250 ms), largest and second largest minima width (0-250 ms), largest maxima location (250-500 ms), largest maxima width (250-500 ms), largest minima location (250-500 ms), largest minima width (250-500 ms). Peaks and valleys in the frame were ranked according to their amplitudes, and the highest and second highest amplitude were used as the largest and second largest maxima or minima accordingly. Location was calculated as the distance from the corresponding R-peak in ms. Width was calculated as the width of the peak or valley at half-prominence, in ms. We extracted eight timing features from the systolic portion of the signal (0-250 ms) rather than putting emphasis on one location feature, to explore how multiple points in the accelerometer and gyroscope signals are related to the AVO. Although PEP is related to the timing features from the systolic portion of the signals, we decided to explore features from the diastolic portion (250-500 ms) of the signals as well and we have extracted four timing features from the diastolic portion of the signals.

4.3.4 Regression Models

Overall Framework: We trained a regression model to estimate the PEP using the features extracted from the accelerometer and gyroscope signals described in Section II.C. For every axis, M features were extracted from N ensemble averages. These features were placed in an matrix $\mathbf{A}$ while the corresponding PEP values were placed in an vector $\mathbf{b}_{\text{PEP}}$. A regression model was trained on these to learn the relationship between $\mathbf{A}$ and $\mathbf{b}_{\mathrm{PEP}}$. Resulted trained model can then be used to estimate PEP for new heartbeat frames, from the features extracted from the accelerometer or gyroscope signals. Fig. 5.3 (e) shows the high level block diagram of the feature extraction and regression on the accelerometer and gyroscope signals to estimate the PEP. The machine learning techniques, including various regression models, were performed using Python 3.6 with the same laptop described in the later section. It required approximately 20 to 60 minutes of processing time for different regression techniques based on the parameters and features used.

XGBoost Regression: The majority of the research on SCG to estimate hemodynamic parameters used conventional linear regression to relate the features from SCG to the estimated parameter [60, 84, 86, 87, 88], with the underlying assumption that the relationships are linear. However, the relationship between PEP and SCG features may not be linear as is the case in most real data sets. That is, if we let Y represent PEP as a random variable and X represent one of our features, it is unlikely that $f(X)=E(Y|X)$ would be a linear function in X [89]. Our aim was to evaluate whether a non-linear model performs better in estimating PEP compared to the standard linear models. Therefore, rather than using only linear techniques, we leveraged Extreme Gradient Boosting (XGBoost) regression, which is a relatively new machine learning algorithm that has recently gained popularity [81]. XGBoost is a computationally efficient implementation of the gradient boosting machine learning algorithm [90], and is an example of an ensemble method, combining multiple estimators to predict a variable rather than using a single estimator [91]. It generates multiple regression trees where errors from previous models are predicted by new models and are then added together. It uses a gradient descent algorithm for this addition to minimize the loss and these sequential additions are carried out until no further improvements can be made.

We used XGBoost regression (with hyper-parameter settings: learning rate=0.1, number of boosting rounds=200, column sampling factor=0.5, row sampling factor=0.5, regularization parameter (λ)=1) to estimate PEP using features extracted from different axes of the accelerometer and gyroscope based SCG signals and combination of multiple axes from the same sensor or both the sensors. Estimated PEPs from different axes and from different combinations of axes and sensors were compared using a variation of the repeated cross-validation model assessment method discussed in [92].

Cross-Validation and Regression Model Evaluation: We first randomly paired the subjects in our dataset, which consists of 16 subjects, into eight groups. We then performed cross-validation by leaving one group (two subjects) out at each fold and trained an XG-Boost regressor on the data from all subjects except the two that were left out. We then predicted PEP for the left-out subjects and repeated this seven more times leaving a different pair of subjects out each time. As a result, we have PEP predictions for all ensembles from all subjects. The root mean squared error (RMSE) was then calculated between the estimated PEP values ($\mathrm{PEP_e}$) and the ground truth PEP acquired from the ICG signals ($\mathrm{PEP_a}$):

$$RMSE = \sqrt{\frac{1}{N}\sum_{i=1}^{N}(RMSE_{\mathrm{e,i}} - RMSE_{\mathrm{a,i}})^2} \tag{4.1}$$

where N=13,993, the number of ensemble average frames from 16 subjects. We used leave-two-out cross validation over leave-one-out cross validation to have more variation in the training sets, and did not have enough subjects to leave more subjects out in the cross-validation steps. We repeated the entire process 50 times with a new random pairing of subjects each time. The cross-validation RMSE was calculated as the average of the RMSE scores from 50 repetitions. In this way, we trained a global model rather than multiple subject-specific models.

Regression for Multiple Axes: This approach was repeated for different axes of the accelerometer and gyroscope and their combination, and we compared the resulting RMSE scores. For the combination of multiple axes from the same or different sensors, features from a pair of axes or multiple axes were combined using vector concatenation and were fed into regressors. The same cross-validation procedure was used to compute the RMSE. We performed statistical analysis of the cross-validation results for single and multiple axes comparisons.

Regression for BCG Signals: Three features (R-J interval, R-I interval and R-K interval) from the ensemble averaged BCG frames were also used in similar fashion to develop another global model following the same cross-validation step stated above, to estimate PEP. Average RMSE from this model gave us the comparison between wearable sensors to the scale based cardiac hemodynamics monitoring.

4.3.5 Feature Importance Evaluation

To generate global models of PEP estimation from the accelerometer and gyroscope signals, we trained XGBoost regressors using many features acquired from one or multiple axes from one or both of the sensors. However, some of these features are more relevant to PEP estimation than others. One advantage of using XGBoost (and other gradient boosting methods) is that, it can provide feature importance estimates from a trained predictive model. This importance indicates how useful each feature is in constructing the boosted decision trees within the model [93]. Typically, the main node of a tree is divided based on the most important feature whereas the deep nodes are divided based on less important features. The feature importance values obtained from all of the decision trees within the model are averaged to get the final relative feature importance scores. These scores can be used to rank the features.

To evaluate which features generated from the accelerometer and gyroscope based SCG signals contributed more to PEP estimation, we trained an XGBoost regressor on the combination data set from all 16 subjects, with features from all the axes of the gyroscope and accelerometer. The resulting regression model was then used to generate relative feature importance scores as described above.

4.3.6 Comparing Our Estimation with Existing Literature

We compared our PEP estimation method with recent PEP estimation methods used in literature, where the researchers annotated specific points in the accelerometer and gyroscope signals using ECG as a reference signal and found those points to be well correlated with the AVO [78, 60, 94, 95]. Tadi et al. [94] and Javaid et al. [95] used a fixed length window of 90 and 200 ms respectively from ECG R peaks to find the AVO points in the dorso-ventral SCG. Yang et al. showed that the maximum peak of the envelope of rotational energy, calculated from the gyroscope signal, is close to the isovolumic moment (IM) of the accelerometer signal, where IM is the minima immediately before AVO in the accelerometer based dorso-ventral SCG signal [78]. Tadi et al. annotated the major maximum peak in angular velocity around the head-to-foot axis (from the gyroscope signal) as AVO and found strong correlation between the time interval between this point and corresponding ECG R-peak with PEP from echocardiography [60]. We have used the aforementioned algorithms to find AVO from the ensemble average heartbeat frames of corresponding accelerometer and gyroscope signals, in our dataset. We have used the same cross-validation method, described in Section II.E and calculated RMSE for each method to compare to our methods.

4.3.7 Statistical Analysis

We performed statistical analysis on the cross-validated RMSE results to compare different axes and combination of axes. In our cross-validation procedure which consisted of 50 repetitions, the random seed was fixed so that the subjects were paired in the same way in the ith repetition, for all sensor axes/combinations. Multiple comparison tests were performed on the RMSE results from the 50 repetitions to compare different axes and sensor combinations. The Friedman test was performed to detect statistical differences if exist and the Wilcoxon signed rank test was performed for post-hoc testing, on different axes or combinations. Additionally, for the post-hoc testing Benjamini-Hochberg correction for multiple comparison was performed on the p-value. Details on these statistical tests and the reasons behind their use are discussed in [96]. We performed similar procedure to compare different regression techniques and to compare our method with different algorithms from recent literature statistically. In this work, p-values below 0.05 were considered statistically significant.

4.4 Results and Discussion

4.4.1 Intersubject Variability

A visual comparison of the complex nature and intersubject variation in signals from both the accelerometer and gyroscope is shown in Fig. 4.3. AVO and AVC points, extracted from corresponding ICG signals, are marked on these signals, demonstrating that the AVO and AVC may not always correspond to specific points or patterns on the accelerometer or gyroscope signal, as often stated in existing literature. Estimation of systolic timing intervals based on this assumption might be error-prone and may work on a specific data set or subject, but not for a global model.

4.4.2 t-SNE Visualization

The features extracted from the ensemble averaged frames were analyzed using machine learning techniques. To visually compare the features generated using different axes and combinations of axes of the accelerometer and gyroscope signals, t-SNE (t-Distributed Stochastic Neighbor Embedding) [97] was used. The dimensionality of our data set, which has twelve features (dimensions) per sensor axis, was reduced to two dimensions using t-SNE. A scatter plot of the data was constructed where the two axes are the two t-SNE dimensions and each point represents one ensemble averaged frame (Fig. 4.4). Each point was colored according to the ground truth PEP of the frame to visualize the relationship between the t-SNE dimensions and our target variable (PEP). If a particular feature has information relevant to PEP, we would expect to see a pattern in the color distribution,

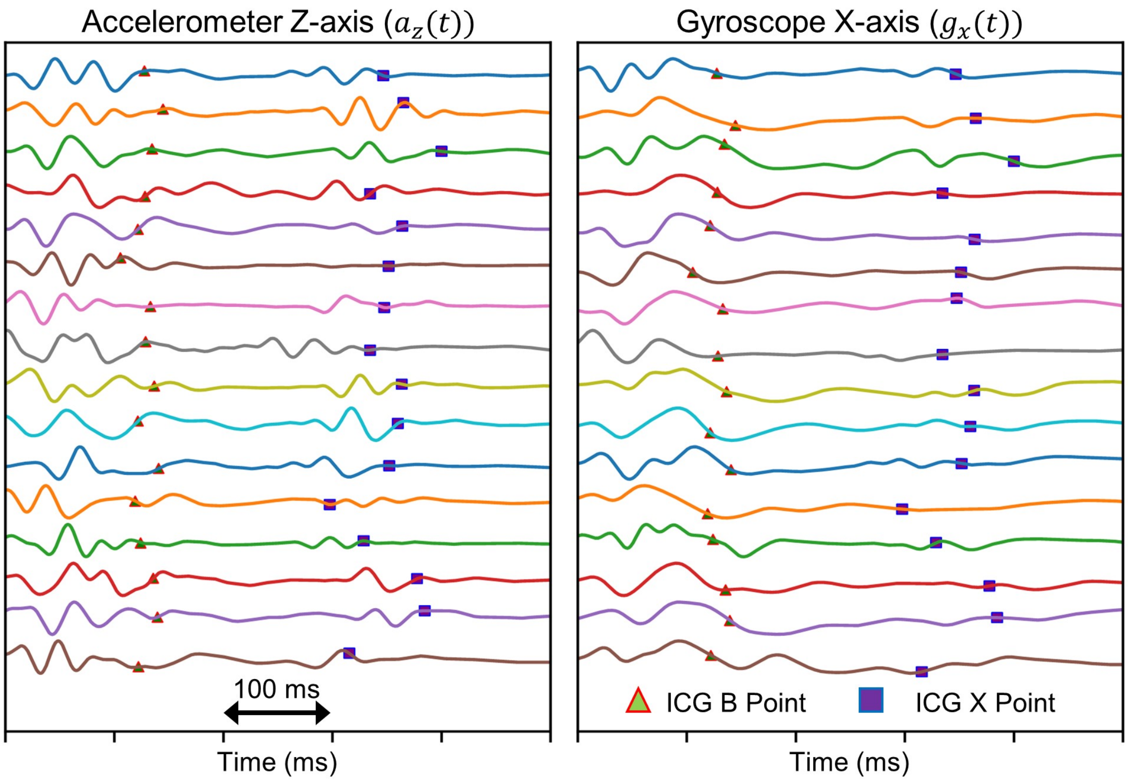

Figure 4.3: Illustration of inter-subject variability in accelerometer and gyroscope signals from rest data of 16 subjects, with AVO (B-point) and AVC (X-point) annotated from corresponding ICG signals. (Left) Ensemble average of 100 heartbeats of the accelerometer Z-axis (dorso-ventral) signal and (right) ensemble average of 100 heartbeats of the gyroscope X-axis (angular velocity around head-to-foot axis) signal. All the signals are normalized in amplitude.

whereas if no relevant information is present, we would expect the colors to be randomly distributed spatially in the plot. Examples where t-SNE is used to visualize the relationship between a high dimensional feature space and a continuous variable can be found in [98, 99].

The t-SNE method considers $p_{j|i}$the probability that a data point x_i would pick x_j as its neighbor, in high dimensions, as a similarity metric between data points. The similarity metric between lower dimension counter parts of these points are denoted as $q_{j|i}$ which is defined similarly to $p_{j|i}$. The t-SNE algorithm finds a low dimensional embedding of the data such that $p_{j|i}$ and $q_{j|i}$ remain similar [97]. We prefer t-SNE to other dimensionality reduction techniques such as principal component analysis (PCA) or isometric feature

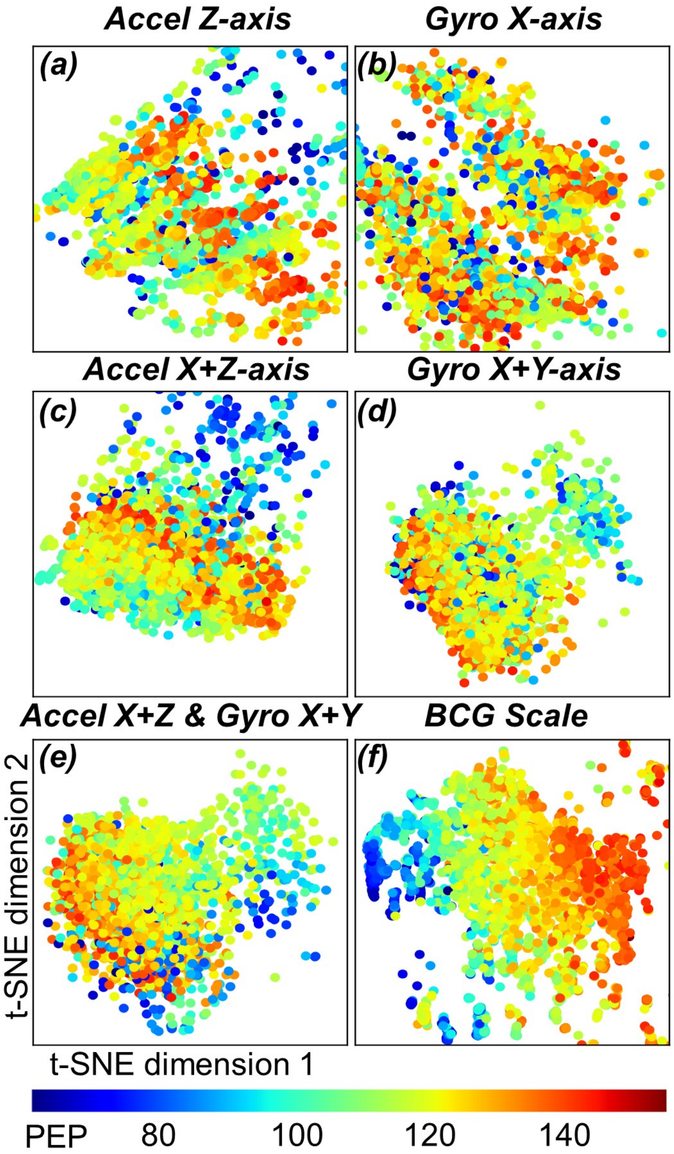

Figure 4.4: Visual comparison of features from single axis and combination of axes from the accelerometer and gyroscope signal, and features from BCG with target variable PEP from ICG using t-Distributed Stochastic Neighbor Embedding (t-SNE): (a) plot for features from z axis of the accelerometer, (b) plot for features from x axis of the gyroscope, (c) plot for combination of features from x and z axes of the accelerometer, (d) plot for combination of features from x and y axes of the gyroscope, (e) plot for combination of features from x and z axes of the accelerometer and x and y axes of the gyroscope. (f) plot for features from scale based BCG.

mapping (ISOMAP) because it was shown in the literature [99] that t SNE preserves the details within the data structure better and minimizes local distortions. One limitation of t-SNE is that it has computational complexity that is quadratic in the number of data points.

To reduce computational time, our data points were down-sampled by a factor of three from 13,993 points to 4,664 points, which is sufficient for the purpose of t-SNE visualization.

Fig. 4.4 is showing the visual comparison among features from a single or combination of axes from the gyroscope and accelerometer with our target variable PEP. Features from scale-based BCG are also shown in the figure to compare the wearable sensor with the scale-based BCG. In case of the accelerometer and gyroscope, each data point corresponds to all the features (12, 24 or 48 based on number of axes used) collected from the ensemble averaged frames. In case of BCG each point corresponds to three features, extracted from the ensemble average frames of BCG. These multiple dimensions (features) of data were reduced to two using t-SNE. Clear transition in the color pattern in the plots for the combination of axes over random nature in the color pattern for the single axis (both in the gyroscope and accelerometer) suggests that it is better to combine and use features from multiple axes in estimating PEP than using one axis only. While BCG is showing the best gradient in the color pattern, a combination of features from x and z axes of the accelerometer and x and y axes of the gyroscope is showing a color pattern which is the closest (compared to other four plots for single axis or pair of axes) to BCG.

4.4.3 Comparison and Combination of Accelerometer and Gyroscope

Table 4.1 shows the RMSE values in milli-seconds (ms) from different axes and their combination from the gyroscope and accelerometer signals. Statistically significant differences were found in these results according to Friedman test ($p<0.05$). Wilcoxon signed rank test was performed on the different axes and their combinations to investigate where the significance exists in post-hoc testing. When comparing single axes from the gyroscope and accelerometer, the results showed that the x-axis of the gyroscope signals provided the lowest RMSE of 12.63 ± 0.49 ms in PEP estimation (Fig. 4.5 (a)) ($p<0.05$). RMSE from y-axis of the gyroscope and z-axis of the accelerometer were similar ($p>0.05$). The z-axis of the gyroscope yielded a slightly higher RMSE than the x-axis of the accelerometer, whereas the y-axis of the accelerometer provided the highest RMSE in PEP ($p<0.05$).

Table 4.1: RMSE (ms) for PEP estimates from single axis and combination of multiple axes from Accelerometer (A), Gyroscope (G) signals and BCG

Axis	**RMSE**
G_x	12.63±0.49
G_y	13.54±0.31
G_z	15.50±0.29
G_x+G_y	12.13±0.40
G_x+G_y+G_z	12.26±0.33
A_x	15.16±0.40
A_y	19.03±0.55
A_z	13.54±0.31
A_x+G_z	12.98±0.30
A_x+G_y+G_z	13.66±0.39
G_x+A_z	12.63±0.42
G_x+A_x+A_z	11.76±0.32
G_x+G_y+A_z	11.84±0.41
G_x+G_y+A_x+A_z	11.46±0.32
G_x+G_y+G_z+A_x+A_y+A_z	11.79±0.44
BCG	9.39±0.20

For the linear acceleration components of the SCG signal, the most salient information being derived from the z-axis from the accelerometer is consistent with the existing literature [39], as the z-axis represents the dorso-ventral component of the signal – the component that has been most commonly analyzed and demonstrated as being useful in prior studies [77, 86, 53, 100]. For the rotational velocity components, the most salient information being derived from the x-axis of gyroscope is consistent with the direction of blood and heart movement inside the chest [101]. Prior imaging studies [101, 102, 103] have shown that blood flow has a right hand helical pattern around the ascending aorta and aortic arch at the beginning of systole: thus the most salient information being contained in the x-axis of gyroscope, which represents rotational velocity around the head-to-foot axis

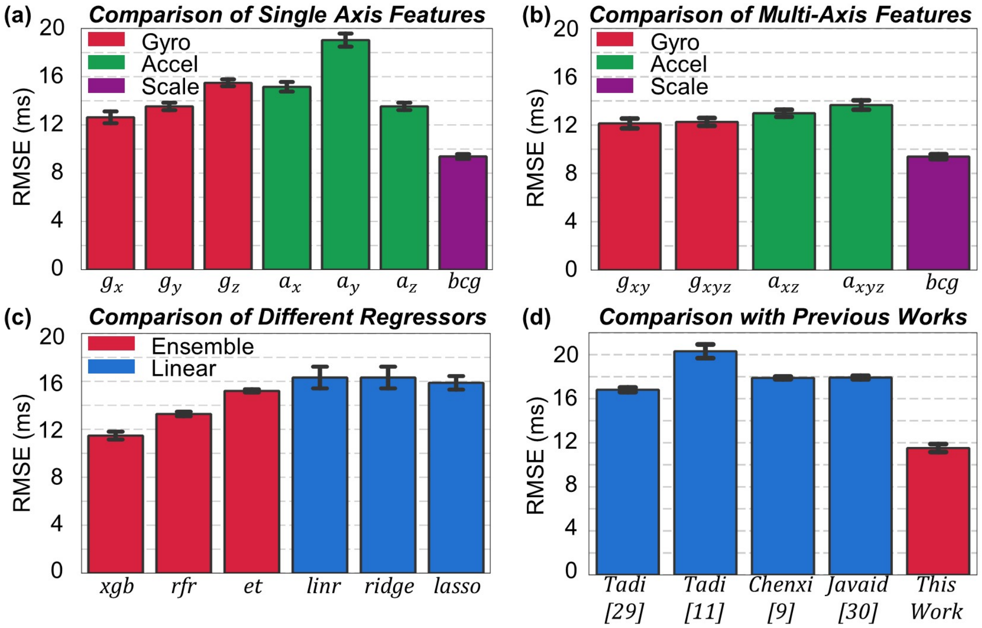

Figure 4.5: (a) Comparison of RMSE in estimation of PEP using features from single axes of gyroscope and accelerometer placed on the mid sternum, with RMSE in estimation using BCG features as a reference. (b) Comparison of RMSE in PEP estimation using combination of features from multiple axes of the gyroscope and accelerometer, with RMSE from BCG features as a reference. (c) Comparison of RMSE for PEP estimation using different regression techniques. (d) Comparing RMSE in estimated PEP from our method with RMSE calculated, using algorithms from recent literatures.

of the body, is as expected. Combination of axes from both the gyroscope and accelerometer reduced the RMSE compared to single axis results ($p<0.05$) (Fig. 4.5 (b)). For the gyroscope, combining the x and y axes provided lower RMSE than all three axes combined ($p<0.05$), which suggests that adding features from the z-axis actually increases the error in estimation of PEP; accordingly, the z-axis is not providing substantial information regarding PEP. In case of the accelerometer, combination of x and z axes provided the lowest RMSE compared to the combination of all three axes ($p<0.05$), which suggests that the y-axis from the accelerometer is not providing useful information regarding PEP. When axes from both the gyroscope and accelerometer were combined, results show that the combination of x and y axes of the gyroscope and x and z axes of the accelerometer is providing the lowest RMSE of 11.46±0.32 ms from all the axes and combination ($p<0.05$), whereas combination of all the axes from both the sensors yields RMSE of 11.79±0.44 ms. This result is supported by the feature ranking of the best 15 features in estimating PEP, shown in Fig. 4.6, where there are no features from the z-axis of the gyroscope and y-axis of the accelerometer.

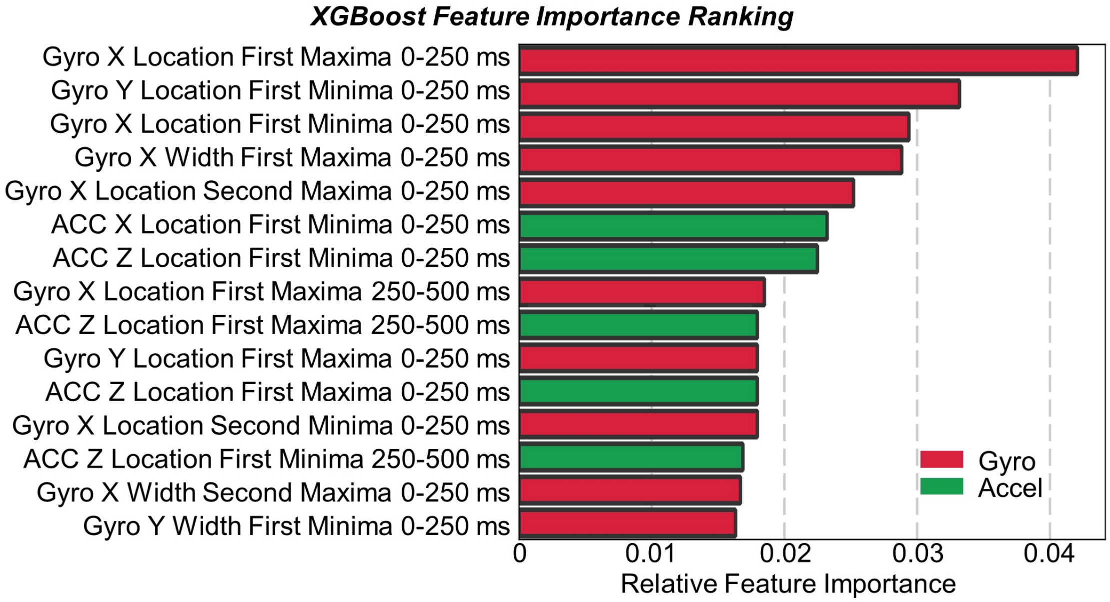

Figure 4.6: Ranking of the best 15 features from gyroscope (Gyro) and accelerometer (ACC) in estimating PEP.

This feature ranking also shows that, out of 15 most contributing features in estimating PEP, 10 features are from the gyroscope; this suggests that the gyroscope is contributing more to PEP estimation compared to the accelerometer, in accordance with the work of Migeotte et al. [59]. One interesting finding is that three out of 15 features are widths of different peaks, which is suggesting that not only peak locations but also peak widths should be considered in PEP estimation. Finally, three out of 15 features are from the diastolic portion of the signals, which will require further studies to understand.

4.4.4 Comparison of Different Regression Technique

We hypothesized that non-linear regression models such as XGBoost regression would perform better than linear regression models for estimating PEP from SCG features. To address this hypothesis, we compared results obtained from the XGBoost regression on the combination of axes (x and z axes of the accelerometer and x and y axes of the gyroscope, which showed the lowest cross-validated RMSE) to the same combination (same feature set) but using other regression models.

We compared XGBoost regression to ordinary linear, Ridge, Lasso, random forest (RF) and extra trees (ET) regression techniques. Ordinary linear, Ridge and Lasso are all linear regression techniques, whereas XGBoost, RF and ET are ensemble learning algorithms. Ensemble methods using regression tree estimators can fit complicated non-linear functions robustly compared to linear models.

For Ridge and Lasso, the regularization parameter was varied between 10_{-3} to 10_2 logarithmically. For RF and ET, regressors contained 200 trees and column sampling factor was chosen as 0.5, similar to the XGBoost model parameters. For these ensemble models, each tree was trained on a subset of features consisting of features. The cross-validated RMSE results were compared for the different regression models, keeping the same features and dataset and only the regression technique was altered.

As hypothesized, XGBoost produced the lowest RMSE (Fig. 4.5 (c), $p<0.05$) when different regression techniques were compared. Ordinary least squares regression resulted in an RMSE that was 4 ms higher ($p<0.05$) compared to XGBoost. Linear regression results does not improve with the introduction of L2 regularization via Ridge regression. Fig. 4.5 (c) is showing the result only for ridge=1. However, results did not change substantially for the range of ridge values tested. L1 regularization via Lasso regression decreases RMSE results by only 0.2 ms ($p<0.05$). Out of the three ensemble methods tested, RF regression performed better than ET regression ($p<0.05$), while XGBoost performed the best.

As hypothesized, the relation between the extracted SCG features and PEP was better characterized by non-linear models rather than linear ones, used in existing literature. Ensemble methods produced lower RMSE compared to linear methods. Automatic feature selection performed by the ensemble methods might be more effective than intrinsic feature selection (due to shrinkage of regression coefficients) used in L1 or L2 regularization.

4.4.5 Comparison with Algorithms from Existing Literature

Fig. 4.5 (d) shows the comparison of RMSE in estimating PEP using features via algorithms from recent publications. As expected, PEP estimation using specific points on the accelerometer or gyroscope is providing higher (more than 30%) RMSE compared to our PEP estimation using combination of x and y axes of the gyroscope and x and z axes of the accelerometer ($p<0.05$). RMSE was similar ($p>0.05$) for PEP estimation models based on features following Javaid et al. [95] and Yang et al. [78].

These results demonstrate that emphasizing specific points (as in the existing literature) from the accelerometer or gyroscope signal in estimating PEP can increase the error of estimation in a global model, due to intersubject variation and complex morphology of the signals. As a result, these approaches may not be applicable as a universal model across subjects or across studies. As an alternative, our work suggests that general time domain features from these signals can provide necessary information regarding PEP and constitute a better-performing global model, which can reduce the complexity in feature extraction techniques. Another point to note is that, in all four algorithms, researchers used one peak/point from a single axis in the accelerometer or gyroscope signal, whereas we are using combination of features from multiple axes from both the sensors.

4.5 Conclusion and Future Work

In this work, we have compared gyroscope and accelerometer based SCG signals and developed a global model to estimate PEP and compared our estimation with the ground truth PEP extracted from a simultaneously-recorded ICG signal. We have demonstrated that the combination of general time domain features from multiple axes of both accelerometer and gyroscope provides a better estimation of PEP compared to the use of specific locations or patterns from single axes of these sensors due to intersubject variability in these signals. In the case of individual sensors, the gyroscope provided more valuable information regarding

PEP compared to the accelerometer for our dataset, when the sensors are placed on the mid sternum. It was also shown that the relationship between SCG signal features and PEP can be modelled using ensemble learning techniques to develop the universal model. Finally, this work highlights the advantages of sensor fusion for developing wearable sensors to monitor cardiac health.

In this work, we collected data from healthy subjects and used the signals acquired from the mid sternum only. Future work should look at the signals from different locations and data from patients with cardiovascular diseases as well to assess how the model performs with higher intersubject variability and take necessary measures to obtain more accurate estimation of PEP. Exercise signals were not used for PEP estimation in this work. Future work should focus on exercise data to assess the possible estimation of PEP during movement with these regression methods. Gravity vector projection on different postures was not considered in this work. Future work can take this into account and can use this as a feature in the prediction model to see if it improves the prediction accuracy. Future work should also focus on estimation of left ventricular ejection time, stroke volume, and other cardio-mechanical parameters. In this work, we explored the relationship between PEP and features from the diastolic portion of both accelerometer and gyroscope signal. Future work can be conducted to investigate the underlying mechanisms.

CHAPTER 5

WEARABLE PATCH-BASED ESTIMATION OF OXYGEN UPTAKE AND ASSESSMENT OF CLINICAL STATUS DURING CARDIOPULMONARY EXERCISE TESTING IN PATIENTS WITH HEART FAILURE

5.1 Overview

The aim of this work is to estimate oxygen uptake (VO_2) from cardiopulmonary exercise testing (CPX) using simultaneously recorded seismocardiogram (SCG) and electrocardiogram (ECG) signals captured with a small wearable patch. CPX is an important risk stratification tool for patients with heart failure (HF) owing to the prognostic value of the features derived from the gas exchange variables such as VO_2. However, CPX requires specialized equipment, as well as trained professionals, to conduct the study.

We have conducted a total of 68 CPX tests on 59 patients with HF with reduced ejection fraction (31% women, mean age 55±13 years, ejection fraction 0.27±0.11, 79% stage C). The patients were fitted with a wearable sensing patch and underwent treadmill CPX. We divided the dataset into a training–testing set (n=44) and a separate validation set (n=24). We developed globalized (population) regression models to estimate VO_2 from the SCG and ECG signals measured continuously with the patch. We further classified the patients as stage D or C using the SCG and ECG features to assess the ability to detect clinical state from the wearable patch measurements alone. We developed the regression and classification model with cross-validation on the training–testing set and validated the models on the validation set. The regression model to estimate VO_2 from the wearable features yielded a moderate correlation (R^2 of 0.64) with a root mean square error of 2.51 ± 1.12 $mL \cdot kg^{-1} \cdot min^{-1}$ on the training–testing set, whereas R^2 and root mean square error on the validation set were 0.76 and 2.28 ± 0.93 $mL \cdot kg^{-1} \cdot min^{-1}$, respectively. Furthermore, the classification of clinical state yielded accuracy, sensitivity, specificity, and an area under the receiver operating characteristic curve values of 0.84, 0.91, 0.64, and 0.74, respectively, for the training–testing set, and 0.83, 0.86, 0.67, and 0.92, respectively, for the validation set.

The result from this work shows that wearable SCG and ECG can assess CPX VO_2 and thereby classify clinical status for patients with HF. These methods may provide value in the risk stratification of patients with HF by tracking cardiopulmonary parameters and clinical status outside of specialized settings, potentially allowing for more frequent assessments to be performed during longitudinal monitoring and treatment.

5.2 Introduction

A hallmark symptom of heart failure (HF) is exercise intolerance, which often manifests through exertional dyspnea and fatigue. The degree of exercise intolerance is captured by subjective assessments (New York Heart Association functional class), quality of life questionnaires (e.g., Kansas City Cardiomyopathy Questionnaire, Minnesota Living with Heart Failure questionnaire), and/or various objective exercise measures (e.g., 6-minute walk distance). Cardiopulmonary exercise testing (CPX) is the most comprehensive exercise test performed in clinical settings to quantify the degree of myocardial impairment and pulmonary dysfunction [104, 105].

CPX has also evolved as an important diagnostic and prognostic tool to manage patients with HF by elucidating mechanisms of exercise intolerance, quantifying disease progression, and facilitating recommendation for advanced therapies, such as heart transplantation or ventricular assist device implantation [104, 105, 106, 107]. Peak oxygen uptake (VO_2), the slope of minute ventilation (VE) and carbon dioxide production (VCO_2) and VO_2 at the anaerobic threshold are key CPX parameters that are used for this risk stratification and disease status quantification. Although CPX is a valuable diagnostic and prognostic tool, it requires a specialized environment and trained professionals to conduct the study. Accordingly, although the information gained from CPX is valuable for patient assessment and titration of care, longitudinal CPX for patients with HF is cost-prohibitive, inconvenient, and thus not feasible on a large scale. Using novel wearable technology, an unobtrusive and inexpensive alternative to the CPX, with the ability to potentially garner similar information as CPX from daily activities in home settings, could improve the remote monitoring and management of patients with HF.

Recently, our team has developed a wearable device [77] capable of measuring electrocardiogram (ECG) and seismocardiogram (SCG) signals and atmospheric sensing (atmospheric temperature, pressure, and humidity) and tested it in patients with HF [23]. The SCG represents the chest wall movements associated with the movement of blood in the heart and includes features representing the ejection of blood through the aorta [39]. Our recent studies have shown that clinical status—degree of myocardial dysfunction and ability to augment cardiac output for patients with HF—can be assessed using SCG after exercise via pre-ejection period estimation and novel machine learning methodology [23, 76, 69]. However, although these results were promising, no group has demonstrated to date that an HF clinical state can be accurately classified using wearable SCG and ECG signals or that key parameters of cardiopulmonary function can be quantified from these signals.

In this work, we recorded ECG and SCG signals using an updated version of the previously validated wearable patch [77] simultaneously with CPX for patients with HF with reduced ejection fraction (HFrEF). We extracted multiple features from these wearable signals and estimated VO_2 continuously throughout the course of exercise using state-of-the-art regression algorithms. We then classified the clinical state of the patients based on the changes in wearable signals associated with the exercise and compared the accuracy of this classification against gold-standard clinical assessment based on CPX. The methodology of this work can be translated into monitoring cardiopulmonary health in patients with HF for longitudinal remote home monitoring. Fig 5.1 shows a hypothetical system for longitudinal monitoring of patients with HF using our wearable patch.

Following the work on estimating VO_2 continuously using our custom-built wearable

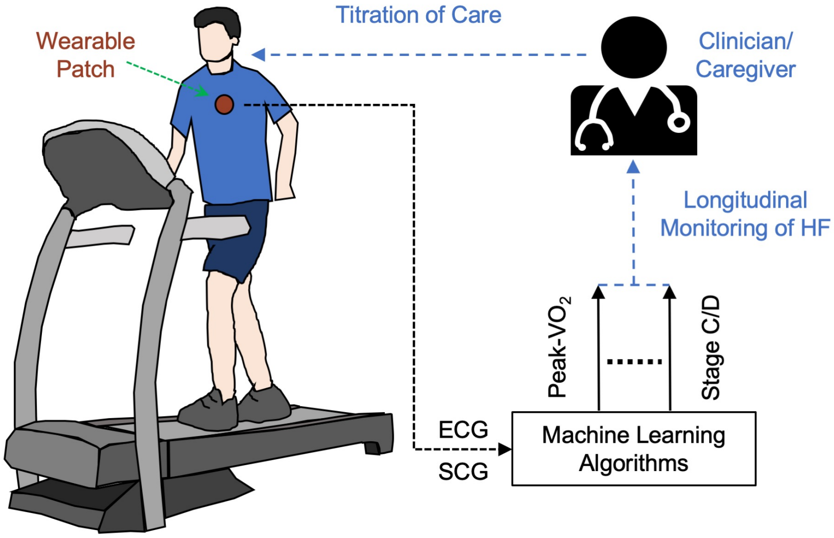

Figure 5.1: Illustration of our envisioned three-step process for longitudinal monitoring of HF patients: 1) Recording of SCG and ECG signals using a custom-built wearable patch during exercise and daily activities. 2) Estimation of cardiopulmonary gas exchange variables and prediction of the clinical state of HF (stage C or D). 3) Intervention by a clinician based on the longitudinal assessment of cardiopulmonary parameters and HF status (future work).

patch, throughout the course of CPX for patients with HF, we translated similar methodology to estimate VO_2 in a minimally controlled outdoor walking environment and in a controlled treadmill exercise environment in healthy individuals. The follow-up study was carried out to showcase the efficacy of the methods of the CPX study with wearable SCG and ECG in tracking changes in VO_2 in a daily living scenario. The follow-up study is another important step towards facilitating remote monitoring of cardiopulmonary health.

5.3 Methods for CPX Study

5.3.1 Experimental Protocol

The CPX study in patients with HF was conducted under a protocol reviewed and approved by the University of California, San Francisco, and the Georgia Institute of Technology Institutional Review Boards. All patients provided written consent before the procedure.

We have conducted a total of 68 CPX tests in 59 patients with HFrEF (with 9 patients having 2 CPX tests separated by 253±117 days). All of the patients were recruited from the cardiopulmonary stress test laboratory at the University of California, San Francisco. Only patients with HFrEF and a body mass index of less than 40 were considered for this study. We have separated the CPX tests into 2 groups of 44 CPX for a training–testing set and 24 CPX for a separate validation set. The 24 CPX tests for the validation set were obtained after the model was trained on the training–testing set.

Fig 5.2 (a) illustrates the experimental setup and placement of different sensors on each patient. Before starting the procedure, normal skin preparation methods were administered, and ECG leads were attached in a 12-lead ECG configuration. A gas exchange mask (Medgraphics) was placed on the patient. A finger pulse oximeter, a forehead pulse oximeter, and a blood pressure cuff were placed, and minimal baseline spirometry data were collected to measure forced and slow vital capacity. The custom-built wearable device was placed just below the suprasternal notch. After placing all the sensors, all wires were taped down such that the patient could perform the protocol comfortably.

All CPX tests were performed on a treadmill (GE T2100) per the American College of Cardiology/American Heart Association Guidelines [108] and following the modified Naughton protocol [109]. Tests were terminated owing to general or leg fatigue, shortness of breath, angina, dizziness, or electrocardiographic evidence of ischemia or arrhythmia. Breath-by-breath measurements of respiratory rate, VE, VO_2, VCO_2, partial pressure of oxygen, and partial pressure of carbon dioxide were collected at rest, at zero grade low-speed walk, during exercise, and during recovery. Heart rate (HR), rhythm, and oxygen saturation were continuously monitored with intermittent sphygmomanometry. ECG and SCG signals were obtained continuously using the wearable patch.

As an outcome of the CPX tests, patients were classified as American College of Cardiology/American Heart Association stage C HF (n=54) or stage D HF (n=14) based on the recommendations from 2 HF physicians (Dr. Teresa De Marco and Dr. Liviu Klein from

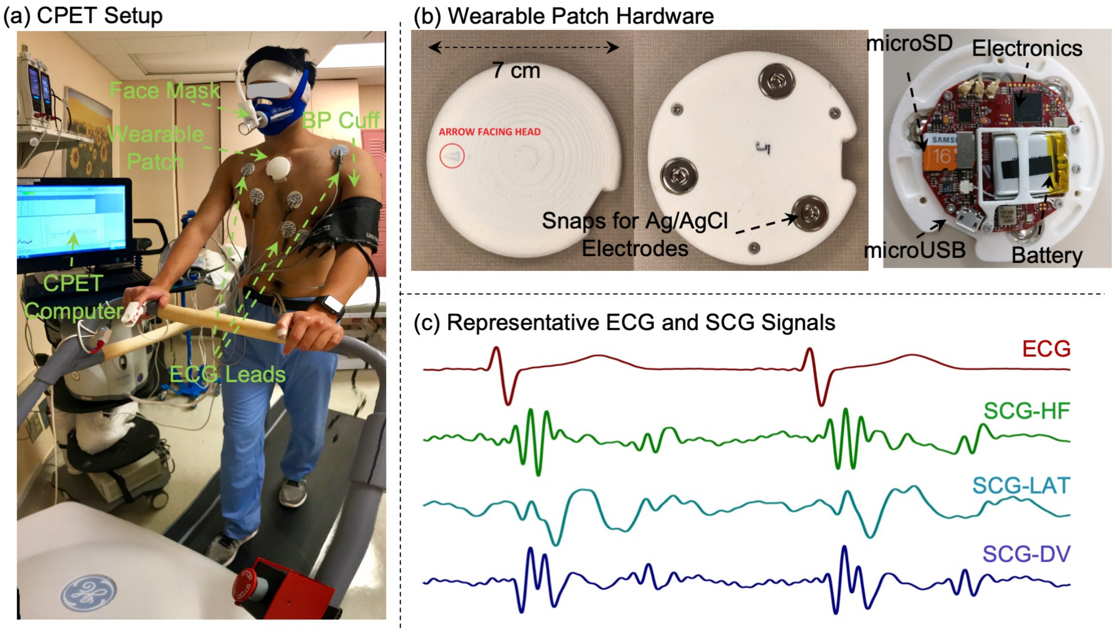
(a) CPET Setup

(b) Wearable Patch Hardware

(c) Representative ECG and SCG Signals

Figure 5.2: Experimental setup with wearable patch hardware and representative cardiogenic signals. (a) The experimental setup with the patient walking on a treadmill, with all the cardiopulmonary exercise testing measurement sensors and wearable patch attached to the body. (b) The wearable patch top and bottom view with snaps for electrocardiogram (ECG) electrodes and internal hardware. (c) Representative ECG and triaxial SCG signals (head-to-foot [HtoF], dorsoventral [DV], and lateral [LAT]) from 1 patient in the study.

UCSF), following standard guidelines [108, 110, 111]. Patients were classified as stage D HF if they were recommended for a heart transplant or ventricular assist device implant based on their peak VO_2 ($<$14 mL/kg/min or $< 50\%$ predicted if women or obese) and VE/VCO_2 ratio ($>$38 if respiratory exchange ratio was $<$1.05).

5.3.2 Sensing Hardware

Breath-by-breath data were collected using MGC Diagnostic/Medgraphics Ultima Series with Breeze suite 8.1.0.54 SP7 (software version number). ECGs (12-lead) were collected using GE Case V6.72. Pulse oximetry was measured using Radical 7 Masimo Rainbow Set.

For all patients, the wearable ECG and 3 axis SCG signals (head-to-foot [HtoF], dorsoventral [DV], and lateral [LAT]) were collected with a novel wearable patch as shown in Fig.

1B. This patch is an improvement upon our previous version, as described in [77]. It contains an ATSAM4LS microcontroller (Atmel Corporation, San Jose, CA), whereas the previous version used an ATmega1284P microcontroller (Microchip Technology, Chandler, AZ). The ECG sensor uses an analog-front-end-integrated circuit with an on-board analog-to-digital converter ADS1291 (Texas Instruments, Dallas, TX). The accelerometer in the present patch that acquires triaxial SCG signals is the ADXL355 (Analog Devices, Norwood, MA), which has a low noise floor of 25 μg/$\sqrt{Hz}$ compared to the triaxial accelerometer BMA280 (Bosch Sensortech GmbH, Reutlingen, Germany) used in the previous version [77] with a noise floor of 120 μg/$\sqrt{Hz}$. The patch also contains a BME280 (Bosch Sensortech GmbH, Reutlingen, Germany) environmental sensor which records atmospheric pressure (AP), ambient temperature and relative humidity, whereas the previous version [77] had only pressure sensing capability using the MS5611-01BA03 (Measurement Specialties, Fremont, CA). The patch used in this work has a diameter of 7 cm and weight of 38.2 gm. When fully charged, it can record continuously for approximately 45 hours, which is more than sufficient for constant remote monitoring. Initially it samples the ECG signal at 1kHz, the accelerometer signals at 500 Hz and the environmental signals at 20 Hz, and saves the data into a SD card in the patch. A custom-built graphical user interface accesses all the data into a computer and resamples the accelerometer and environmental signals at 1 kHz to have the same sampling frequency of 1 kHz for all the signals. Fig 5.2 (c) shows representative ECG and triaxial SCG signals from the wearable patch. Fig 5.3 illustrates the overall workflow used in this work.

5.3.3 Data Analytics Techniques for Reducing Noise and Extracting Features from the Wearable SCG and ECG Signals

Whereas the CPX equipment captures breath-by-breath VO_2 data, the wearable patch captures one data point every 0.001 second (1 kHz sampling rate). A sliding window approach was used to combine all of the values from the SCG and ECG signals for the period in

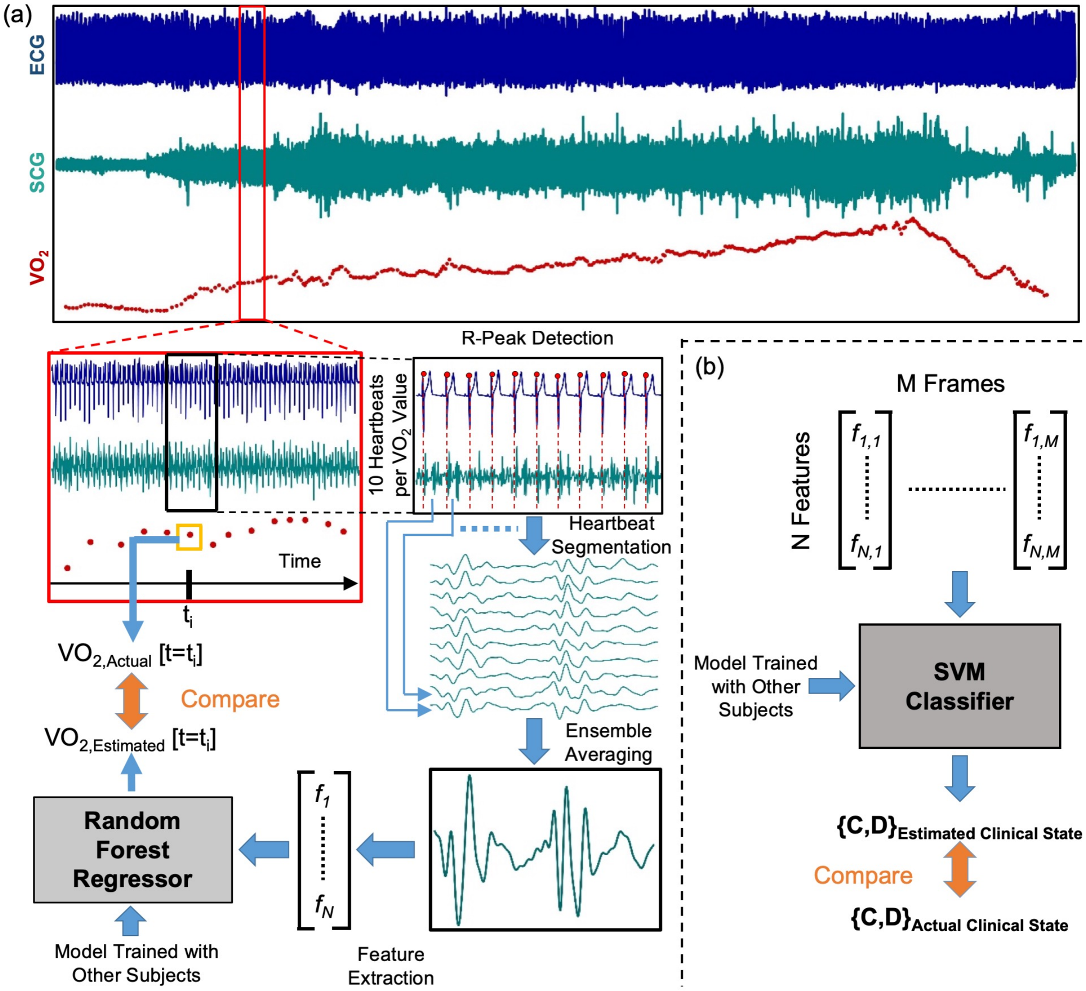

Figure 5.3: Overview of the regression and classification techniques. (a) Wearable ECG and seismocardiogram (SCG) (only showing 1 axis of the signal for simplicity) signals were synchronized with breath-by-breath data from the CPX computer. R-peaks of the ECG signal were detected, and the SCG signals were segmented into heartbeats using corresponding R-peaks. Ten heartbeat frames from the SCG signals were averaged to get ensemble-averaged heartbeats corresponds to 1 oxygen uptake (VO$_2$) value from breath-by-breath data from CPX, and features were extracted from the averaged heartbeats. The features were fed into a Random Forest regressor as estimators to estimate VO$_2$. Estimated VO$_2$ was compared with actual VO$_2$ to see the estimation accuracy. (b) The features from SCG and ECG were fed into a support vector machine (SVM) classifier with radial basis function kernel to estimate the clinical state of a patient and it was compared with the actual clinical state derived from CPX.

between breaths to estimate a single VO$_2$ value to compare against the gold standard. At a high level, the approach to estimating VO$_2$ was as follows: (1) the signals were preprocessed using our existing data analytics algorithms for SCG and ECG signals to decrease motion artifacts and other noise; (2) representative features, or signal characteristics, we hypothesized to be relevant for VO_2 estimation were extracted from the SCG, and ECG signals; and (3) regression models were trained to mathematically estimate VO_2 from these SCG and ECG signal features for all CPX instances in the training–testing set and later validated in the validation set.

Preprocessing and ECG Artifact Removal: All the signals from the wearable patch were synchronized with the breath-by-breath data from the CPX computer. The raw ECG and SCG signals from the wearable patch were digitally filtered (cut-off frequencies: 0.5–40.0 Hz for the ECG and 1–40 Hz for the SCG signals) to remove out-of-band noise. After filtering, a fourth SCG signal (SCGMag) was computed using vector summation on the 3 axes of the SCG. All the wearable signals were inspected for motion artifacts, and portions of the signals corrupted by motion artifacts were excluded from the analysis.

Motion artifacts in the ECG signal can pose a major challenge to subsequent signal processing and regression steps. Accordingly, an algorithm was implemented to detect and remove artifact-corrupted segments of the signal automatically. Specifically, the ECG for each 30-second-long frame was passed through an artifact detection function to choose the window frame (i.e., length) of signal that is artifact-free (Fig 5.4). First, the upper (E_u) and lower (E_l) envelope of the data is detected and a difference E_d ($= E_u - E_l$) is computed. Then, the mean (μ) and standard deviation (σ) of E_d throughout the recording is calculated. An artifact is defined as the signal segment when the E_d of that specific portion is greater or less than 3σ from the μ. The longest artifact-free segment of the signal was chosen, and the time stamp for this portion was used to segment all the wearable signals to obtain the signals where high-quality ECG was present.

The ECG R-wave peaks were detected using a simple thresholding based peak detection method. The four SCG signals (SCG_{HtoF}, SCG_{LAT}, SCG_{DV}, and SCG_{Mag}) were segmented into individual heartbeats using the R-peaks from the ECG signals. Each heartbeat

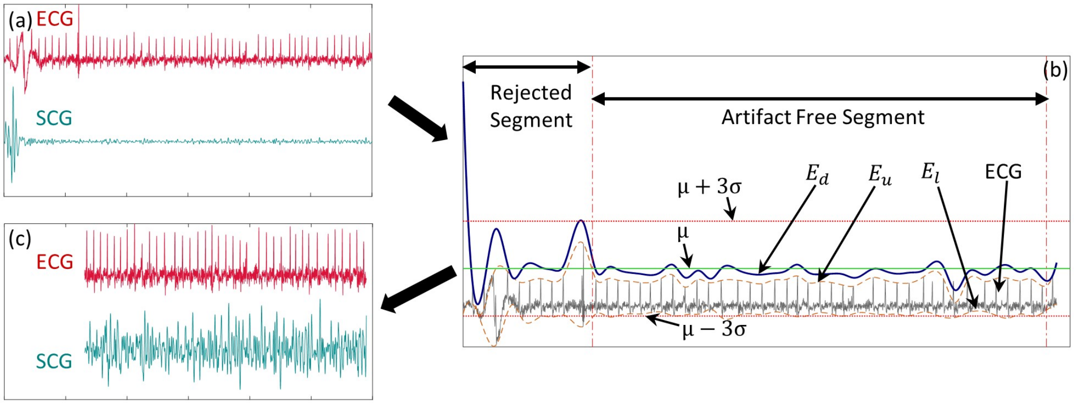

Figure 5.4: Automatic artifact removal of ECG: (a) Filtered ECG and SCG signals. (b) ECG is passed through artifact detection algorithm. Segments with artifacts are chosen when the difference (E_d) of upper (E_u) and lower (E_l) envelope of the signal is outside the range of mean (μ) $\pm$ 3$\times$standard deviation (σ) of E_d. The longest artifact free signal segment is chosen and the time stamp of the start and end of that segment is calculated. (c) Both ECG and SCG signals are segmented with the time stamps from the previous step, where the ECG was found to be artifact free.

was windowed to a 600-ms duration from the R-peak. For each SCG signal, 10 consecutive heartbeats surrounding 1 VO_2 measurement from the CPX hardware were averaged time-point by time-point to obtain an ensemble-averaged heartbeat (Fig 5.3). Ensemble-averaged heartbeats were computed across the whole recording with a step size of 1 heartbeat. Ensemble averaging was used to reduce noise and motion artifacts within each heartbeat [85]. This process resulted in a total of 46,673 ensemble-averaged heartbeats from 44 CPX instances in the training–testing set and 28,230 ensemble-averaged heartbeats from 24 CPX instances in the validation set. For each ECG signal, the R-to-R interval and instantaneous HR were calculated for each heartbeat and averaged in the same way as the ensemble-averaged waveforms. The average VO_2 measurements corresponding to each ensemble-averaged heartbeat were computed to be used as the target variables for each ensemble-averaged heartbeat (i.e., the output variables against which the regression model was trained).

Feature Extraction: The next step toward estimating VO_2 from the measured signals involved extracting multiple features—or characteristics—that could then be input to a machine learning regression algorithm. A total of 17 frequency-domain features were automatically extracted from each of the four SCG signals resulting in a total of 68 SCG features per ensemble-averaged heartbeat. The SCG features extracted were as follows: total band power (0-500 Hz), and band power in 3 Hz bandwidth frequency ranges from DC to 30 Hz. Additional frequency domain features were: the highest prominent frequency (fp1), second prominent frequency (fp2), and third prominent frequency in the power spectral density (PSD), and the amplitudes of the PSD at fp1, fp2, and fp3.

For prominent frequency, peaks in the PSD of the frame were ranked according to their amplitudes, and the highest, second-highest, and third-highest amplitudes were used to locate the first, second, and third prominent frequency accordingly. The averaged R-to-R interval and instantaneous HR for each averaged heartbeat were used as ECG features.

SCG Outiler Heartbeat Removal: Before training a regression model to estimate VO_2, we removed outlier beats from the ensemble-averaged SCG heartbeats using the Mahalanobis distance [112]. For each subject, the first 50 averaged frames from the rest signal were assumed as baseline frames and all the features (for a particular feature set) of the 50 frames were averaged to create baseline feature distribution. The Mahalanobis distance [112] was calculated between the baseline feature distribution and each averaged heartbeat frame for a particular subject. The underlying hypothesis was that the wearable signal would change in morphology with various intensity of exercise, and it would vary the most at peak exercise compared to baseline, which would be reflected by the Mahalanobis distance. The first and third quartile (Q_1 and Q_3) were extracted, and the interquartile range (IQR) was calculated as $IQR=Q_3-Q_1$, for subject-wise distribution. A particular frame was considered as an outlier if the Mahalanobis distance of the frame is lower than ($Q_1-1.5\times IQR$) or higher than ($Q_3+1.5\times IQR$) of the distribution. These outlier frames and corresponding target variables were removed from the dataset. The distance calculated for each frame was used as a feature in the regression model, which makes the total number of features equal to *f+1*. The signal processing and feature extraction were performed in Matlab 2018a.

5.3.4 Regression and Classification

Regression Model: For each VO_2 measurement recorded by the CPX equipment, a corresponding set of features from the SCG signals was derived using methods described elsewhere in this article. A regression algorithm was then designed and trained on the training set to mathematically estimate VO_2 from this set of features using part of the recorded data as a training set and the remainder of the data as a testing set. Specifically, we trained a Random Forest (RF) [113] regression algorithm to estimate VO_2 from the wearable signal features and used leave-one-subject-out (LOSO) cross-validation [114] to evaluate the estimation accuracy. For all 44 CPX instances in the training–testing set, at each fold—or iteration of the cross-validation process—an RF regression model was trained on the data from 43 patients (thus leaving 1 CPX instance out) to learn the relationship between features from the wearable sensors and the target variable VO_2. The resulting trained model was then used to estimate the corresponding VO_2 values for the heartbeat frames from the left out CPX instance. This procedure was repeated 43 more times, leaving a different CPX instance out each time. This cross-validation method was used to develop a global regression model with optimized hyperparameters on the data in the training–testing set only. For the validation of the global model, the regression model (with the optimized hyperparameters) was trained on the whole training–testing set (all 44 CPX instances) and tested on the separate validation set (with 24 CPX instances). As a result, we obtained predictions of all target variables from all ensemble-averaged heartbeats, from all 68 CPX instances.

Two figures of merit that are commonly used in the existing literature were used to evaluate the regression model and approach. First, the root mean squared error (RMSE) was calculated for each left out CPX instance: specifically, the error between the estimated VO_2 values and the CPX equipment measured VO_2 values across all breaths. The cross-validated RMSE was then calculated as the average of the RMSE scores from 44 folds in the training–testing set and 24 CPX instances in the validation set. Second, the coefficient of determination (R^2) between the true values and the cross-validated predictions of VO_2 across all CPX instances were calculated for the training–testing set and the validation set separately.

To assess the benefit of using a combined SCG/ECG approach for predicting VO_2, the RF regression approach was repeated for 3 different feature sets: the SCG features only, the ECG features only, and the combined SCG and ECG features. We compared the resulting cross-validated RMSE scores to assess the performance of each feature set to estimate VO_2. We performed statistical analysis on the cross-validation results from the different feature sets.

To understand the value of the information provided by SCG signals and our machine learning algorithm compared with the ECG-derived HR for estimating instantaneous VO_2, we trained an RF regression model using SCG signal features alone and a second model with HR alone using a simple linear regression model as used in literature to investigate the VO_2–HR relationship [115, 116]. We performed the same LOSO cross-validation and calculated the cross-validated RMSE. We performed statistical analyses on the cross-validation results to compare the SCG signal feature-based model with the HR-based model.

Classification: In addition to estimating VO_2 using regression, we aimed to assess the ability to classify each patient's clinical status based on the wearable sensing data measured during treadmill exercise using classification. We used a machine learning classification technique to classify the patients with HF as stage C or stage D on a particular CPX procedure day using the wearable measurement alone and compared the estimated class with the true class based on the CPX outcome. Specifically, a support vector machine classifier with a radial basis function kernel [117, 118] was used, and classification performance was evaluated using LOSO cross-validation in the training–testing set and later validated on the separate validation set similarly as described in the regression model section. We preprocessed the wearable features before using them in the classifier. The details on the preprocessing of the wearable features for the classifier are given below.

For each subject, ensemble-averaged heartbeats were ranked from lowest to highest using corresponding Mahalanobis distance (described above) for a particular subject and the highest 100 heartbeats were chosen for each subject for further classification analysis, giving us a total of 4400 heartbeats from 44 subjects. The underlying hypothesis of choosing the highest 100 heartbeats was that the subjects were classified based on the peak exercise capacity during CPX, and wearable signal segments correspond to peak exercise capacity would reflect the difference between stage C and stage D subjects. These heartbeats were labeled for each subject based on the true class for that particular subject.

Similar to the regression analysis approach with the training–testing set, for the classification task, the classifier was trained on the features from 43 of the 44 CPX instances to map the features into an output of stage C and D state. We then used this classifier to predict the class of each heartbeat frame for the left-out patient. The majority vote (i.e., class) of the heartbeats was chosen as the predicted class for the patient on that particular CPX procedure day. We repeated these steps 43 more times, leaving a different CPX instance out each time. In this way, we obtained a predicted class for all CPX instances. Similarly, for the validation set, we trained the classification model (with hyperparameters tuned in the training–testing set of the classification task) on all 44 CPX instances in the training–testing set and estimated the class of each CPX instances in the validation set. Finally, we compared the estimated class to the true class of the patients from the corresponding CPX outcome to calculate classification performance for the training–testing and validation set separately. The machine learning techniques for regression and classification were performed using Python 3.6.

Estimation of Peak VO_2: Because the peak VO_2 is among the key parameters extracted from a CPX procedure to assess the clinical status of the patients, we tried to see how our regression model, which estimates instantaneous VO_2, can be used in estimating peak VO_2 as well. The maximum of the estimated VO_2 values for a particular CPX instance was used as the estimated peak VO_2 value for that CPX and compared with the true measured peak VO_2 from corresponding CPX procedure, in a correlation and a Bland–Altman analysis. We have calculated the percentage error between estimated and true values of peak VO_2 and reported the average of the percentage error. We have used values from all 68 CPX instances, including both the training–testing and the validation CPX instances.

Peak HR-Based Regression and Classification: To understand the potential added value from SCG signals and our machine learning approach beyond peak HR alone, we have directly studied peak HR-based correlation and classification for the same dataset. We performed a simple correlation analysis (without any cross-validation) between peak VO_2 and peak HR. Further, we also applied exactly the same methodology (regression model with cross-validation) as for SCG-based peak VO_2 estimation and formed a model for estimating peak VO_2 from peak HR alone. In addition to the regression analysis, we classified the patients based on peak HR alone into stage C and stage D, in exactly the same manner we applied to our SCG-based features.

5.3.5 Statistical Analysis

We performed statistical analysis on the cross-validated RMSE results to compare regression results from different feature sets. Multiple comparison tests were performed on the RMSE results from the cross-validation. The Friedman test was performed to detect if statistical differences exist, and the Wilcoxon signed-rank test was performed in post hoc testing for pairwise comparison. Additionally, for the post hoc testing, Benjamini–Hochberg correction for multiple comparison was performed on the *P* values. The demographics of patients in stage C and stage D were compared using the Student t-test. In this work, *P* values of less than .05 were considered statistically significant.

5.4 Methods for Healthy Subject Study

5.4.1 Experimental Protocol and Hardware

For the follow-up study with healthy individuals, we conducted the study under a protocol (H18452) approved by the Georgia Institute of Technology Institutional Review Board. A total of 17 healthy subjects (9 females and 8 males) participated in the study (Age: 26.8 ± 4.1 years, Weight: 67.5 ± 14.1 kg and Height: 170.5 ± 9.9 cm). All subjects provided written informed consent before experimentation and reported no cardiopulmonary issues.

To record the gold-standard VO_2 for this follow-up study, we used a COSMED K5 (COSMED, Rome, Italy) metabolic system. The same wearable patch, used in the CPX study, was used in this follow-up study with healthy individuals. Fig. 5.5(a) shows the placement of both sensors: our custom-built wearable patch and the COSMED K5 metabolic system. Fig. 5.5(b) shows the custom-built wearable sensor hardware, which measures ECG, triaxial SCG, and environmental features (atmospheric pressure, temperature, and humidity). For each subject, we placed the wearable sensor evenly between the suprasternal notch and xiphoid process on the mid-sternal line, using three ECG electrodes (model 2670, 3M, Saint Paul, MN, USA). For the COSMED K5 system, we fitted subjects with a gas exchange mask on their face and the K5 system on their back. We situated a heart rate belt from the K5 system just below the chest line. After fitting subjects with all the sensors and systems, we asked them for confirmation of their comfort before testing. At the start of each trial, we synchronized both the wearable sensor and K5 system to a smart mobile phone in order to record timestamps throughout the protocol.

Fig. 5.5(d) shows the outline of the study protocol, which we divided into two parts: a treadmill walking portion in a laboratory setting and an outdoor walking portion in an uncontrolled setting. For the treadmill part of the protocol, subjects first stood still for two minutes to record baseline data. Then, subjects walked on a treadmill at five different speed settings (0.75, 1, 1.25, 1.5 and 1.75 meters/second, roughly 1.7, 2.2, 2.8, 3.4 and 4

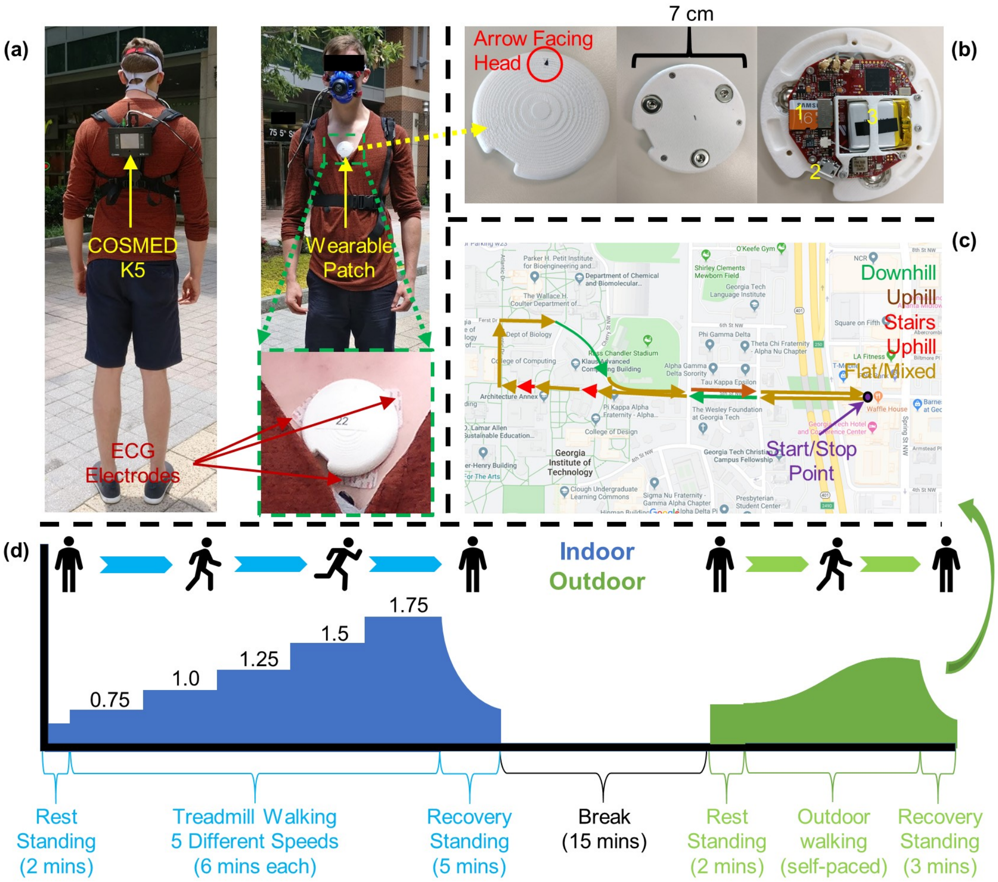

Figure 5.5: (a) A subject configured with both the wearable patch and the COSMED K5 system, with inset showing a zoomed-in image of the ECG electrodes. (b) The wearable patch top, bottom, and inside. The microSD (1), microUSB (2), and battery (3) are shown. (c) A map of the outdoor walking route across Georgia Institute of Technology with marked terrain. (d) An outline of the study protocol.

miles/hour) for six minutes at each speed, totaling 30 minutes of walking. After completing the treadmill walk, subjects stood still for 5 minutes to record a recovery period. Including this recovery period, subjects performed the treadmill protocol continuously for a total of 37 minutes.

After the treadmill part, subjects rested for 15 minutes before starting the outside walking protocol. They began this section standing still for 2 minutes at the "Start/Stop" location of the route marked in Fig. 5.5(c). Then, subjects walked the route shown in Fig. 5.5(c), arriving back at the same "Start/Stop" point. The route contains a mixture of level ground, uphill and downhill walkways (with significant slopes), two uphill stairs climbing, and four traffic signals along the way. The terrain is marked in Fig. 5.5(c). Subjects completed this walk at their own chosen speed and followed normal pedestrian traffic laws. After completing the route, subjects stood still for 3 minutes to record a recovery period. This part of the protocol took approximately 20-30 minutes depending on each subject's speed as well as traffic conditions during their testing. Of 17 subjects, two females were not able to perform the outside walk due to precipitation. For that reason, we obtained data from 17 treadmill protocols and 15 outdoor protocols.

For this study, we recorded the gold standard breath-by-breath (BxB) metabolic data with the COSMED K5 system (COSMED, Rome, Italy). Subjects wore the COSMED heart rate probe (i.e., belt), which provided an HR reading corresponding to the ground-truth metabolic data.

We collected ECG and triaxial SCG (axes: head-to-foot (HtoF), dorso-ventral (DV), and lateral (Lat)), with the same wearable patch described in the method section of the CPX study, shown in Fig. 5.5(b).

5.4.2 Signal Processing and Regression

For signal processing of the BxB data and wearable sensor, we followed similar procedures (ECG artifact removal, heartbeat segmentation, and ensemble averaging), as mentioned for the CPX study. For SCG feature extraction, we extracted a couple of more time and amplitude features on top of the frequency domain features mentioned above in the CPX study.

Using an automated algorithm, we extracted 28 time domain, 17 amplitude, and 17 frequency domain features (62 total) from the ensemble-averaged waveforms for each of the four SCG signals. The list of extracted features is provided in Table. 5.1. We extracted the amplitude and time domain features from the time-domain representation of the SCG signals, and the frequency domain features from the power spectral density (PSD) estimate of the SCG signals. Peaks and valleys in the averaged frames were ranked according to their amplitudes, and the highest and second-highest amplitudes were used. The location was calculated as the distance from the corresponding R-peak in ms. The width was calculated as the width of the peak or valley at half-prominence, in ms. We evaluated different combinations of feature sets for performance in estimating VO_2

Table 5.1: SCG Features Extracted

Signals	Feature Names	Number of Features		
		Ampl.	Time	Freq.
SCG (0-200 ms)	Highest and second highest peak (Ampl., Loc. and Width)	2	4	
	Lowest and second lowest valley (Ampl., Loc. And Width)	2	4	
	Number of peaks and valleys		2	
	First and second peak (Ampl., Loc. And Width)	2	4	
	First and second valley (Ampl., Loc. And Width)	2	4	
	Highest peak of absolute signal (Ampl., Loc. And Width)	1	2	
SCG (200-500 ms)	Highest peak (Ampl., Loc. and Width)	1	2	
	Lowest valley (Ampl., Loc. And Width)	1	2	
	Number of peaks and valleys		2	
	Highest peak of absolute signal (Ampl., Loc. And Width)	1	2	
SCG AUS	(0-100 ms), ..., (400-500 ms)	5		
SCG PSD Band Power	(0-3 Hz), (3-6 Hz), ..., (27-30 Hz) and (0-500 Hz)			11
SCG PSD	First, second and third prominent frequency (Ampl. and Freq.)			6
Single Axis Total		17	28	17
4-Axes Total		68	112	68

Ampl: amplitude, Freq: frequency, Loc: location, AUS: area under signal, PSD: power spectral density.

Regression Model: For the regression model in the follow-up study, we chose an extreme gradient boosting (XGBoost) regression [81] from our initial analysis in this work. XGBoost is a decision-tree based ensemble algorithm that uses a gradient boosting [119] framework. It is an example of an ensemble method [91] that is computationally efficient, parallelizable, able to handle missing values, and able to be pruned/regularized to avoid over-fitting. We fit an XGBoost regressor on the extracted features for all ensemble-averaged heartbeats to estimate corresponding target VO_2 values. We then used this model to estimate VO_2 values for unseen heartbeat frames as represented by the same feature sets. We performed this process with different combinations of feature sets extracted from the SCG, ECG, and AP signals, optimizing hyper-parameters with a grid search. The final hyper-parameters are as follows: learning rate=0.05, max_depth=10, subsample=0.6, colsample_bytree=0.7, n_estimators=100, min_child_weight=2, gamma=0.3. We used Python 3.6 for all machine learning techniques.

Statistical Analysis: We performed the same statistical tests to compare the performance of different feature sets of SCG and ECG to estimate VO_2, as described in the CPX study method section.

5.5 Results and Discussion from CPX Study

Patient demographics and clinical characteristics for the CPX study are detailed in Table 5.2 and CPX characteristics are provided in Table 5.3.

5.5.1 Regression Model Comparison

Fig 5.6 (a) shows the correlation analysis between the actual (measured) VO_2 and the estimated VO_2 using the combined features from SCG and ECG for the training–testing set and Fig 5.7 (a) shows the corresponding analysis for the validation set. For the training–testing set, the regression model with the SCG features only performed better in estimating VO_2 compared with the model using ECG features only: RMSE of 2.55 ± 1.16 $mL \cdot kg^{-1} \cdot min^{-1}$ vs 3.75 ± 1.68 $mL \cdot kg^{-1} \cdot min^{-1}$, respectively ($P< .001$) and a corresponding R^2 of 0.63 vs 0.19. Combining SCG and ECG features improved the estimation accuracy slightly compared with SCG features only, but the improvement was not significant ($P>.05$) with an

RMSE of 2.50±1.12 mL · kg^{-1} · min^{-1} and an R^2 of 0.64.

Table 5.2: Patient Demographics and Characteristics

	All CPX Instances (N=68)	Stage C (n=54)	Stage D (n=14)	*P* Value
Age, years	54.53 ± 12.68	54.81±12.88	53.43±12.28	0.53
Sex				
Male	47 (69%)	40 (74%)	7 (50%)	
Female	21 (31%)	14 (26%)	7 (50%)	
Height, cm	172.4±9.14	172.67±9.34	171.4±8.57	0.59
Weight, kg	87.99±18.39	87.57±17.96	89.59±20.63	0.68
BMI, kg/m$_2$	29.53±5.26	29.27±4.85	30.51±6.73	0.37
Ejection fraction,%	27.25±10.64	26.21±9.29	31.29±14.46	0.13
NYHA class				
I	12 (13%)	12 (18%)	0 (0%)	
II	24 (30%)	22 (36%)	2 (0%)	
III	32 (57%)	20 (45%)	12 (100%)	
Orthopnea	17 (27%)	13 (27%)	4 (27%)	0.73
Bilateral leg edema	12 (20%)	8 (18%)	4 (27%)	0.23
Systolic blood pressure, mmHg	105±15	105±14	102±19	0.41
Diastolic blood pressure, mmHg	68±10	68±9	68±15	0.85
BNP, pg/mL	568.4±722.5 (23∗)	368±514 (17∗)	1136.3±962.1 (6∗)	0.02

Table 5.2: Patient Demographics and Characteristics

	All CPX Instances (N=68)	Stage C (n=54)	Stage D (n=14)	*P* Value
NT-proBNP, pg/mL	1635±1671 (31∗)	1783±1687 (25∗)	1018±1587 (6∗)	0.35
Serum Creatinine, mg/dL	1.40±1.43 (60∗)	1.49±1.61 (46∗)	1.13±0.43 (14∗)	0.38
Loop Diuretics, Furosemide, mg/d	83.7±93.4 (68%)	64±71 (65%)	146.4±128.1 (79%)	0.01
β-blockers, Bisoprolol, mg/d	6.1±3.8 (94%)	5.9±3.9 (93%)	6.7±3.7 (100%)	0.54
ACE-Inhibitors, Lisinopril, mg/d	18.6±15.5 (10%)	18.6±15.5 (13%)	0 (0%)	
ARB, Losartan, mg/d	54.8±30.4 (19%)	61.1±30.9 (17%)	40.6±27.7 (29%)	0.28
ARNI, Sacubitril-Valsartan, mg/d	102.4±64.2 (58%)	101.2±64.8 (61%)	107.7±65.5 (50%)	0.91
MRA, Spironolactone, mg/d	29.8±16.7 (85%)	29.3±15.5 (81%)	31.6±20.7 (100%)	0.64
Subsequent Events (OHT/VAD/Death)[a]	11(16%)	7 (13%)	4 (29%)	0.16

Table 5.2: Patient Demographics and Characteristics

	All CPX Instances (N=68)	Stage C (n=54)	Stage D (n=14)	*P* Value

Values shown are mean±standard deviation or n (% of population) or mean±standard deviation (% of population) unless otherwise indicated. Statistical significance between stage C and D patients in values, where applicable, was evaluated using an unpaired t test or a χ^2 test.

ACE, angiotensin converting enzyme; ARB, angiotensin receptor blocker; ARNI, angiotensin receptor blocker—neprilysin inhibitor; BNP, B-type natriuretic peptide; CPX, cardiopulmonary exercise testing; MRA, mineralocorticoid receptor antagonist; NT-proBNP, N-terminal pro b-type natriuretic peptide; NYHA, New York Heart Association; OHT, orthotopic heart transplantation; VAD, ventricular assisted device implantation.

$*$Number of CPX test instances with available laboratory results.

[a] Subsequent events were recorded up to 6 months after the completion of the study. In the cases where 1 cardiopulmonary exercise testing patient had multiple events (e.g., VAD, followed by transplant later), only the first occurring event was counted as subsequent events for a particular patient.

In the case of the validation set, similar results were obtained using SCG and ECG features separately: RMSE of 2.28±1.04 $\text{mL} \cdot \text{kg}^{-1} \cdot \text{min}^{-1}$ vs 3.52±1.5 $\text{mL} \cdot \text{kg}^{-1} \cdot \text{min}^{-1}$, respectively ($P < .001$) and a corresponding R^2 of 0.76 vs 0.36. Similarly, combining the SCG and ECG features improved the estimation accuracy (RMSE of 2.28±0.93 $\text{mL} \cdot \text{kg}^{-1} \cdot \text{min}^{-1}$ and R^2 of 0.76) slightly compared with SCG features only, although the improvement was not significant ($P > .05$).

In the case of comparing SCG features with ECG-derived HR in estimating instantaneous VO_2, SCG features resulted in a significantly higher R^2 of 0.63 compared with 0.31 using HR only for the training–testing set ($P < .05$), and correspondingly 0.76 compared

Table 5.3: Cardiopulmonary Exercise Test Responses

	All CPX Instances (N=68)	Stage C (n=54)	Stage D (n=14)	P Value
Peak VO_2, ml/kg/min	15.58±4.82	17.21±3.92	9.32±1.93	<0.001
Percent predicted peak VO_2, %	58±21	63±20	37±9	<0.001
VE/VCO_2 slope	33.35±6.65	32.44±6.48	36.82±6.34	0.04
VO_2 at AT, ml/kg/min	11.79±3.95 (62*)	12.92±3.33 (50*)	7.08±2.69 (12*)	<0.001
Peak oxygen pulse, ml/beat	12.02±3.68	12.91±3.47	8.59±2.24	<0.001
Peak respiratory exchange ratio	1.05±0.12	1.07±0.11	0.96±0.12	0.002
Exercise duration, s	672±235	743±200	401±148	<0.001
Peak heart rate, beats/min	120.06±23.8	124.57±22.79	102.64±19.77	0.002

Values shown are mean±SD. Statistical significance between stage C and stage D subjects in values, where applicable, was evaluated using an unpaired t test

*Number of CPX instances with detectable AT points, Modified V-slope method was used to detect the AT points.

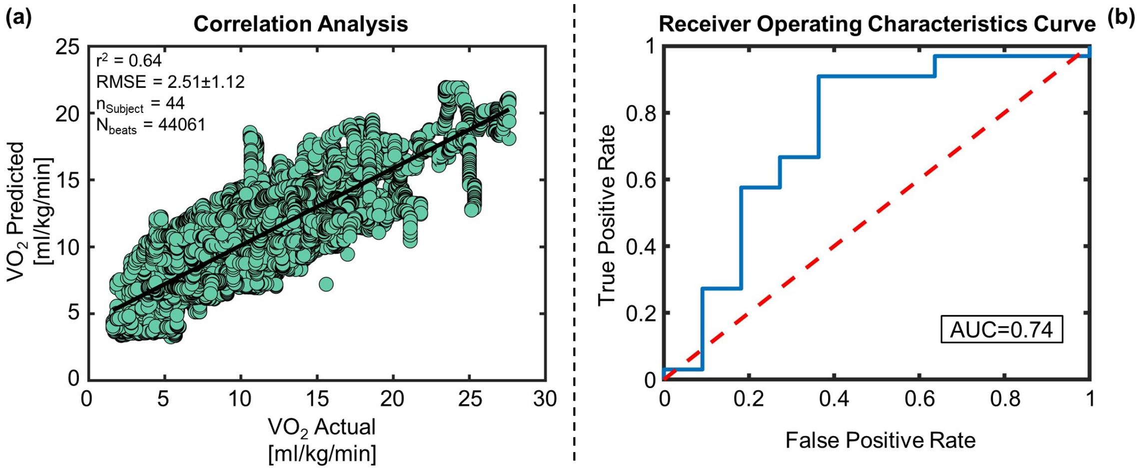

Figure 5.6: Regression and classification results on the training–testing set. (a) Correlation analysis between VO_2 predicted vs VO_2 actual for the training and testing set. (b) The blue curve is showing the receiver operating characteristic (ROC) curve for the support vector machine (SVM) classifier with a radial basis function kernel for the training and testing set. The red line is the ROC curve for classification based on random chance. The area under the blue ROC curve (AUC) is 0.74.

with 0.25 using HR only in the validation set ($P < .05$). The corresponding RMSE values were 2.55±1.16 (SCG) vs 3.58±1.54 $\mathrm{mL \cdot kg^{-1} \cdot min^{-1}}$ (HR) for the training–testing set and 2.28±1.04 (SCG) vs 3.66±1.74 $mL \cdot kg^{-1} \cdot min^{-1}$ (HR) for the validation set.

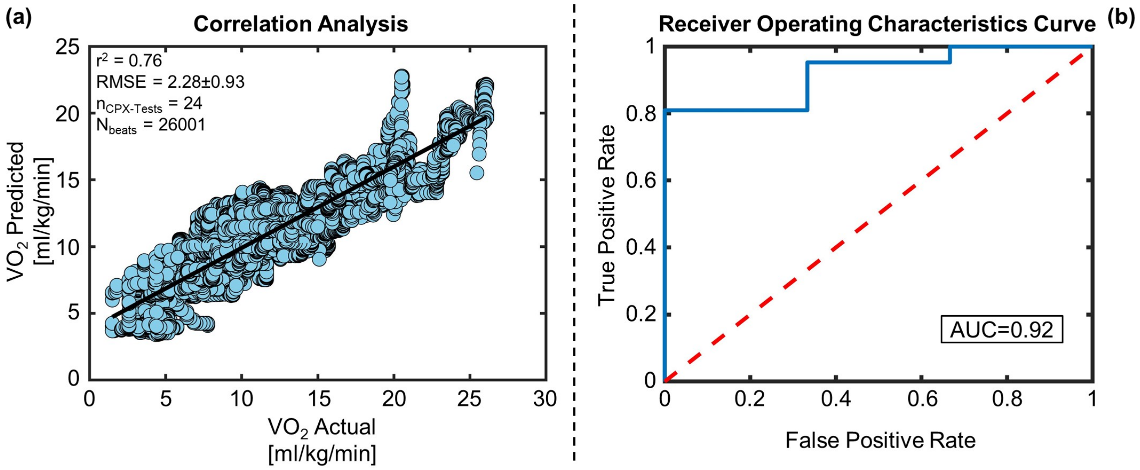

Figure 5.7: Regression and classification results on the validation set. (a) Correlation analysis between VO_2 predicted vs VO_2 actual for the validation set. (b) The blue curve is showing the ROC curve for the SVM classifier with radial basis function kernel for the validation set. The red line is the ROC curve for classification based on random chance. The AUC of the blue ROC curve is 0.92.

5.5.2 Classification

Table 5.4 and Table 5.5 show the classification results using the support vector machine with a radial basis function kernel for the training–testing and validation sets, respectively. Accuracy, sensitivity, and specificity obtained for the training–testing set were 0.84, 0.91, and 0.64, respectively, whereas for the validation set, they were 0.83, 0.86, and 0.67 respectively. Fig 5.6 (b) and Fig 5.7 (b) show the receiver operating characteristics curve of the classifier with an area under the curve of 0.74 and 0.92 for the training–testing and validation sets, respectively.

5.5.3 Peak VO_2 Estimation

Fig 5.8 shows the correlation analysis and Bland–Altman analysis between measured and estimated peak VO_2 values using SCG and ECG features for all 68 CPX instances, with a percentage error of 20.74% and an R^2 of 0.5.

Table 5.4: Confusion Matrix for Classification on the Training-Testing Set

n=44	Predicted Stage C	Predicted Stage D	
Actual Stage C	30 (TP)	3 (FN)	33
Actual Stage D	4 (FP)	7 (TN)	11
	34	10	

TP = True Positive, FN = False Negative, FP = False Positive, TN= True Negative

Accuracy = 0.84, Sensitivity = 0.91, Specificity = 0.64, Positive predictive value = 0.88 and Negative predictive value = 0.7

Table 5.5: Confusion Matrix for Classification on the Validation Set

n=24	Predicted Stage C	Predicted Stage D	
Actual Stage C	18 (TP)	3 (FN)	21
Actual Stage D	1 (FP)	2 (TN)	3
	19	5	

Accuracy = 0.83, Sensitivity = 0.86, Specificity = 0.67, Positive predictive value = 0.95 and Negative predictive value = 0.4

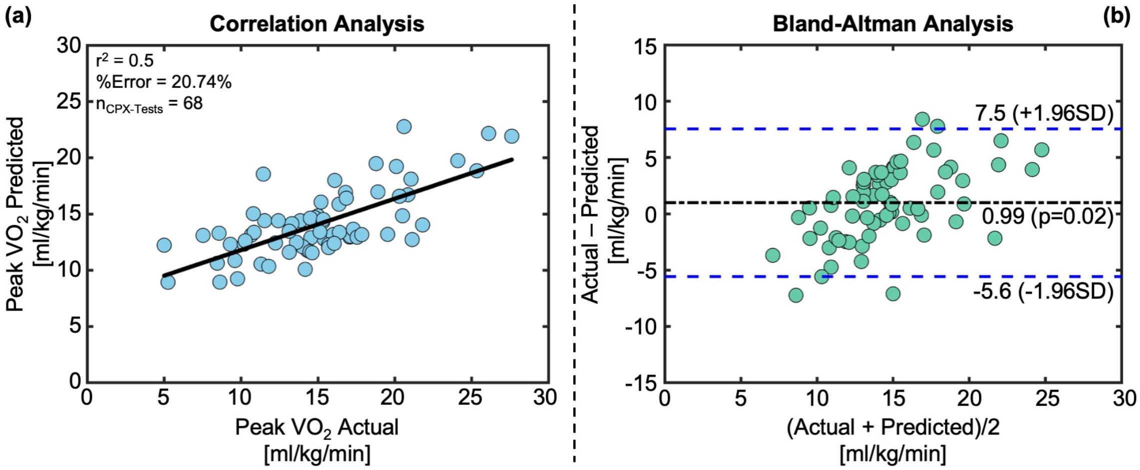

Figure 5.8: Results of peak VO_2 estimation. (a) Correlation analysis and (b) Bland–Altman analysis between predicted peak VO_2 vs actual peak VO_2 for all 68 CPX instances used in the study.

5.5.4 Peak HR-Based Regression and Classification

The correlation analysis between the peak VO_2 and the peak HR resulted in an R^2 of 0.23 for all 68 CPX instances. In contrast, estimation of the peak VO_2 using the peak HR using the same regression model and LOSO cross-validation approach used with SCG features resulted in an R^2 of 0.19 between the measured and estimated peak VO_2 values for all 68

CPX instances. The Bland–Altman confidence interval was calculated to be 17.1 mL · kg^{-1} · min^{-1} in this case. In the case of classifying the patients based on peak HR alone into stage C and stage D HF, the resultant area under the curve values for the receiver operating characteristics curve were 0.59 for the training–testing set and 0.54 for the validation set.

5.5.5 Discussion

With this proof-of-concept study, we have shown the potential of a small, lightweight, wearable patch capable of measuring SCG and ECG to estimate beat-by-beat VO_2 estimation throughout a standard CPX procedure. Our results have shown that features from the wearable patch may capture the changes in cardiopulmonary demand during exercise and may be used to differentiate between stage C and stage D HFrEF. These promising initial results provide a foundation for determining cardiopulmonary variables and the clinical status of patients with HF in their daily life and activities using wearable sensors. With further research, this approach could enable remote monitoring of these patients outside clinical settings.

An important finding in this work was that the features from the SCG signal were more salient in estimating VO_2 as compared with the ECG signal. Many Holter-type patches are currently available for ECG measurement and have been used in studies for monitoring patients with HF [41, 42]. Additionally, smartwatches are commercially available and can measure HR and possibly HR variability (provided there is minimal motion artifact). Although such commercially available tools are convenient and readily applicable to studies in patients with HF, the results from this article demonstrate that HR-based features may not provide sufficient value in assessing cardiopulmonary health in patients with HF during exercise. Rather, approaches using a combination of ECG- and SCG-based sensing are needed such that VO_2 and a patient's clinical status can be accurately determined during exercise. This result is consistent with our prior work [23], where changes in the SCG signal in response to a 6-minute walk test were found to be more salient in assessing clinical state for patients with HF than ECG or HR features alone.

Another important, and perhaps surprising, finding in this work is that the signal quality of the SCG signals measured during treadmill exercise in patients with low signal levels overall (patients with HF) was sufficiently high to enable accurate estimation of VO_2. The 2 main factors allowing such high signal quality to be obtained during exercise from a signal that has typically been limited to low motion/vibration environments only were the following: (1) the improved wearable patch we have developed that was used in this work employs the lowest noise microelectromechanical system accelerometer available, with a noise floor that is 2.5 times lower than any other microelectromechanical system accelerometer used in prior studies to the best of our knowledge; and (2) the direct coupling of the patch to the chest wall at the sternum with a triangular configuration of ECG electrodes provides a rigid and robust mechanical interface to the body from which SCG signals can be reliably recorded, even in the presence of motion artifacts. Thus, the results of this work may form a foundation upon which future efforts focused on assessing the mechanical aspects of left ventricular function during movement can be designed and realized.

From the result with peak VO_2 estimation, it is apparent that the model underestimated and overestimated peak VO_2 for very high and low values of measured peak VO_2, respectively. This limitation is well-known in machine learning-based models, because it will try to produce results close to the overall mean of the distribution rather than extreme values. Increasing the number of patients with a broader spectrum of exercise capabilities may decrease the estimation accuracy for the extreme peak VO_2 values in future studies. Also, a point to note here is that the regression model presented here was trained to learn the underlying relationship of SCG and ECG features with beat-by-beat VO_2, not only peak VO_2. Maximal effort covers only a small portion of the CPX protocol. This can be attributed to the comparatively lower performance of peak VO_2 estimation in our analysis compared with the estimation of the beat-by-beat estimation of VO_2.

Although the measurement of VO_2 values at less than peak may not currently be clinically relevant, one can imagine that with the capability of estimating VO_2 accurately for submaximal exercise tasks, such as walking upstairs or outdoors, the ability to assess patients with HF outside of clinical settings may be enhanced. Thus, in future clinical care scenarios where digital data collection methodologies are being leveraged, the measurement of VO_2 in submaximal tasks could potentially become an important and clinically relevant capability.

Comparing the results of peak VO_2 estimation using our method with peak HR-based method demonstrates that augmenting HR with cardiomechanical features may result in a higher correlation coefficient and smaller confidence interval for estimating peak VO_2. The SCG signal features resulted in a more robust classification performance for separating patients with stage C and D HF as well. Future work should focus on improving the estimation accuracy of peak VO_2 from wearable SCG and ECG signals.

The peak VO_2 was used along with the VE/VCO_2 ratio to determine the severity of HF (stage C and D) in these patients. In our regression analysis, the algorithm was trained to learn the underlying features of the SCG and ECG signals to estimate instantaneous VO_2 throughout the CPX protocol, whereas the classification algorithm was trained to learn the underlying features of the SCG and ECG signals to determine the severity (stage C vs stage D) of HF for these patients. The regression model can be used to estimate VO_2 during submaximal exercise levels as well as maximal effort, whereas classification tasks can give 1 label to the whole CPX test. These preliminary findings, however, need verification in a larger patient population with a variety of exercise levels. Because peak VO_2 played a key role in determining the true class of the patients, there can be some common SCG and ECG features that were used by both regression and classification models. Future work should examine both SCG and ECG features from both maximal and submaximal exercise to relate to the severity of HF and investigate the underlying physiological relationship between them.

It should also be noted that, although the regression and classification approaches used in this work are “black box,” as is the case for any machine learning technique, the relative importance of SCG frequency domain features vs. ECG-HR features does provide some insight into possible physiologic mechanisms behind the relationship between SCG signals and VO_2. Specifically, the changes in the frequency domain characteristics of the signals might suggest the presence of nonlinearity (i.e., harmonics) in the vibrations of the chest in response to the heartbeat at higher levels of exercise and VO_2. Another potential mechanistic link could be in the relationship between some frequencies of the SCG signal and stroke volume, which is an important factor constituting VO_2. Nevertheless, these mechanistic links are conjecture at this point and should be investigated in the future using studies with direct hemodynamic measurements (e.g., right heart catheterization) taken simultaneously with SCG signals to characterize the origin and characteristics of the signal in the context of left ventricular function and health.

This study also has several limitations that should be noted. Our dataset had only 21% patients with stage D HF (25% in the training–testing set and 13% in the validation set), resulting in higher peak VO_2 for patients with stage D HF. For a few cases of patients with stage C HF with a very high peak VO_2compared with the rest of the population, our model underestimated their VO_2 and corresponding peak VO_2 estimation. In future studies, we will increase the number of patients and incorporate patients with a broader spectrum of exercise capabilities, which may decrease the estimation error for these extreme cases. Similarly, our classification model classified 30 of 33 stage C CPX instances accurately, whereas 7 of 11 stage D CPX instances were accurately classified in the training–testing set. For the validation set, it classified 18 of 21 stage C CPX instances accurately, whereas 2 of 3 stage D CPX instances were accurately classified. The comparatively poor performance in the classification of patients with stage D HF can be associated with a smaller number of patients with stage D HF (n=14) in our dataset, the shorter duration of exercise compared with patients with stage C HF, and greater pathophysiologic differences among patients owing to various HF-related diseases. Increasing the number of patients with stage D HF in future studies should increase the classification accuracy for patients with stage D HF as well.

This preliminary study demonstrated the potential of using advanced machine learning algorithms to estimate continuous VO_2 throughout the CPX procedure and clinical status of patients with HF, both in a training–testing set and a separate validation set. Results in the validation set were comparatively better than the training–testing set. One reason can be that our validation set had fewer patients with stage D HF by chance compared with the training–testing set, and our model performed well for the patients with stage C HF because it has more patients with stage C HF to learn from in the training phase. Incorporating more patients with stage D HF in future studies should verify these initial findings in a large set of population pool.

In this work, we have only estimated VO_2. Future work should focus on estimating other gas exchange variables (e.g., VCO_2, VE, and tidal volume) from the CPX and to investigate the underlying mechanisms. Additionally, we have collected data only from patients with HFrEF. Future studies can assess the efficacy of this sensor in patients with HF with preserved ejection fraction. In addition, these tests were performed in a controlled clinical setting with trained professionals. The data from home or an unsupervised setting may be of lower quality compared with the data obtained here. Future studies can elucidate whether wearable SCG and ECG parameters measured during normal activities of daily living can be predictive of the parameters measured during extensive CPX.

5.6 Results and Discussion from Healthy Subject Study

5.6.1 Comparison of Different Feature Sets of SCG with ECG

Table. 5.6 shows the RMSE in ml/kg/min and R^2 values for different combinations of feature sets extracted from the wearable signals. Statistically significant differences existed in these results, according to the Friedman test ($p<0.05$). We performed Wilcoxon signed-rank tests on the different feature sets to investigate the significance of their differing accuracy values. All the feature sets described in this table included an AP signal feature (except HR-based linear regression model) in addition to the features explicitly stated.

Table 5.6: RMSE (*ml/kg/min*) and R^2 for VO_2 estimation from different feature sets of SCG (Amplitude, *Ampl*, Frequency, *Freq* and Time, *Time*) and ECG using XGBoost, and HR using linear regression model

	Treadmill Protocol		Outside Walking Protocol	
Feature Set	RMSE	R^2	RMSE	R^2
Ampl	4.06±1.06	0.76	4.8±1.53	0.52
Freq	**3.68±0.98**	0.77	4.85±1.31	0.57
Time	5.42±1.39	0.45	5.13±1.18	0.45
ECG	7.48±1.83	0.17	5.81±1.07	0.4
Ampl+ECG	4.24±1.18	0.72	4.46±1.56	0.58
Freq+ECG	3.99±1.28	0.71	**4.30±1.47**	**0.64**
Time+ECG	5.07±1.79	0.5	4.89±1.66	0.47
Ampl+Freq	3.78±0.98	**0.78**	4.79±1.53	0.54
Ampl+Time	4.04±1.27	0.68	4.93±1.62	0.47
Freq+Time	3.9±1.33	0.67	4.92±1.41	0.48
Ampl+Freq+ECG	3.98±1.27	0.75	4.52±1.52	0.59
Ampl+Time+ECG	4.27±1.54	0.64	4.81±1.67	0.48
Freq+Time+ECG	4.27±1.61	0.61	4.69±1.65	0.51
Ampl+Freq+Time	3.87±1.18	0.73	4.95±1.57	0.47
Ampl+Freq+Time+ECG	4.12±1.4	0.68	4.75±1.66	0.5
HR[a]	6.31±1.72	0.44	5.94±1.76	0.35

[a] A simple linear regression model was used for HR only. For other feature sets, XGBoost regression model was used to generate the reported results.

As shown in table 5.6, of the single SCG feature sets, frequency domain features achieved the lowest RMSE and highest R^2 for the treadmill protocol. Amplitude features were slightly worse ($p>.05$), and time-domain features performed the poorest ($p<.05$ compared to both frequency and amplitude). For the outdoor protocol, frequency features achieved the best R^2 and had an RMSE only slightly above ($p>.05$) that of amplitude features (with a narrower confidence interval). Time-domain features once again performed

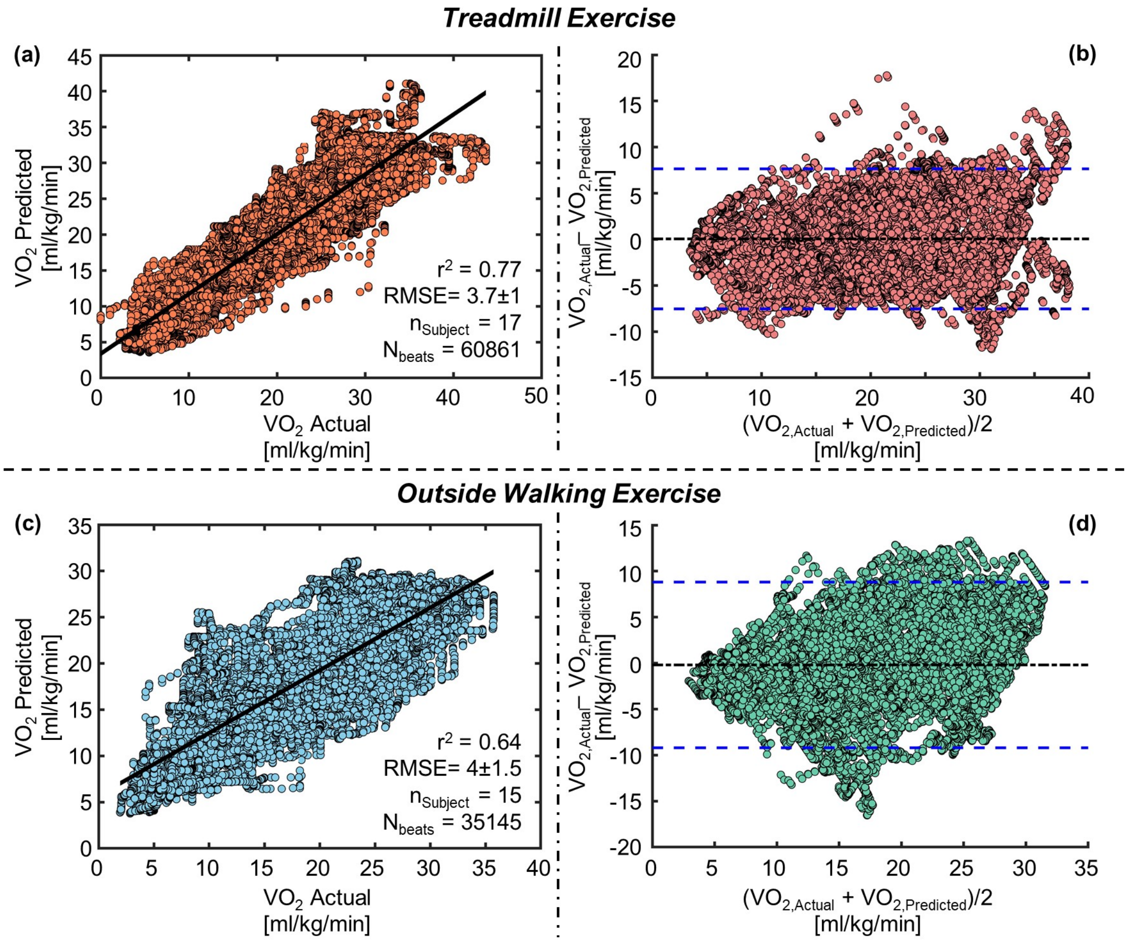

Figure 5.9: (a) Correlation analysis for VO_2 predicted vs VO_2 actual (b) Bland-Altman analysis for VO_2 predicted and VO_2 actual for treadmill exercise. (c) Correlation analysis for VO_2 predicted vs VO_2 actual (d) Bland-Altman analysis for VO_2 predicted and VO_2 actual for outside walking exercise. In the Bland-Altman plots, the solid black line indicates the mean while the blue dashed lines indicate mean ± 1.96 x standard deviation.

the worst, though not significant ($p > .05$). From these results it appears that frequency domain features provided the most salient information for estimating VO_2 from SCG in both settings.

Better performance of frequency domain features in the estimation of VO_2 is understandable as exercise leads to substantial changes in the shape and timing of waveforms. For example, the shortening of isovolumetric contraction time associated with increased sympathetic tone compresses the SCG waveform in time and thus increases high-frequency components [77]. VO_2 relates to Stroke Volume [120], which has been shown to have a relation with the amplitude features of the SCG signal [39]. This result is consistent with [121, 23], where researchers have used frequency-domain features of the SCG signal to assess clinical state for patients with HF. When comparing the frequency and amplitude features, frequency features performed slightly ($p>0.05$) better. Our results show that exercise-induced changes of VO_2 change not only the amplitude of the SCG signals but also the signal power at different frequency bands. Frequency domain features captured these changes better than amplitude features.

ECG features alone performed worse than all three SCG features alone in both protocols ($p<0.05$ compared to all three feature sets of SCG for the treadmill protocol and $p<0.05$ compared to amplitude and frequency feature sets of SCG for the outside walking protocol), using XGBoost regression algorithm. As other studies have demonstrated high linear correlations between HR and VO_2 [122, 123, 115, 124], the comparatively poor performance of ECG features (instantaneous HR and R-to-R interval) in our approach is likely attributable to the overly-complex nature of an XGBoost regression model and/or the addition of the R-to-R interval feature. To compare our results with the common HR-based approach, we also fit a simple linear regression model with HR only to estimate instantaneous VO_2 using the same LOSO cross-validation approach, which achieved an RMSE of 6.31 ± 1.72 and R^2 of 0.44 for the treadmill protocol and an RMSE of 5.94 ± 1.76 and R^2 of 0.35 for the outside walking protocol. Still, these results are significantly poorer ($p<0.05$) compared to the amplitude and frequency domain features of SCG. Separate from the HR-based simple linear regression model with LOSO cross-validation, we also performed a simple correlation analysis between instantaneous HR and VO_2 across all subjects, which resulted in an overall R^2 of 0.49 and 0.42 for the treadmill and outside walking protocol, respectively. A similar analysis on each subject individually resulted in a higher R^2 of 0.73 ± 0.11 and 0.71 ± 0.16 for the treadmill and outside walking protocol, respectively. The lower value of the global R^2 compared to the subject-wise R^2 is in agreement with existing literature [115, 124]. For this reason, researchers often use %VO_2-max and %HR-max when attempting to show population-level relationships between VO_2 and HR rather than their raw values directly [115, 124, 125, 126, 127]. Overall, these results show the benefit of incorporating cardio-mechanical information from SCG into a complex machine learning algorithm for the development of a global regression model to estimate instantaneous VO_2 compared to simple linear models involving only HR-based information.

When combining different feature sets of SCG with ECG in XGBoost regressors, we achieved our best results (i.e., lowest RMSE and highest R^2) on the treadmill protocol using amplitude and frequency features of SCG (RMSE of 3.78 ± 0.98 ml/kg/min and R^2 of 0.78), which is significantly lower ($p<0.05$) than amplitude features alone. Still, the lowest RMSE for the treadmill protocol was obtained using frequency-domain features alone (RMSE of 3.68 ± 0.98 ml/kg/min with frequency-domain features alone vs. 3.78 ± 0.98 with amplitude and frequency domain features together, $p>0.05$). For the outdoor protocol, we obtained our best results using frequency features of SCG and ECG features (RMSE of 4.30 ± 1.47 ml/kg/min and R^2 of 0.64). These results were significantly better ($p<0.05$) than those from frequency, amplitude, time, and ECG features alone. Best results in RMSE and R^2 values for each protocol are shown in bold in Table 5.6. Fig. 5.9 provides a correlation analysis and Bland-Altman analysis of actual VO_2 values and estimated VO_2 values, using the feature set with the lowest RMSE for each protocol. It is apparent that regression models can generally estimate instantaneous VO_2 well on a heartbeat by heartbeat basis.

Fig. 5.10 shows examples of best and worst estimations of VO_2 compared to actual VO_2 for both protocols. The same model used in Fig. 5.9 generated the VO_2 estimations here. Even when achieving the worst results in both protocols, as shown in Fig. 5.10 (b) and (d), the algorithm still tracks relative changes well despite overestimating overall VO_2 values. Hence, we see a consistent offset between actual and predicted values in both cases.

From Table. 5.6 in the case of the treadmill protocol, adding ECG features independently to both the amplitude feature set and the frequency feature set increased the error in both cases. This is as expected because the performance of ECG features was the worst

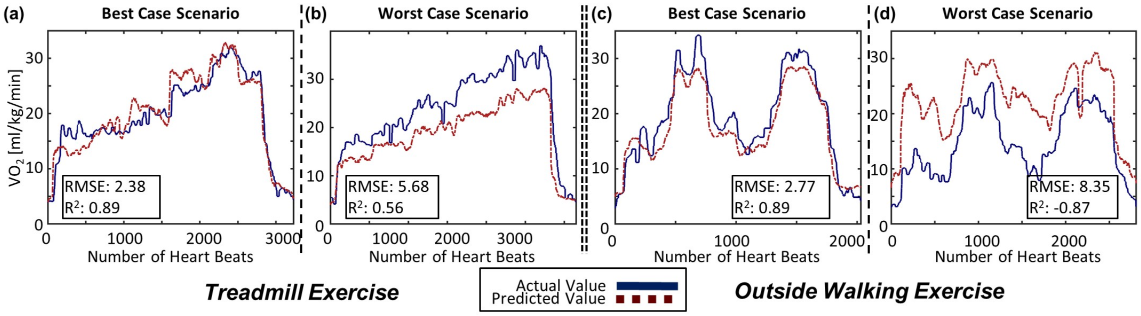

Figure 5.10: Example of subject-wise VO_2 prediction for both exercise tasks: (a) Best case scenario and (b) worst case scenario for treadmill exercise. (c) Best case scenario and (d) worst case scenario for outside walking exercise.

among all the feature sets for the treadmill protocol. For the outside walking protocol, adding ECG features reduced the RMSE for these same two feature sets ($p<0.05$). For better VO_2 estimation, the selection of feature sets for a global model should incorporate domain knowledge of cardio-electromechanical responses to ranges of exercise and activity.

Overall from Table 5.6, the estimation results were better for the treadmill protocol than for the outside walking protocol. This is expected as the treadmill protocol took place indoors with standardized speeds and conditions, whereas the outside walking protocol was completed at the subject's pace with variable atmospheric conditions depending on the day. Future studies should examine wider varieties of exercise with subjects of broader age range and health status to apply this methodology in estimating instantaneous VO_2 throughout daily activities.

5.7 Conclusions

We have demonstrated that a wearable chest patch-based sensor capable of recording ECG and SCG may be used to estimate VO_2 from CPX for patients with HF using a global regression model and may facilitate the determination of the clinical state of the patient. We have also demonstrated that the patch-based sensor is capable of estimating VO_2 in uncontrolled daily life activities with healthy individuals. We thus demonstrated that wearable sensors can potentially be used to monitor cardiopulmonary health and to stratify disease risk for patients with HF both in an inpatient and in an outpatient management system. The approach described in this work may thus provide the capability to perform longitudinal CPX testing for patients with HF in clinical and hospital settings such that treatment and management can be titrated and personalized based on physiologic state. Because CPX testing has been established as a valuable technique in assessing patient state for HF, broadening the ability to perform such testing in longitudinal patient management may improve the quality of care and life for patients with HF. Future studies should verify these preliminary findings in a larger patient population with a wider spectrum of exercises, in both a clinical environment and normal daily living activities.

CHAPTER 6

TRACKING CHANGES IN PULMONARY CONGESTION WITH SEISMOCARDIOGRAM DURING RIGHT HEART CATHETERIZATION WITH VASODILATOR CHALLENGE IN PATIENTS WITH HEART FAILURE

6.1 Overview

Tracking changes in pulmonary congestion and the consequent proactive readjustment of treatment plans have shown efficacy in reducing rehospitalization for patients with HF. However, the cost-prohibitive nature of these sensing systems precludes their usage in the large patient population affected by HF. In this study, we estimated the changes in pulmonary artery mean pressure (PAMP) and pulmonary capillary wedge mean pressure (PCWMP) due to vasodilator infusion during right heart catheterization, using changes in wearable SCG. We have collected data from 19 subjects with HF, and using a population regression model estimated the changes in PAMP and PCWMP with the changes in simultaneously recorded SCG. The leave-one-subject-out cross-validated result shows good estimation accuracies for both: an RMSE of 2.6 mmHg and R^2 of 0.77 for estimating changes in PAMP, and an RMSE of 2.2 mmHg and R^2 of 0.88 for estimating changes in PCWMP. The result of this work shows that changes in SCG can be used to track changes in pulmonary congestion due to vasodilator infusion.

6.2 Introduction

The increased filling pressure of the heart is an early indicator of the onset of worsening HF [25]. Continuous monitoring of PA pressure using an implantable sensor (CardioMEMS) to track the increased filling pressure of the heart and adjustments of care (i.e., titration of medications, early follow-up clinic visits, etc.) have shown efficacy in reducing readmission for patients with HF [19, 128, 129]. CardioMEMS (CardioMEMS HF System, Abbott, Chicago, IL) is a microelectromechanical system (MEMS) based pressure sensor that is implanted in the pulmonary artery and which sends the pulmonary artery pressure once per day to the clinicians [24] and the clinicians can change the course of the treatment (by titrating medication) based on the pulmonary congestion to keep the pulmonary artery pressure within a recommended limit [19]. This proactive adjustment of care has been shown to reduce the HF-related readmission by 33%.

Another recent technologies from Sensible medical (Netanya, Israel), remote dielectric sensing (ReDS), also tracks the pulmonary congestion (lung fluid content) via measuring the dielectric properties of the thorax (with the sensor placed on the right mid- thorax) non-invasively and has shown efficacy in reducing HF-related rehospitalization by 87% and 79% compared to pre- and post ReDS guided therapy in a clinical study consists of 50 patients with HF[22]. Both of these technologies have shown the importance of tracking pulmonary congestion (a biomarker for tracking the filling pressure of the heart) as an early indicator of the worsening HF condition and the efficacy of hemodynamically-guided HF management system to reduce hospitalization. However, costs related to both the device ($>$ \$25,000 for CardioMEMS and \$48,000 for ReDS) make them financially non-accessible for the large patient population affected with HF in the US, which is roughly 6.2 Million Americans [130]. For that reason, a low-cost alternative that can track changes in pulmonary congestion has the potential to help millions of people affected with HF not only in the US but also in the whole world.

With the advent of MEMS-based sensors and digital health technologies, various wearable monitoring systems have been explored by the clinicians and researchers to monitor cardiovascular health both in healthy individuals and patients with HF. One such methodology is Seismocardiogram (SCG), the local vibration of the chest wall due to the cardiac cycle, which has shown to track cardiac contractility with exercise and physiological perturbation [76, 131, 95]. Recent studies have shown that SCG can be used to classify patients with decompensated HF [23, 121]. Based on these results on SCG in tracking hemodynamics for both healthy individuals and patients with HF, we hypothesized that the changes in pulmonary artery pressure (PAP) and pulmonary capillary wedge pressure (PCWP) could be tracked with changes in SCG signal.

In the current work, we recorded SCG and ECG signals from patients with HF using a previously validated custom-built wearable patch during the right heart catheterization (RHC) [132] procedure, which is a gold standard clinical procedure to measure pulmonary congestion via measuring pulmonary artery pressure (PAP) and pulmonary capillary wedge pressure (PCWP). During the RHC procedure, the PAP and PCWP were modulated via infusing systemic vasodilator, and changes in the mean pressure values were estimated via tracking the changes in simultaneously recorded SCG signals. We have analyzed various portions of the SCG signals to understand the important segments that are providing more relevant information regarding changes in PAP and PCWP.

6.3 Methods

6.3.1 Experimental Protocol

The study was conducted under a protocol reviewed and approved by the University of California, San Francisco, and the Georgia Institute of Technology Institutional Review Boards. All patients provided written consent before the procedure. We have conducted the RHC procedures on a total of 19 patients with HF (14 with HFrEF and 5 with HFpEF, four female, age: 55±14, weight: 92±18 kg, height: 175±10 cm, ejection fraction [EF]: 32±19). All of the patients were recruited from the Catheterization laboratory at the University of California, San Francisco.

Fig 6.1 (a) illustrates the experimental setup and placement of different sensors on each patient. Before starting the RHC procedure, the custom-built wearable device was placed just below the suprasternal notch, and the RHC computer was time-synchronized with the wearable patch.

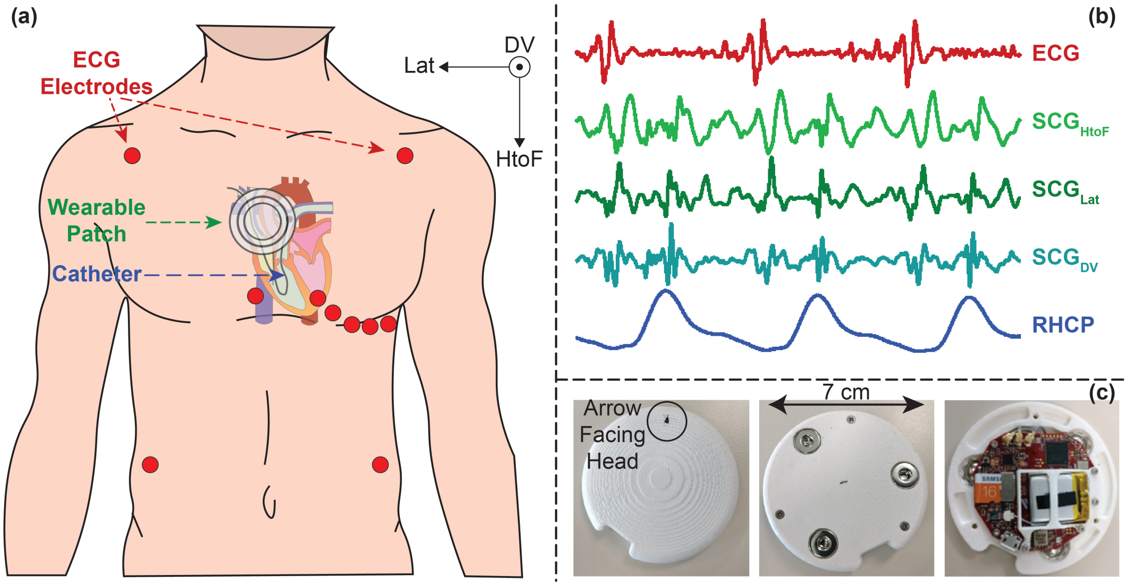

Figure 6.1: (a) Experimental setup with a wearable patch placed on a subject undergoing right heart catheterization (RHC) procedure, with axes (on the upper-right) showing the axes of the seismocardiogram (SCG) signal. (b) Representative cardiogenic signals: electrocardiogram (ECG), triaxial SCG (head-to-foot [HtoF], lateral [Lat], and dorsoventral [DV]), and RHC pressure (RHCP) signal. (c) Wearable patch top, bottom, and inside view with the bottom view showing the snaps for ECG electrodes.

For beginning the RHC procedure, a local anesthetic agent was administered subcutaneously at the access site. To access the venous, an 18-gauge needle was inserted in the femoral/jugular site, and once the venous access was obtained, an appropriately sized sheath is placed in the vein and secured. A pulmonary artery swan-ganz catheter [133] was advanced through the sheath into the vein and guided to the right atrium, right ventricle, pulmonary artery, and pulmonary capillaries following standard protocol [134]. The blood pressure values at different intra-cardiac and pulmonary chambers were recorded at the end of expiration from the RHC computer. When the baseline pressure values were recorded, a systemic vasodilator (nitroprusside/nitroglycerin) was infused and the RHC pressure values were again recorded at the end of expiration. When all the pressure values were recorded, the catheter was taken out from the veins, and subjects were monitored for post-procedure recovery. The wearable ECG and SCG signals were recorded continuously throughout the

RHC procedure, and the timestamps from both the RHC and wearable system were used to extract the specific portions of the wearable signals later in the analysis, to estimate the changes in PAP and PCWP from the changes in wearable signals. Fig 6.1 (b) shows the wearable signals with corresponding PAP signal from the RHC computer during the baseline RHC recording from a representative subject.

6.3.2 Sensing Hardware

RHC pressure values were extracted by the expert RHC clinicians from the RHC Mac-Lab computer (Mac-Lab Hemodynamic Recording System, GE Healthcare, Chicago, IL, USA).

We collected the wearable ECG and triaxial SCG (axes: head-to-foot (HtoF), dorsoventral (DV), and lateral (Lat)), with the same wearable patch described in Chapter 5, as shown in Fig. 6.1(c). All the ECG and SCG signals were sampled at 1kHz.

6.3.3 Signal Procecssing and Feature Extraction

Fig. 6.2 illustrates the signal processing and feature extraction procedures used for the wearable signals and the pressure signal from the RHC computer. Both the system were time-synchronized before the procedure was started. The PA mean pressure (PAMP) and PCW mean pressure (PCWMP) values for both the baseline (BL) and during vasodilator infusion (VI) were extracted by the expert clinicians and later used to calculate the changes in PAMP (δPAMP) and changes in PCWMP (δPCWMP) using the following equations:

$$\delta PAMP = PAMP_{\text{VI}} - PAMP_{\text{BL}} \tag{6.1}$$

$$\delta PCWMP = PCWMP_{\text{VI}} - PCWMP_{\text{BL}} \tag{6.2}$$

The PCWMP_{VI} value for one subject was not recorded due to a technical issue in the Mac-Lab system. For that reason, the δPCWMP value is missing for that subject. In total, we had δPAMP values from 19 subjects and δPCWMP values from 18 subjects for this study protocol.

The synchronized timestamps were used to extract 20 seconds long wearable signals (ECG and SCG) from both BL and VI state of the protocol when the catheter was at the pulmonary artery and pulmonary capillaries. The changes in the wearable signals were analyzed with the δPAMP and δPCWMP values and later used in a population regression model with cross-validation. The details of the wearable signal processing, feature extraction, and regression model are given below.

Preprocessing and Noise Reduction

The BL and VI wearable signals were processed (filtering, removal of outliers, and ensemble averaging) separately and later used to calculate the dynamic time warping (DTW) distances between the two states. The DTW distances between different portions of the SCG signals from different axes were used in a regression algorithm to estimate δPAMP and δPCWMP with leave-one-subject-out (LOSO) cross-validation.

The raw ECG and SCG signals from the wearable patch were digitally filtered (cut-off frequencies: 0.5–40.0 Hz for the ECG and 1–40 Hz for the SCG signals) to remove out-of-band noise. We chose these cut-off frequencies to remove out-of-band noise without distorting the shape of the signals [131]. After the filtering step, we computed a fourth SCG signal representing the accelerometer magnitude ($\mathrm{SCG}_{\mathrm{Mag}}$) using the three SCG axes already obtained ($\mathrm{SCG}_{\mathrm{HtoF}}$, $\mathrm{SCG}_{\mathrm{Lat}}$, $\mathrm{SCG}_{\mathrm{DV}}$) according to the following formula:

$$SCG_{\mathrm{Mag}} = \sqrt{(SCG_{\mathrm{HtoF}}{}^2 + SCG_{\mathrm{Lat}}{}^2 + SCG_{\mathrm{DV}}{}^2)} \tag{6.3}$$

We amplitude normalized the ECG signal (in the 20-second frame) and used the Pan Tompkins method [135], [136] to detect the R-peaks of the ECG signal. We segmented the SCG signals (four axes of SCG) into individual heartbeats using the R-peaks of the ECG signal. We cropped each heartbeat to a duration of 500 ms before and after the R-peak. The

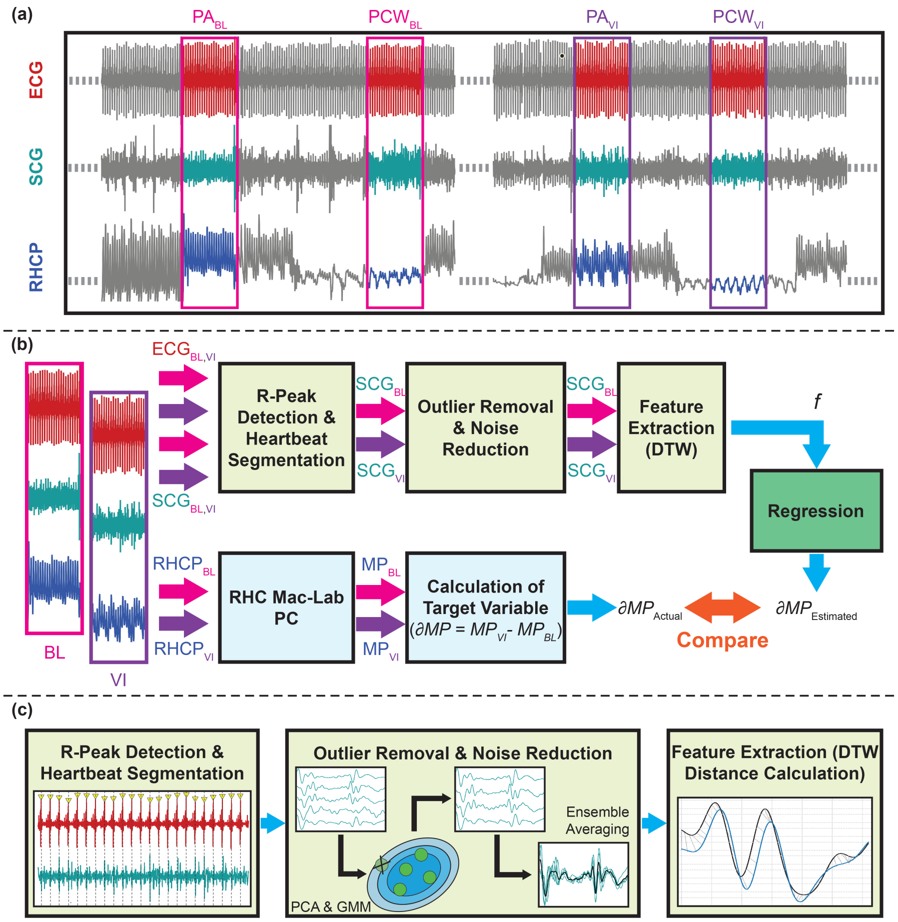

Figure 6.2: Overview of the method: (a) Wearable ECG and SCG (only showing one axis of the signal for simplicity) signals were synchronized with the RHCP signal. 20s long signals from both baseline (BL) and during vasodilator infusion (VI) were extracted when the catheter was recording pulmonary artery (PA) pressure and in pulmonary capillary wedge (PCW) pressure signals. (b) The R-peaks of the ECG signal were detected and later used to segment the corresponding SCG signals into individual heartbeats. Outlier removal and noise reduction steps were performed on the SCG heartbeats, and features were extracted to be used in the regression algorithm to estimate the changes in the RHC mean pressure (MP) values (e.g., changes in pulmonary artery mean pressure [δPAMP], and changes in pulmonary capillary wedge mean pressure [δPCWMP]). The MPBL and MPVI values were extracted from the RHC Mac-Lab computer and used to calculate the target variable (δPAMP and δPCWMP). (c) Details on the wearable signal processing: First, the R-peaks of the ECG signals were detected, and the SCG signals were segmented into individual heartbeats. Second, SCG_{BL} and SCG_{VI} heartbeats were passed through an outlier removal algorithm (using principal component analysis [PCA] and Gaussian mixture model [GMM]) and were ensemble-averaged to have two average SCG heartbeats per axis (one for BL and one for VI). Third, dynamic time warping (DTW) distances were calculated between the BL and VI heartbeats per axes and used as features (f) in the regression algorithm.

500 ms SCG frame before the R peak roughly represents the ventricular diastolic phase, and the 500 ms SCG frame after the R peak roughly represents the ventricular systolic phase of the cardiac cycle, as described in Fig. 2.3. We chose the duration of 500 ms before and after the R-peak based on our previous experience with SCG signals and generic feature extraction processes [131], as most of the relevant diastolic and systolic cardiac events of interests (e.g., rapid inflow, atrial systole, isovolumetric contraction, ventricular ejection, etc.) occur within this time frame, with respect to the corresponding R-peak of ECG. We chose a constant time window to crop the ECG and SCG signals to have a repeatable and generic feature extraction process.

Following the heartbeat segmentation of the wearable SCG signals, we removed the outliers beats from the SCG for the two distribution from the two states (BL and VI) for each axis and each portion (diastolic and systolic) of the SCG signals separately. For outlier removal from a particular distribution, we reduced the dimension of the 500 sample long SCG heartbeats (for 500 ms long frame with a 1kHz sampling frequency) into three dimensions by using principal component analysis (PCA) and taking the first three principal components (PC). This low-level representation of the SCG heartbeats was used in a Gaussian-mixture model (GMM) to determine the probability that each sample belongs to a particular distribution (BL or VI) for a particular portion and a particular axis of SCG. For a particular distribution, the points with the lowest 20% probability were detected as the outlier for the distribution. The cut-off of 20% was chosen based on the initial analysis with 10%, 20%, and 30% beats removed as outliers. As most of the power in the SCG signal stays in the systolic portion of the signal [39], it might end up dominating the outlier removal in the diastolic portion of the signal. For that reason, the outlier removal was performed separately for the diastolic and systolic portion of the SCG. The actual SCG heartbeats correspond to the outliers for the distribution were removed and resulted in two separate distribution per axis (SCG_{BL} and SCG_{VI}). The remaining heartbeats were ensemble-averaged [85] to create two ensemble-averaged heartbeats for BL and VI for a particular axis and portion, which were later used to calculate the DTW distances. The ensemble-averaging step reduced the inherent variabilities and remaining noises in the SCG heartbeats. Fig. 6.3 shows the ensemble-averaged SCG_{DV} heartbeats from the BL and VI states and corresponding PAP and PCWP heartbeats.

Dynamic Time Warping and Feature Extraction

To calculate the changes in SCG from BL to VI, we have used dynamic dime warping (DTW) and compare the DTW distances from different portions of the SCG heartbeats to the δPAMP and δPCWMP in simple correlation analyses, shown in Fig. 6.4. The DTW is a time-series analysis method to align signals and find similarities between signals [137]. We have used Euclidean distances as the DTW-based distance calculation between signals from BL and VI. The DTW distances were calculated from different portions of the SCG heartbeats: total diastole (-500ms:R-peak), early diastole (-500ms:-200ms), late diastole (-200ms:R-peak), total systole (R-peak:500ms), early systole (25-150 ms), and late systole (200-500ms), where negative time means before the R-peak and positive time means after the R-peak. Early diastole corresponds to the passive ventricular filling, late diastole corresponds to the atrial systole, early systole corresponds to isovolumetric contraction (IVC), and late systole corresponds to the ventricular ejection phase of the cardiac cycle, as depicted in Fig. 2.3. We compared the DTW distances from the different portions of SCG heartbeats with the target variable in a simple correlation analysis (shown in Fig. 6.4) and calculated the coefficients of determination (R^2) between them to analyze which segments of the SCG are more relevant to track changes in PAMP and PCWMP. Later, we used the DTW distances as the features in a regression algorithm to estimate the changes in PAMP and PCWMP.

6.3.4 Regression

Following the feature extraction and simple correlation analysis, a population level regression model with LOSO cross-validation was performed to estimate the δPAMP and δPCWMP from the DTW distances. We explored different regression algorithms for this purpose, and from our initial analysis, the Ridge regression model outperformed other regression methods. For that reason, we chose the ridge regression model for detailed analysis in this work. The Ridge regression method belongs to the class of linear regression models with l2 regularization where the loss function is the linear least-squares function, and the regularization is given by the l2-norm [138].

As we have seen in the simple correlation analysis (Fig. 6.4) between the DTW distances from different portions of the SCG heartbeats and corresponding target variables (δPAMP and δPCWMP), not all the changes from the different portions of the SCG (i.e., DTW distances) are relevant to the changes in the mean pressures (MP). For that reason, we have performed a feature selection technique using sequential forward selection (SFS) [139]. We selected the top 5 features as the estimating variables in the regression model.

We used LOSO cross-validation for *n* subjects. At each fold we trained a Ridge regressor on the selected (using SFS method) DTW distances from *n-1* subjects, leaving one subject out. We then predicted the target variables (δPAMP and δPCWMP) for the left-out subject, repeating this *n-1* more times with a different subject excluded each time. As a result, we obtained predictions for all subjects. We calculated a root mean squared error (RMSE) between the estimated target variable ($\delta\text{MP}_{\text{Pred}}$) and the ground truth target variable from the RHC computer ($\delta\text{MP}_{\text{Act}}$):

$$RMSE = \sqrt{\frac{1}{n}\sum_{i=1}^{n}(\delta MP_{\text{Pred(i)}} - \delta MP_{\text{Act(i)}})^2} \tag{6.4}$$

where *n* is the number of subjects. We also performed a simple correlation analysis and Bland-Altman analysis between the true values and the cross-validated predictions of

δMP across all subjects. We have performed the Pearson correlation analysis between the estimated and true δMP to get the statistical significance of prediction and calculated R^2 between the true and predicted values. In this work, we considered p-values below 0.05 to be statistically significant.

6.4 Results & Discussion

6.4.1 Effects of Vasodilator on RHCP and SCG

Fig. 6.3 shows the changes in PAP and PCWP signals and the changes in SCG_{DV} with vasodilator infusion. One thing to note here is that all the signals shown in the figure are synchronized with the corresponding R-peak. We can see how the overall mean of the PAP and PCWP signals are decreased with vasodilator infusion, whereas the systolic portion of the SCG_{DV} signal is right-shifted with vasodilator. With vasodilator infusion, the PAMP and PCWMP decrease as well as the preload of the heart (the filling pressure of the heart), and PEP is inversely correlated with preload [32]. For that reason, with a decrease in preload, we are observing an increase in PEP, which is as expected. The diastolic portion of the SCG signal is also changing in morphology; however, the change is not very apparent compared to the systolic portion of the SCG. From this figure, it is apparent that the changes in SCG signals (specifically in the systolic portion of the signal) with vasodilators have the potential to track the changes in PAMP and PCWMP.

6.4.2 Feature Correlation

Fig. 6.4 shows the R^2 values between the DTW distances from different portions and axes of the SCG signals with δPAMP and δPCWMP. In the case of δPAMP, the changes in SCG during the early systole (IVC period) provide the most relevant information related to changes in the PAMP, with changes in SCG_{DV} during the IVC period showing the highest R^2 of 0.8 with δPAMP. In the case of δPCWMP, the changes in the SCG during the late diastole (atrial systole) phase provided the most relevant information related to changes

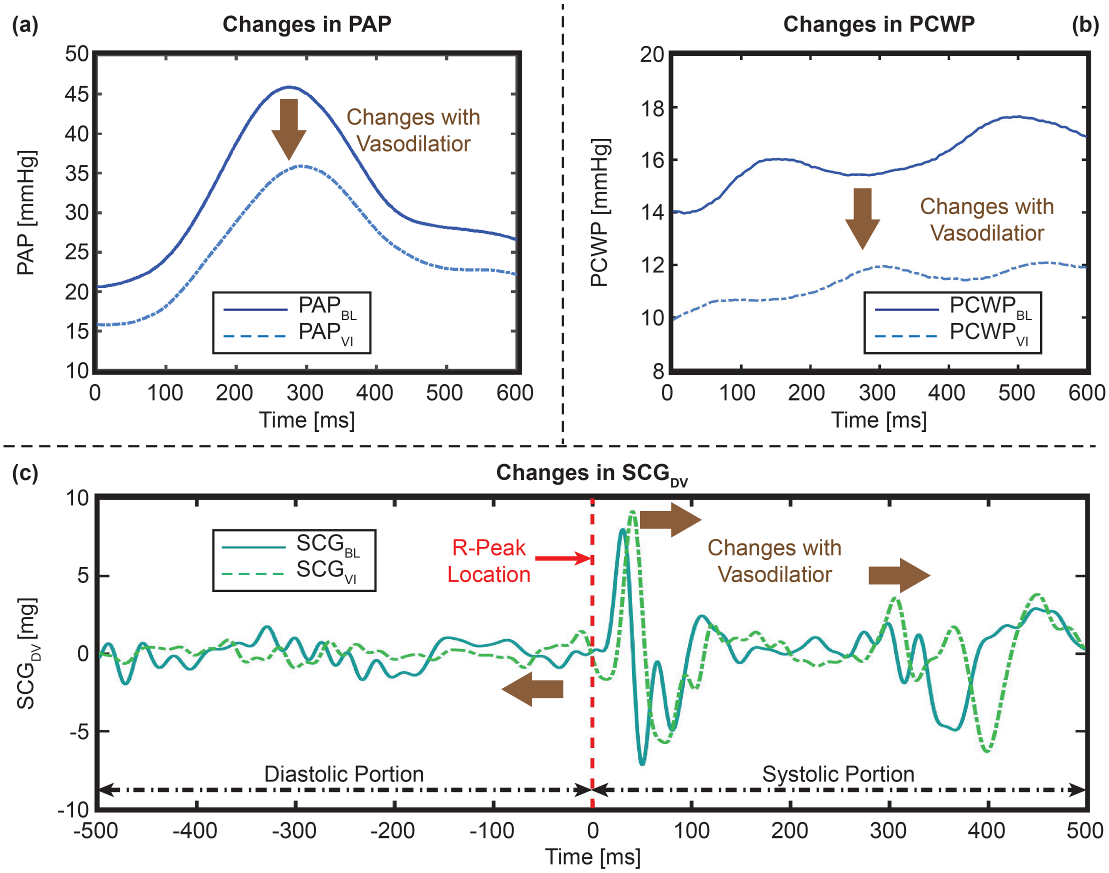

Figure 6.3: Changes in (a) pulmonary artery pressure (PAP), (b) pulmonary capillary wedge pressure (PCWP), and SCG_{DV} with the infusion of vasodilator for a representative subject, with brown arrows showing the changes in the respective signals. Time “0” indicates the location of the corresponding ECG R-peak.

in PCWMP, with changes in SCG_{Mag} during the late diastole period showing the highest R^2 of 0.86 with δPCWMP. Overall, the figure is showing that δPAMP is more related to the changes in the systolic portion (IVC more specifically) of the SCG signal, whereas δPCWMP is more related to the changes in the late ventricular diastole (i.e., atrial systole) portion of the SCG. It might be explained with physiological rationale, as the pulmonary artery is directly connected to the right ventricle, the ventricular systole (contraction) phase is dominating the changes in PAMP. On the other hand, the pulmonary capillaries are connected to the left atrium and showing more relation with atrial systole. These preliminary results should be verified with simultaneous imaging modalities, in a large population study with diversified subjects with various cardiovascular conditions.

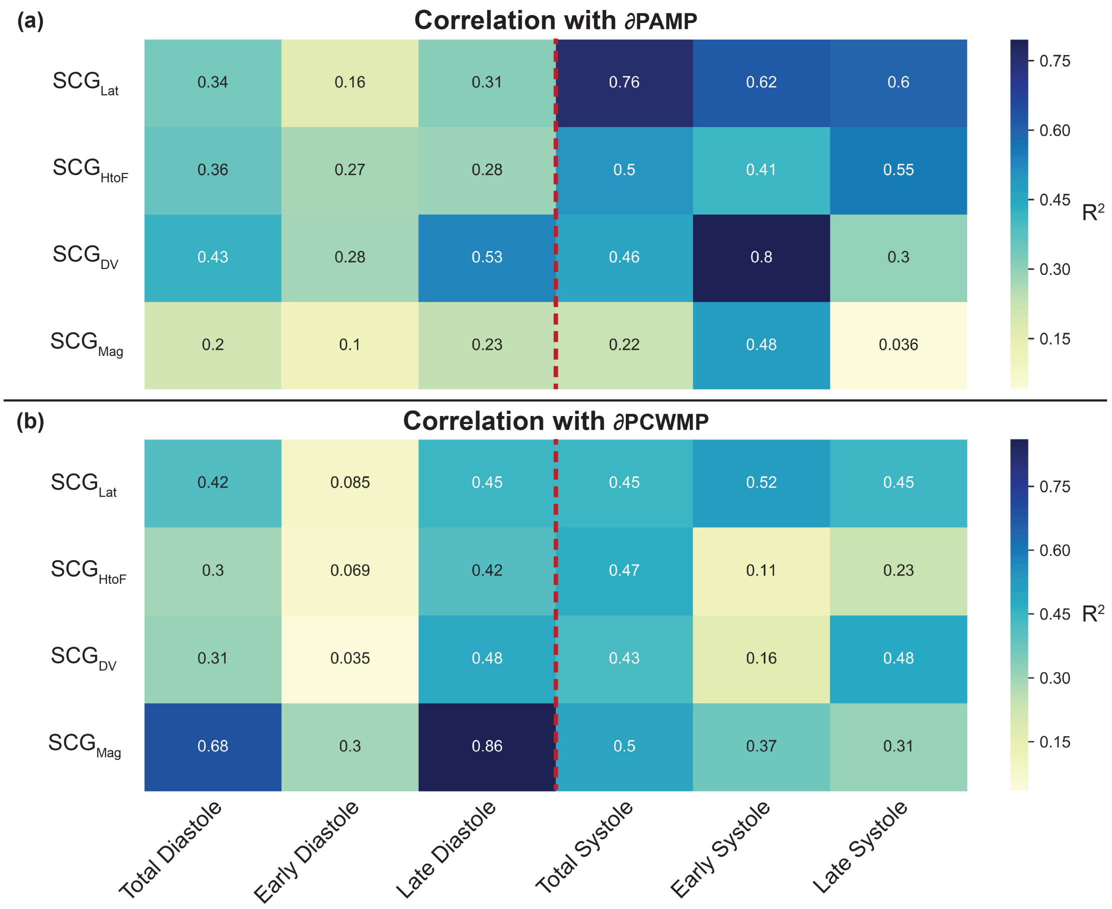

Figure 6.4: Correlation analysis of the target variable (a) δPAMP and (b) δPCWMP with different DTW distances of corresponding SCG signals, with the colorbar showing the R2 values and the red dotted line indicating the division between ventricular diastole and systole (i.e., R-peak of corresponding ECG). Total Diastole (-500ms:R-peak), early diastole (-500ms:-200 ms), late diastole (-200ms:R-peak), total systole (R-peak:500ms), early systole (25ms:150ms), and late systole (200ms:500ms).

6.4.3 Regression Estimation

Fig 6.5 shows the correlation analysis and Bland-Altman analysis between the actual (measured) and the estimated δPAMP and δPCWMP values, using the selected five DTW distances with the labels shown in Fig 6.6. The correlation shows a good estimation accuracy for both δPAMP and δPCWMP, with RMSE of 2.6 mmHg and an R^2 of 0.77 for δPAMP, and RMSE of 2.2 mmHg and an R^2 of 0.88 for δPCWMP. The Bland-Altman analysis also shows that the regression model was able to predict very high to a very low value of changes well with a 95% error of estimation within ±5.2 mmHg for δPAMP and ±4.4 mmHg for δPCWMP. The results are showing that the changes in SCG can be used to track the changes in PAMP and PCWMP. However, this is a pilot study, and the results from this initial study should be verified with a large population in a longitudinal study.

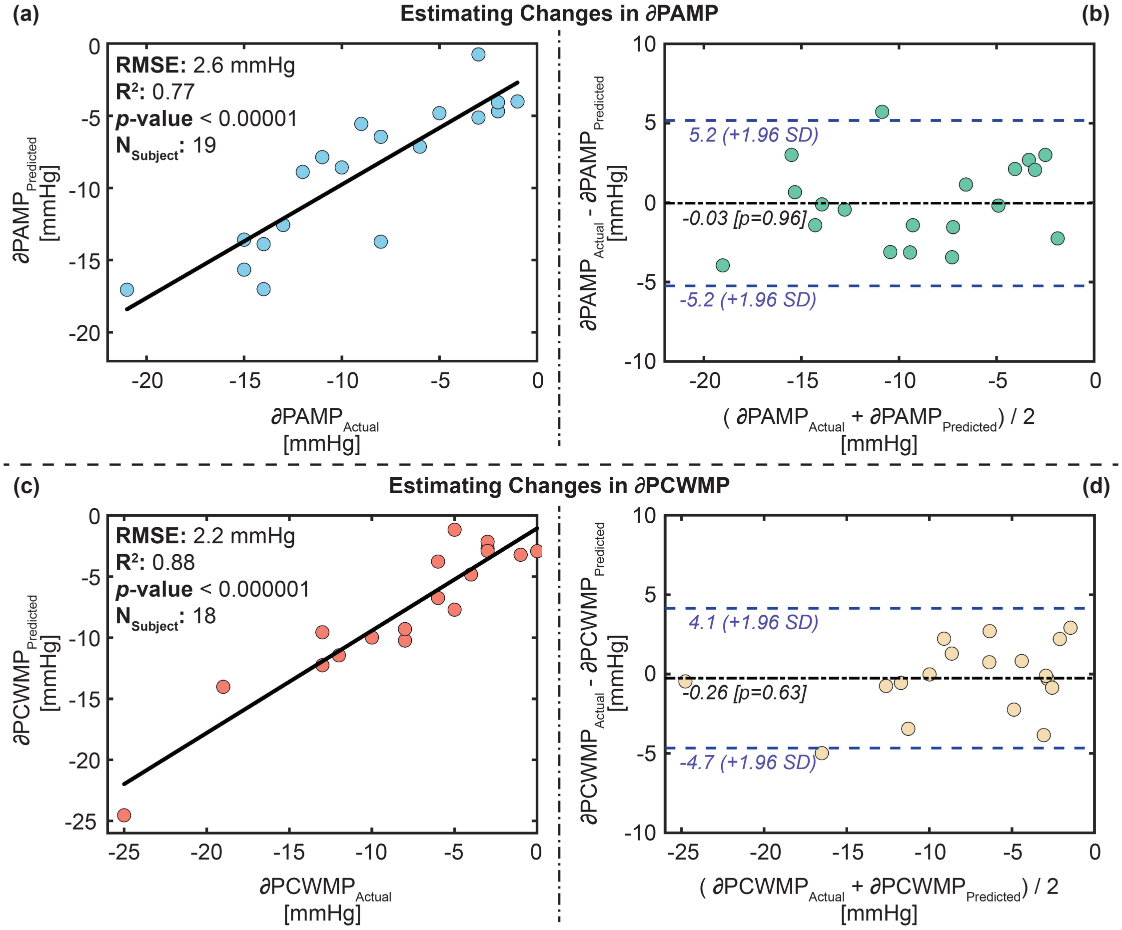

Figure 6.5: (a) Correlation analysis for δPAMP predicted vs. δPAMP actual, (b) Bland-Altman analysis for δPAMP predicted and δPAMP actual, (c) correlation analysis for δPCWMP predicted vs. δPCWMP actual, and (d) Bland-Altman analysis for δPCWMP predicted and δPCWMP actual. In the Bland-Altman plots, the black line indicates the mean, while the blue dashed lines indicate mean $\pm$ 1.96$\times$ standard deviation (SD)

6.4.4 Feature Importance

Fig. 6.6 shows the relative weights of the features in the Ridge regression for the estimation of δPAMP and δPCWMP, with the top feature related to δPAMP being the change $\mathrm{SCG}_{\mathrm{DV}}$ during the IVC period and the top feature related to δPCWMP being the change $\mathrm{SCG}_{\mathrm{Mag}}$ during the atrial systole period. Similar to the results obtained from the individual correlation analysis (in Fig. 6.4) between the target variables with the DTW distances, all the top 5 features for the δPAMP are from the systolic portion of the SCG. In the case of δPCWMP, three of the top five are from the diastolic portion of the SCG and two are from the systolic portion of the SCG. Both Fig. 6.4 and Fig. 6.6 are showing the importance of the diastolic portion of the SCG in estimating δPCWMP. Most of the SCG researches are concentrated on the systolic portion of the signal [39, 58]. Our results suggest that diastolic portion of the SCG signal also has the potential to provide relevant information regarding pulmonary congestion.

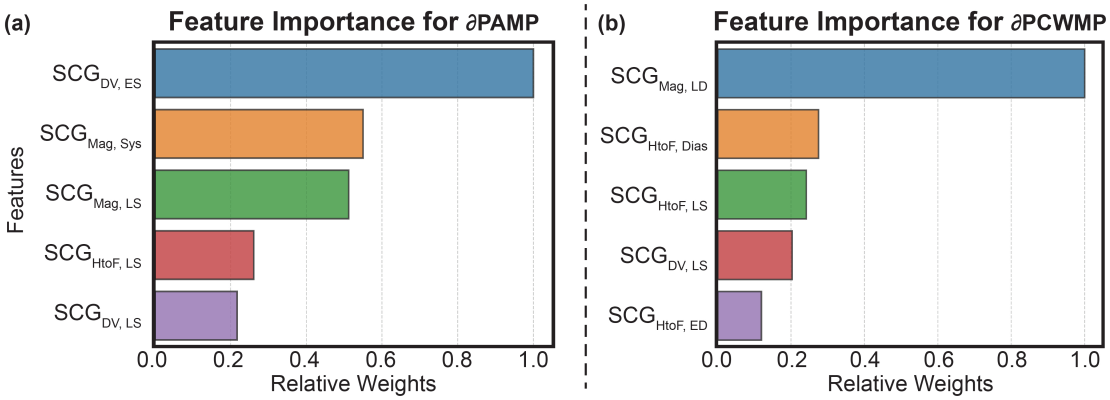

Figure 6.6: Relative feature importance ranking (i.e., relative weights) of the features in the regression algorithm for (a) δPAMP and (b) δPCWMP. Dias: Total Diastole, ED: Early Diastole, LD: Late Diastole, Sys: Systole, ES: Early Systole, and LS: Late Systole. Time-length for the segments is explained in Fig. 6.4

6.5 Conclusion and Future Work

In this work, we have estimated the changes in pulmonary artery mean pressure and pulmonary capillary wedge mean pressure in patients with HF due to vasodilator infusion with the changes in simultaneously recorded SCG signal. We have developed a global regression model for the estimation of δPAMP and δPCWMP using state-of-the-art machine learning algorithms validated with leave-one-subject-out cross-validation. We have demonstrated that tracking changes in SCG can track changes in the pulmonary congestion (the filling pressure of the heart), which has the potential to be used for remote home management for patients with HF. Overall, this work demonstrates the capability of an unobtrusive wearable patch to track pulmonary congestion. Success in this regard represents a considerable step towards the hemodynamically-guided affordable HF management for the mass population affected by HF.

Though this preliminary study has shown good promise in tracking changes in PAMP and PCWMP in patients with HF, it has multiple limitations. This preliminary study was conducted with 19 persons only, including both patients with HFrEF and HFpEF. However, the pathophysiology of the two HF subgroups may present different relationships between the changes in SCG with changes in PAMP and PCWMP. Due to the small number of subjects for this preliminary study, we could not analyze the difference. Future studies should verify the analysis of this preliminary study in a large patient population with HF, with emphasis on the difference between the HF subgroups. We have estimated the changes in PAMP and PCWMP only. Future studies should look into changes in other key variables from RHC procedure, e.g., right atrium pressure, right ventricle pressure, stroke volume, cardiac output, and cardiac index. In this study, we have considered the change in pulmonary congestion with vasodilator infusion only. Future study should include other pharmacological agents, e.g., diuretics, beta-blocker, ace-inhibitors, and verify whether changes in SCG can be used to track changes due to other pharmacological agents as well. We have collected data during the RHC procedure in a controlled clinical environment for acute changes in pulmonary congestion. To be a reliable sensor for outpatient HF management, the device and the methods need to be verified with a longitudinal remote home pulmonary congestion monitoring systems (e.g., CardioMEMS and ReDS). Future studies should also focus on how the motion artifacts and home data quality may impact estimation accuracy.

CHAPTER 7
CONCLUSIONS AND FUTURE WORK

7.1 Conclusions of the Presented Work

Recent work on digital health technologies shows promise in transforming HF management by taking proactive measures based on the sensing of hemodynamic congestion. These new technologies have improved the individuals' quality of life and reduced overall health care cost by improving the worsening symptoms and decreasing readmission. However, the cost-prohibitive nature of these digital technologies precludes their usage in the large patient population affected by HF, both in the US and around the world. To overcome this limitation and to make these technologies broadly accessible, the work presented in this dissertation aims to pave the way toward an inexpensive, wearable cardiovascular hemodynamic monitoring system that can provide reliable information to clinicians to remotely monitor the patient population in a hemodynamically-guided HF management system.

We began this dissertation by comparing different wearable sensing modalities to track changes in cardiac contractility via estimation of PEP, during baseline and exercise recovery in a healthy population dataset. For the first time, we have presented that a gyroscope-based SCG sensor provided more relevant information regarding PEP compared to an accelerometer-based SCG sensor. We further presented our argument on the difficulty of using these biomedical signals in a population-level model due to the inter-subject variability of these signals and how extracting general time, frequency, and amplitude features and developing advanced machine learning regression models to estimate relevant and reliable hemodynamic features can be used to overcome these difficulties.

We further validated our custom-built wearable patch to record cardioelectromechanical signals (ECG and SCG) and signal processing and machine learning technologies in patients with HF during two clinical gold-standard procedures, which showcases the potential of using this sensing modalities and data analysis algorithm in helping a real-world patient population. For the first validation, we have validated our sensor and analysis algorithm during the CPX test in patients with HF, which is a gold-standard clinical procedure to stratify risks associated with HF and facilitate advanced heart therapy recommendations. Our method was accurate in estimating instantaneous VO_2 throughout these procedures and in predicting the outcome of the CPX test in a separate independent validation set, using the wearable signals alone. Doing so has opened up newer possibilities in longitudinal monitoring of cardiopulmonary health in patients with HF in their everyday life conditions during exercise and daily activities. We further translated these methodologies in tracking VO_2 in a minimally controlled walking activity, in a healthy population dataset, which showcases the promise of this methodology in cardiopulmonary health monitoring for both healthy individuals and patients with HF.

For the second validation study, we have validated our sensor and analysis algorithm in tracking changes in pulmonary artery pressure and pulmonary capillary wedge pressure during the RHC procedure, which is a gold-standard clinical procedure to monitor pulmonary congestion and increased filling pressure of the heart in patients with HF. Tracking changes in congestion (via tracking pulmonary artery pressure and lung fluid content) has already shown efficacy in reducing rehospitalization in patients with HF in hemodynamically-guided treatment methods using CardioMEMS and ReDS system. Our result of reliably tracking the changes in pulmonary congestion (via tracking changes in PAMP and PCWMP) has shown the efficacy of this noninvasive low-cost wearable sensor to monitor the pulmonary congestion in patients with HF in a clinical setting and has opened the possibility of similar tracking in an outpatient HF management. The possible outpatient HF management can track the worsening HF condition and help the clinicians to take proactive measures in remote HF management with the help of the SCG-based sensors.

With all three major contributions of this work, we establish the possibilities of using SCG-based wearable sensing, signal processing, and machine learning algorithms to monitor patients with HF during exercise and daily-life environments. The methodologies presented here have the potential to yield an accessible and affordable HF management system that the clinicians and caregivers can leverage for this large patient population.

7.2 Future Directions

Various potential future endeavors can stem from the research presented here. All three major works presented here were carried out mainly in a controlled laboratory or clinical environment, and a follow-up study was carried out in a minimally controlled outdoor setting. Future work should take these initial findings to test them in more everyday life scenarios to quantify if the wearable sensing system and analysis algorithm can be used in monitoring cardiovascular and pulmonary health in daily living activities (e.g., household chores, different forms of activities and exercises, etc.), where signal quality and both inter- and intra-subject variability may pose challenges in using these signals to extract relevant information from them. This is a necessary step towards true ubiquitous remote home monitoring of the patients with HF. Additionally, most of the patients with HF in this work were HFrEF. Future work should include more patients with HFpEF, cardiomyopathy, and other CVDs to analyze how this sensing system and the presented models can generalize in a diversified data set. Moreover, we have mostly focused on remote monitoring in this work. The work also has potential application in inpatient decision making using these wearable sensing modalities. Future work should investigate incorporating these sensing modalities in an intensive care unit (ICU), for inpatient management, and for disease progression monitoring.

The models and algorithms developed in this works were accurate in tracking changes in cardiac contractility, oxygen uptake, and changes in pulmonary congestion. Similar models and algorithm can be extended, perhaps through adding other sensing modalities, into estimating other key hemodynamic parameters, such as LVET, SV, CO, VE, VCO_2, pressures in other intra-cardiac and pulmonary chambers.

Though we have shown the accuracy of these sensing systems and advanced machine learning algorithms in monitoring hemodynamics with patients with HF and healthy subjects only, we can translate a similar approach to extract relevant information for patients with other chronic conditions, such as tracking cardiotoxicity due to cancer treatments in cancer survivors and cancer patients undergoing treatments, tracking cardiovascular health with neurological conditions. Lastly, though these sensing modalities have been researched and explored for decades, much is still unknown about the origin and pathophysiologically driven variations of these signals. Future work should investigate inter-subject variability and effects of different underlying cardiovascular and respiratory conditions on these signals in a mathematical framework or through finite element method modeling to understand the changes in the SCG signals we would expect from person to person due to difference in BMI, gender, and underlying disease conditions. This can, in turn, help us to use this sensing modality in a population-level model for the large number of patient populations affected by CVDs and other chronic health conditions.

REFERENCES

[1] U. D. of Health, H. Services, *et al.*, “Global health and aging,” *Washington, DC, USA: National Institute on Aging, National Institutes of Health*, 2011.

[2] J. Xu, K. D. Kochanek, S. L. Murphy, and B. Tejada-Vera, “Deaths: Final data for 2014,” 2016.

[3] P. A. Heidenreich, J. G. Trogdon, O. A. Khavjou, J. Butler, K. Dracup, M. D. Ezekowitz, E. A. Finkelstein, Y. Hong, S. C. Johnston, A. Khera, *et al.*, “Forecasting the future of cardiovascular disease in the united states: A policy statement from the american heart association,” *Circulation*, vol. 123, no. 8, pp. 933–944, 2011.

[4] V. L. Roger, A. S. Go, D. M. Lloyd-Jones, R. J. Adams, J. D. Berry, T. M. Brown, M. R. Carnethon, S. Dai, G. De Simone, E. S. Ford, *et al.*, “Heart disease and stroke statistics—2011 update: A report from the american heart association,” *Circulation*, vol. 123, no. 4, e18–e209, 2011.

[5] R. B. Zuckerman, S. H. Sheingold, E. J. Orav, J. Ruhter, and A. M. Epstein, “Readmissions, observation, and the hospital readmissions reduction program,” *New England Journal of Medicine*, vol. 374, no. 16, pp. 1543–1551, 2016.

[6] E. J. Benjamin, M. J. Blaha, S. E. Chiuve, M. Cushman, S. R. Das, R. Deo, S. D. De Ferranti, J. Floyd, M. Fornage, C. Gillespie, *et al.*, “Heart disease and stroke statistics—2017 update,” 2017.

[7] A. L. Bui, T. B. Horwich, and G. C. Fonarow, “Epidemiology and risk profile of heart failure,” *Nature Reviews Cardiology*, vol. 8, no. 1, p. 30, 2011.

[8] K. Dharmarajan, Y. Wang, Z. Lin, S.-L. T. Normand, J. S. Ross, L. I. Horwitz, N. R. Desai, L. G. Suter, E. E. Drye, S. M. Bernheim, *et al.*, “Association of changing hospital readmission rates with mortality rates after hospital discharge,” *Jama*, vol. 318, no. 3, pp. 270–278, 2017.

[9] A. Gupta and G. C. Fonarow, “The hospital readmissions reduction program—learning from failure of a healthcare policy,” *European journal of heart failure*, vol. 20, no. 8, pp. 1169–1174, 2018.

[10] A. Finkelstein, A. Zhou, S. Taubman, and J. Doyle, “Health care hotspotting—a randomized, controlled trial,” *New England Journal of Medicine*, vol. 382, no. 2, pp. 152–162, 2020.

[11] M. K. Ong, P. S. Romano, S. Edgington, H. U. Aronow, A. D. Auerbach, J. T. Black, T. De Marco, J. J. Escarce, L. S. Evangelista, B. Hanna, *et al.*, "Effectiveness of remote patient monitoring after discharge of hospitalized patients with heart failure: The better effectiveness after transition–heart failure (beat-hf) randomized clinical trial," *JAMA internal medicine*, vol. 176, no. 3, pp. 310–318, 2016.

[12] M. Shah, R. Zimmer, M. Kollefrath, and R. Khandwalla, "Digital technologies in heart failure management," *Current Cardiovascular Risk Reports*, vol. 14, no. 8, pp. 1–8, 2020.

[13] A. L. Bui and G. C. Fonarow, "Home monitoring for heart failure management," *Journal of the American College of Cardiology*, vol. 59, no. 2, pp. 97–104, 2012.

[14] S. I. Chaudhry, Y. Wang, J. Concato, T. M. Gill, and H. M. Krumholz, "Patterns of weight change preceding hospitalization for heart failure," *Circulation*, vol. 116, no. 14, pp. 1549–1554, 2007.

[15] W. T. Abraham, S. Compton, G. Haas, B. Foreman, R. C. Canby, R. Fishel, S. McRae, G. B. Toledo, S. Sarkar, and D. A. Hettrick, "Intrathoracic impedance vs daily weight monitoring for predicting worsening heart failure events: Results of the fluid accumulation status trial (fast)," *Congestive Heart Failure*, vol. 17, no. 2, pp. 51–55, 2011.

[16] C.-M. Yu, L. Wang, E. Chau, R. H.-W. Chan, S.-L. Kong, M.-O. Tang, J. Christensen, R. W. Stadler, and C.-P. Lau, "Intrathoracic impedance monitoring in patients with heart failure: Correlation with fluid status and feasibility of early warning preceding hospitalization," *Circulation*, vol. 112, no. 6, pp. 841–848, 2005.

[17] M. Packer, W. T. Abraham, M. R. Mehra, C. W. Yancy, C. E. Lawless, J. E. Mitchell, F. W. Smart, R. Bijou, C. M. O'Connor, and B. M. Massie, "Utility of impedance cardiography for the identification of short-term risk of clinical decompensation in stable patients with chronic heart failure," *Journal of the American College of Cardiology*, vol. 47, no. 11, pp. 2245–2252, 2006.

[18] G. M. Felker, T. Ahmad, K. J. Anstrom, K. F. Adams, L. S. Cooper, J. A. Ezekowitz, M. Fiuzat, N. Houston-Miller, J. L. Januzzi, and E. S. Leifer, "Rationale and design of the guide-it study: Guiding evidence based therapy using biomarker intensified treatment in heart failure," *JACC: Heart Failure*, vol. 2, no. 5, pp. 457–465, 2014.

[19] W. T. Abraham, L. W. Stevenson, R. C. Bourge, J. A. Lindenfeld, J. G. Bauman, and P. B. Adamson, "Sustained efficacy of pulmonary artery pressure to guide adjustment of chronic heart failure therapy: Complete follow-up results from the champion randomised trial," *The Lancet*, vol. 387, no. 10017, pp. 453–461, 2016.

[20] R. C. Bourge, W. T. Abraham, P. B. Adamson, M. F. Aaron, J. M. Aranda, A. Magalski, M. R. Zile, A. L. Smith, F. W. Smart, and M. A. O'Shaughnessy, "Randomized controlled trial of an implantable continuous hemodynamic monitor in patients with advanced heart failure: The compass-hf study," *Journal of the American College of Cardiology*, vol. 51, no. 11, pp. 1073–1079, 2008.

[21] J. Ritzema, I. C. Melton, A. M. Richards, I. G. Crozier, C. Frampton, R. N. Doughty, J. Whiting, S. Kar, N. Eigler, and H. Krum, "Direct left atrial pressure monitoring in ambulatory heart failure patients: Initial experience with a new permanent implantable device," *Circulation*, vol. 116, no. 25, pp. 2952–2959, 2007.

[22] O. Amir, T. Ben-Gal, J. M. Weinstein, J. Schliamser, D. Burkhoff, A. Abbo, and W. T. Abraham, "Evaluation of remote dielectric sensing (reds) technology-guided therapy for decreasing heart failure re-hospitalizations," *International journal of cardiology*, vol. 240, pp. 279–284, 2017.

[23] O. T. Inan, M. B. Pouyan, A. Q. Javaid, S. Dowling, M. Etemadi, A. Dorier, J. A. Heller, A. O. Bicen, S. Roy, T. D. Marco, and L. Klein, "Novel wearable seismocardiography and machine learning algorithms can assess clinical status of heart failure patients," *Circulation: Heart Failure*, 2017 (In Press).

[24] W. T. Abraham, P. B. Adamson, R. C. Bourge, M. F. Aaron, M. R. Costanzo, L. W. Stevenson, W. Strickland, S. Neelagaru, N. Raval, S. Krueger, S. Weiner, D. Shavelle, B. Jeffries, and J. S. Yadav, "Wireless pulmonary artery haemodynamic monitoring in chronic heart failure: A randomised controlled trial," *The Lancet*, vol. 377, no. 9766, pp. 658–666, 2011.

[25] P. B. Adamson, "Pathophysiology of the transition from chronic compensated and acute decompensated heart failure: New insights from continuous monitoring devices," *Current heart failure reports*, vol. 6, no. 4, p. 287, 2009.

[26] O. Amir, D. Rappaport, B. Zafrir, and W. T. Abraham, "A novel approach to monitoring pulmonary congestion in heart failure: Initial animal and clinical experiences using remote dielectric sensing technology," *Congestive Heart Failure*, vol. 19, no. 3, pp. 149–155, 2013.

[27] W. T. Abraham, S. Anker, D. Burkhoff, J. Cleland, E. Gorodeski, T. Jaarsma, R. Small, J. Lindenfeld, A. Miller, S. Ogenstad, *et al.*, "Primary results of the sensible medical innovations lung fluid status monitor allows reducing readmission rate of heart failure patients (smile) trial," *Journal of Cardiac Failure*, vol. 25, no. 11, p. 938, 2019.

[28] D. Bensimhon, D. McLean, P. Chase, D. Wood, V. Garman, and L. Curran, "Readiness for discharge of heart failure patients based on reds lung fluid measurement," *Journal of Cardiac Failure*, vol. 23, no. 8, S66, 2017.

[29] D. B. Newlin and R. W. Levenson, "Pre-ejection period: Measuring beta-adrenergic influences upon the heart," *Psychophysiology*, vol. 16, no. 6, pp. 546–552, 1979.

[30] R. C. Talley, J. F. Meyer, and J. L. McNay, "Evaluation of the pre-ejection period as an estimate of myocardial contractility in dogs," *The American journal of cardiology*, vol. 27, no. 4, pp. 384–391, 1971.

[31] A. M. Weissler, W. S. Harris, and C. D. Schoenfeld, "Systolic time intervals in heart failure in man," *Circulation*, vol. 37, no. 2, pp. 149–159, 1968.

[32] S Hassan and P Turner, "Systolic time intervals: A review of the method in the non-invasive investigation of cardiac function in health, disease and clinical pharmacology.," *Postgraduate Medical Journal*, vol. 59, no. 693, pp. 423–434, 1983.

[33] E. Braunwald, "Heart failure," *JACC: Heart Failure*, vol. 1, no. 1, pp. 1–20, 2013.

[34] W. A. Gattis, C. M. O'Connor, D. S. Gallup, V. Hasselblad, and M. Gheorghiade, "Predischarge initiation of carvedilol in patients hospitalized for decompensated heart failure: Results of the initiation management predischarge: Process for assessment of carvedilol therapy in heart failure (impact-hf) trial," *Journal of the American College of Cardiology*, vol. 43, no. 9, pp. 1534–1541, 2004.

[35] M. R. Zile, T. D. Bennett, M. J. S. St, Y. K. Cho, P. B. Adamson, M. F. Aaron, J. J. Aranda, W. T. Abraham, F. W. Smart, and L. W. Stevenson, "Transition from chronic compensated to acute decompensated heart failure: Pathophysiological insights obtained from continuous monitoring of intracardiac pressures," *Circulation*, vol. 118, no. 14, pp. 1433–1441, 2008.

[36] P. B. Adamson, A. Magalski, F. Braunschweig, M. Böhm, D. Reynolds, D. Steinhaus, A. Luby, C. Linde, L. Ryden, and B. Cremers, "Ongoing right ventricular hemodynamics in heart failure: Clinical value of measurements derived from an implantable monitoring system," *Journal of the American College of Cardiology*, vol. 41, no. 4, pp. 565–571, 2003.

[37] *Difference between pulmonary and systemic circulation*, `https://difference.guru/difference-between-pulmonary-and-systemic-circulation/`, Updated: 2019-05-28.

[38] D. Dias and J. Paulo Silva Cunha, "Wearable health devices—vital sign monitoring, systems and technologies," *Sensors*, vol. 18, no. 8, p. 2414, 2018.

[39] O. T. Inan, P.-F. Migeotte, K.-S. Park, M. Etemadi, K. Tavakolian, R. Casanella, J. Zanetti, J. Tank, I. Funtova, and G. K. Prisk, "Ballistocardiography and seismocardiography: A review of recent advances," *IEEE journal of biomedical and health informatics*, vol. 19, no. 4, pp. 1414–1427, 2015.

[40] D. E. Becker, “Fundamentals of electrocardiography interpretation,” *Anesthesia progress*, vol. 53, no. 2, pp. 53–64, 2006.

[41] S. R. Steinhubl, J. Waalen, A. M. Edwards, L. M. Ariniello, R. R. Mehta, G. S. Ebner, C. Carter, K. Baca-Motes, E. Felicione, and T. Sarich, “Effect of a home-based wearable continuous ecg monitoring patch on detection of undiagnosed atrial fibrillation: The mstops randomized clinical trial,” *Jama*, vol. 320, no. 2, pp. 146–155, 2018.

[42] D. M. Levine, K. Ouchi, B. Blanchfield, K. Diamond, A. Licurse, C. T. Pu, and J. L. Schnipper, “Hospital-level care at home for acutely ill adults: A pilot randomized controlled trial,” *Journal of general internal medicine*, vol. 33, no. 5, pp. 729–736, 2018.

[43] R. Patterson, “Fundamentals of impedance cardiography,” *IEEE Engineering in Medicine and Biology magazine*, vol. 8, no. 1, pp. 35–38, 1989.

[44] A. Sherwood, M. T. Allen, J. Fahrenberg, R. M. Kelsey, W. R. Lovallo, and L. J. Van Doornen, “Methodological guidelines for impedance cardiography,” *Psychophysiology*, vol. 27, no. 1, pp. 1–23, 1990.

[45] P. Carvalho, R. P. Paiva, J. Henriques, M. Antunes, I. Quintal, and J. Muehlsteff, “Robust characteristic points for icg-definition and comparative analysis.,” in *BIOSIGNALS*, 2011, pp. 161–168.

[46] K. Tavakolian, “Systolic time intervals and new measurement methods,” *Cardiovascular engineering and technology*, vol. 7, no. 2, pp. 118–125, 2016.

[47] P. Kh Dehkordi, F. Khosrow-Khavar, M. Di Rienzo, O. T. Inan, S. E. Schmidt, A. Blaber, K. Sørensen, J. J. Struijk, V. Zakeri, P. Lombardi, *et al.*, “Comparison of different methods for estimating cardiac timings: A comprehensive multimodal echocardiography investigation,” *Frontiers in physiology*, vol. 10, p. 1057, 2019.

[48] B. Bozhenko, “Seismocardiography–a new method in the study of functional conditions of the heart,” *Terapevticheskii arkhiv*, vol. 33, p. 55, 1961.

[49] J. M. Zanetti and D. M. Salerno, “Seismocardiography: A technique for recording precordial acceleration,” in *Computer-Based Medical Systems-Proceedings of the Fourth Annual IEEE Symposium*, IEEE Computer Society, 1991, pp. 4–5.

[50] R. S. Crow, P. Hannan, D. Jacobs, L. Hedquist, and D. M. Salerno, “Relationship between seismocardiogram and echocardiogram for events in the cardiac cycle,” *American journal of noninvasive cardiology*, vol. 8, pp. 39–46, 1994.

[51] K. Tavakolian, “Characterization and analysis of seismocardiogram for estimation of hemodynamic parameters,” Thesis, 2010.

[52] K. Sørensen, S. E. Schmidt, A. S. Jensen, P. Søgaard, and J. J. Struijk, “Definition of fiducial points in the normal seismocardiogram,” *Scientific reports*, vol. 8, no. 1, pp. 1–11, 2018.

[53] M Di Rienzo, E Vaini, P Castiglioni, G Merati, P Meriggi, G Parati, A Faini, and F Rizzo, “Wearable seismocardiography: Towards a beat-by-beat assessment of cardiac mechanics in ambulant subjects,” *Autonomic Neuroscience*, vol. 178, no. 1, pp. 50–59, 2013.

[54] M Becker, A. Roehl, U Siekmann, A Koch, M de la Fuente, R Roissant, K Radermacher, N Marx, and M Hein, “Simplified detection of myocardial ischemia by seismocardiography,” *Herz*, vol. 39, no. 5, pp. 586–592, 2014.

[55] D. M. Salerno and J. Zanetti, “Seismocardiography for monitoring changes in left ventricular function during ischemia,” *Chest*, vol. 100, no. 4, pp. 991–993, 1991.

[56] K. Tavakolian, G. A. Dumont, G. Houlton, and A. P. Blaber, “Precordial vibrations provide noninvasive detection of early-stage hemorrhage,” *Shock*, vol. 41, no. 2, pp. 91–96, 2014.

[57] J. M. Zanetti and K. Tavakolian, “Seismocardiography: Past, present and future,” in *2013 35th annual international conference of the IEEE engineering in medicine and biology society (EMBC)*, IEEE, 2013, pp. 7004–7007.

[58] A. Taebi, B. E. Solar, A. J. Bomar, R. H. Sandler, and H. A. Mansy, “Recent advances in seismocardiography,” *Vibration*, vol. 2, no. 1, pp. 64–86, 2019.

[59] P.-F. Migeotte, V. Mucci, Q. Delière, L. Lejeune, and P. van de Borne, “Multidimensional kineticardiography a new approach for wearable cardiac monitoring through body acceleration recordings,” in *XIV Mediterranean Conference on Medical and Biological Engineering and Computing 2016*, Springer, pp. 1125–1130.

[60] M. J. Tadi, E. Lehtonen, A. Saraste, J. Tuominen, J. Koskinen, M. Teräs, J. Airaksinen, M. Pänkäälä, and T. Koivisto, “Gyrocardiography: A new non-invasive monitoring method for the assessment of cardiac mechanics and the estimation of hemodynamic variables,” *Scientific Reports*, vol. 7, no. 1, p. 6823, 2017.

[61] D. M. Salerno, J. M. Zanetti, L. A. Green, M. R. Mooney, J. D. Madison, and R. A. Van Tassel, “Seismocardiographic changes associated with obstruction of coronary blood flow during balloon angioplasty,” *The American journal of cardiology*, vol. 68, no. 2, pp. 201–207, 1991.

[62] P. K. Jain, A. K. Tiwari, and V. S. Chourasia, "Performance analysis of seismocardiography for heart sound signal recording in noisy scenarios," *Journal of medical engineering & technology*, vol. 40, no. 3, pp. 106–118, 2016.

[63] I. Starr, A. Rawson, H. Schroeder, and N. Joseph, "Studies on the estimation of cardiac ouptut in man, and of abnormalities in cardiac function, from the heart's recoil and the blood's impacts; the ballistocardiogram," *American Journal of Physiology-Legacy Content*, vol. 127, no. 1, pp. 1–28, 1939.

[64] J. Gordon, "Certain molar movements of the human body produced by the circulation of the blood," *Journal of anatomy and physiology*, vol. 11, no. Pt 3, p. 533, 1877.

[65] O. Inan, M Etemadi, R. Wiard, L Giovangrandi, and G. Kovacs, "Robust ballistocardiogram acquisition for home monitoring," *Physiological measurement*, vol. 30, no. 2, p. 169, 2009.

[66] N. J. Conn, K. Q. Schwarz, and D. A. Borkholder, "In-home cardiovascular monitoring system for heart failure: Comparative study," *JMIR mHealth and uHealth*, vol. 7, no. 1, e12419, 2019.

[67] M. Etemadi, O. T. Inan, L. Giovangrandi, and G. T. Kovacs, "Rapid assessment of cardiac contractility on a home bathroom scale," *IEEE transactions on information technology in biomedicine*, vol. 15, no. 6, pp. 864–869, 2011.

[68] S. Morra, A. Hossein, D. Gorlier, J. Rabineau, M. Chaumont, P.-F. Migeotte, and P. van de Borne, "Ballistocardiography and seismocardiography detect hemodynamic changes during simulated obstructive apnea," *Physiological Measurement*, 2020.

[69] O. T. Inan, A. Q. Javaid, S. Dowling, H. Ashouri, M. Etemadi, J. A. Heller, S. Roy, and L. Klein, "Using ballistocardiography to monitor left ventricular function in heart failure patients," *Journal of Cardiac Failure*, vol. 22, no. 8, S45, 2016.

[70] H. Ashouri, L. Orlandic, and O. T. Inan, "Unobtrusive estimation of cardiac contractility and stroke volume changes using ballistocardiogram measurements on a high bandwidth force plate," *Sensors*, vol. 16, no. 6, p. 787, 2016.

[71] V. B. Aydemir, S. Nagesh, M. M. H. Shandhi, J. Fan, L. Klein, M. Etemadi, J. A. Heller, O. T. Inan, and J. M. Rehg, "Classification of decompensated heart failure from clinical and home ballistocardiography," *IEEE Transactions on Biomedical Engineering*, vol. 67, no. 5, pp. 1303–1313, 2019.

[72] R. Yi, M. Enayati, J. M. Keller, M. Popescu, and M. Skubic, "Non-invasive in-home sleep stage classification using a ballistocardiography bed sensor," in *2019*

IEEE EMBS International Conference on Biomedical & Health Informatics (BHI), IEEE, 2019, pp. 1–4.

[73] W. C. Hixson and D. E. Beischer, “Biotelemetry of the triaxial ballistocardiogram and electrocardiogram in a weightless environment,” NAVAL SCHOOL OF AVIATION MEDICINE PENSACOLA FLA, Tech. Rep., 1964.

[74] Baevskiĭ, “Ballistocardiographic studies during the 4th expedition on the saliut-6 orbital station,”

[75] G. Prisk, S Verhaeghe, D Padeken, H Hamacher, and M Paiva, “Three-dimensional ballistocardiography and respiratory motion in sustained microgravity,” *Aviation Space and Environmental Medicine*, vol. 72, no. 12, pp. 1067–1074, 2001.

[76] O. T. Inan, A. Dorier, S. Dowling, A. Q. Javaid, M. Etemadi, S. Roy, T. De Marco, and L. Klein, “Activity-contextualized wearable ballistocardiogram measurements can classify decompensated versus compensated heart failure patients,” *Circulation*, vol. 134, no. suppl_1, A17525–A17525, 2016.

[77] M. Etemadi, O. T. Inan, J. A. Heller, S. Hersek, L. Klein, and S. Roy, “A wearable patch to enable long-term monitoring of environmental, activity and hemodynamics variables,” *IEEE transactions on biomedical circuits and systems*, vol. 10, no. 2, pp. 280–288, 2016.

[78] C. Yang, S. Tang, and N. Tavassolian, “Utilizing gyroscopes towards the automatic annotation of seismocardiograms,” *Sensors*, vol. 16738, p. 1, 2016.

[79] C. Yang and N. Tavassolian, “Combined seismo-and gyro-cardiography: A more comprehensive evaluation of heart-induced chest vibrations,” *IEEE Journal of Biomedical and Health Informatics*, 2017.

[80] T. Chen and T. He, “Xgboost: Extreme gradient boosting,” *R package version 0.4-2*, 2015.

[81] T. Chen and C. Guestrin, “Xgboost: A scalable tree boosting system,” in *Proceedings of the 22nd acm sigkdd international conference on knowledge discovery and data mining*, ACM, 2016, pp. 785–794, ISBN: 1450342329.

[82] W. Kubicek, R. Patterson, and D. Witsoe, “Impedance cardiography as a noninvasive method of monitoring cardiac function and other parameters of the cardiovascular system,” *Annals of the New York Academy of Sciences*, vol. 170, no. 1, pp. 724–732, 1970.

[83] D. Serrano, R Lipka, D Younkin, P Hrudey, J Tovera, A Rahafrooz, M. Zaman, S Nagpal, I Jafri, and F Ayazi, “Environmentally-robust high-performance tri-axial

bulk acoustic wave gyroscopes," in *Position, Location and Navigation Symposium (PLANS), 2016 IEEE/ION*, IEEE, pp. 5–8, ISBN: 150902042X.

[84] A. Q. Javaid, H. Ashouri, A. Dorier, M. Etemadi, J. A. Heller, S. Roy, and O. T. Inan, "Quantifying and reducing motion artifacts in wearable seismocardiogram measurements during walking to assess left ventricular health," *IEEE Transactions on Biomedical Engineering*, vol. 64, no. 6, pp. 1277–1286, 2017.

[85] L. Sörnmo and P. Laguna, *Bioelectrical signal processing in cardiac and neurological applications*. Academic Press, 2005, vol. 8, ISBN: 0124375529.

[86] K. Tavakolian, A. P. Blaber, B. Ngai, and B. Kaminska, "Estimation of hemodynamic parameters from seismocardiogram," in *Computing in Cardiology, 2010*, IEEE, pp. 1055–1058, ISBN: 1424473195.

[87] P. Castiglioni, A. Faini, G. Parati, and M. Di Rienzo, "Wearable seismocardiography," in *Engineering in Medicine and Biology Society, 2007. EMBS 2007. 29th Annual International Conference of the IEEE*, IEEE, pp. 3954–3957, ISBN: 1424407877.

[88] K. Tavakolian, G. Portacio, N. R. Tamddondoust, G. Jahns, B. Ngai, G. A. Dumont, and A. P. Blaber, "Myocardial contractility: A seismocardiography approach," in *Engineering in Medicine and Biology Society (EMBC), 2012 Annual International Conference of the IEEE*, IEEE, pp. 3801–3804, ISBN: 1457717875.

[89] C. M. Bishop, *Pattern recognition and machine learning*. springer, 2006, ISBN: 0387310738.

[90] J. H. Friedman, "Greedy function approximation: A gradient boosting machine," *Annals of statistics*, pp. 1189–1232, 2001.

[91] T. G. Dietterich, "Ensemble learning," *The handbook of brain theory and neural networks*, vol. 2, pp. 110–125, 2002.

[92] A. Dupuy and R. M. Simon, "Critical review of published microarray studies for cancer outcome and guidelines on statistical analysis and reporting," *Journal of the National Cancer Institute*, vol. 99, no. 2, pp. 147–157, 2007.

[93] T. Hastie, R. Tibshirani, and J. Friedman, "The elements of statistical learning new york," *NY: Springer*, pp. 115–163, 2001.

[94] M. J. Tadi and J Mojtaba, "A new algorithm for segmentation of cardiac quiescent phases and cardiac time intervals using seismocardiography," in *Sixth International Conference on Graphic and Image Processing. International Society for Optics and Photonics*, 94432K–94432K.

[95] A. Q. Javaid, N. F. Fesmire, M. A. Weitnauer, and O. T. Inan, "Towards robust estimation of systolic time intervals using head-to-foot and dorso-ventral components of sternal acceleration signals," in *Wearable and Implantable Body Sensor Networks (BSN), 2015 IEEE 12th International Conference on*, IEEE, pp. 1–5, ISBN: 1467372013.

[96] R. Tibshirani, "Regression shrinkage and selection via the lasso," *Journal of the Royal Statistical Society. Series B (Methodological)*, pp. 267–288, 1996.

[97] L. v. d. Maaten and G. Hinton, "Visualizing data using t-sne," *Journal of Machine Learning Research*, vol. 9, no. Nov, pp. 2579–2605, 2008.

[98] B. Anchang, T. D. Hart, S. C. Bendall, P. Qiu, Z. Bjornson, M. Linderman, G. P. Nolan, and S. K. Plevritis, "Visualization and cellular hierarchy inference of single-cell data using spade," *Nature protocols*, vol. 11, no. 7, pp. 1264–1279, 2016.

[99] G. J. Berman, D. M. Choi, W. Bialek, and J. W. Shaevitz, "Mapping the stereotyped behaviour of freely moving fruit flies," *Journal of The Royal Society Interface*, vol. 11, no. 99, p. 20 140 672, 2014.

[100] F. I. Marcus, V. Sorrell, J. Zanetti, M. Bosnos, G. Baweja, D. Perlick, P. Ott, J. Indik, D. S. He, and K. Gear, "Accelerometer-derived time intervals during various pacing modes in patients with biventricular pacemakers: Comparison with normals," *Pacing and Clinical Electrophysiology*, vol. 30, no. 12, pp. 1476–1481, 2007.

[101] M. Markl, P. J. Kilner, and T. Ebbers, "Comprehensive 4d velocity mapping of the heart and great vessels by cardiovascular magnetic resonance," *Journal of Cardiovascular Magnetic Resonance*, vol. 13, no. 1, p. 7, 2011.

[102] H. G. Bogren and M. H. Buonocore, "4d magnetic resonance velocity mapping of blood flow patterns in the aorta in young vs. elderly normal subjects," *Journal of Magnetic Resonance Imaging: An Official Journal of the International Society for Magnetic Resonance in Medicine*, vol. 10, no. 5, pp. 861–869, 1999.

[103] U. Morbiducci, R. Ponzini, G. Rizzo, M. Cadioli, A. Esposito, F. De Cobelli, A. Del Maschio, F. M. Montevecchi, and A. Redaelli, "In vivo quantification of helical blood flow in human aorta by time-resolved three-dimensional cine phase contrast magnetic resonance imaging," *Annals of biomedical engineering*, vol. 37, no. 3, p. 516, 2009.

[104] R. Malhotra, K. Bakken, E. D'Elia, and G. D. Lewis, "Cardiopulmonary exercise testing in heart failure," *JACC: Heart Failure*, vol. 4, no. 8, pp. 607–616, 2016.

[105] J. Myers, R. Arena, L. P. Cahalin, V. Labate, and M. Guazzi, "Cardiopulmonary exercise testing in heart failure," *Current problems in cardiology*, vol. 40, no. 8, pp. 322–372, 2015.

[106] G. J. Balady, R. Arena, K. Sietsema, J. Myers, L. Coke, G. F. Fletcher, D. Forman, B. Franklin, M. Guazzi, and M. Gulati, "Clinician's guide to cardiopulmonary exercise testing in adults: A scientific statement from the american heart association," *Circulation*, vol. 122, no. 2, pp. 191–225, 2010.

[107] M. J. Haykowsky, C. R. Tomczak, J. M. Scott, D. I. Paterson, and D. W. Kitzman, "Determinants of exercise intolerance in patients with heart failure and reduced or preserved ejection fraction," *Journal of Applied Physiology*, vol. 119, no. 6, pp. 739–744, 2015.

[108] M. Guazzi, V. Adams, V. Conraads, M. Halle, A. Mezzani, L. Vanhees, R. Arena, G. F. Fletcher, D. E. Forman, D. W. Kitzman, C. J. Lavie, J. Myers, P. European Association for Cardiovascular, Rehabilitation, and A. American Heart, "Eacpr/aha scientific statement. clinical recommendations for cardiopulmonary exercise testing data assessment in specific patient populations," *Circulation*, vol. 126, no. 18, pp. 2261–2274, 2012.

[109] A. C. o. S. Medicine, *ACSM's guidelines for exercise testing and prescription*. Lippincott Williams Wilkins, 2013, ISBN: 1469826666.

[110] M. Guazzi, R. Arena, M. Halle, M. F. Piepoli, J. Myers, and C. J. Lavie, "2016 focused update: Clinical recommendations for cardiopulmonary exercise testing data assessment in specific patient populations," *Circulation*, vol. 133, no. 24, e694–e711, 2016.

[111] M. R. Mehra, C. E. Canter, M. M. Hannan, M. J. Semigran, P. A. Uber, D. A. Baran, L. Danziger-Isakov, J. K. Kirklin, R. Kirk, and S. S. Kushwaha, "The 2016 international society for heart lung transplantation listing criteria for heart transplantation: A 10-year update," *The Journal of Heart and Lung Transplantation*, vol. 35, no. 1, pp. 1–23, 2016.

[112] P. C. Mahalanobis, "On the generalized distance in statistics," National Institute of Science of India, 1936.

[113] L. Breiman, "Random forests," *Machine learning*, vol. 45, no. 1, pp. 5–32, 2001.

[114] M. Stone, "Cross-validatory choice and assessment of statistical predictions," *Journal of the Royal Statistical Society: Series B (Methodological)*, vol. 36, no. 2, pp. 111–133, 1974.

[115] S. Bot and A. Hollander, "The relationship between heart rate and oxygen uptake during non-steady state exercise," *Ergonomics*, vol. 43, no. 10, pp. 1578–1592, 2000.

[116] H. Loe, Rognmo, B. Saltin, and U. Wisløff, "Aerobic capacity reference data in 3816 healthy men and women 20–90 years," *PloS one*, vol. 8, no. 5, e64319, 2013.

[117] J. Platt, "Probabilistic outputs for support vector machines and comparisons to regularized likelihood methods," *Advances in large margin classifiers*, vol. 10, no. 3, pp. 61–74, 1999.

[118] C. Cortes and V. Vapnik, "Support-vector networks," *Machine learning*, vol. 20, no. 3, pp. 273–297, 1995.

[119] J. H. Friedman, "Greedy function approximation: A gradient boosting machine," *Annals of statistics*, pp. 1189–1232, 2001.

[120] C. Vella and R. Robergs, "A review of the stroke volume response to upright exercise in healthy subjects," *British journal of sports medicine*, vol. 39, no. 4, pp. 190–195, 2005.

[121] M. M. H. Shandhi, S. Hersek, J. Fan, E. Sander, T. De Marco, J. A. Heller, M. Etemadi, L. Klein, and O. T. Inan, "Wearable patch based estimation of oxygen uptake and assessment of clinical status during cardiopulmonary exercise testing in patients with heart failure," *Journal of Cardiac Failure*, 2020.

[122] A. J. Cook, B. Ng, G. D. Gargiulo, D. Hindmarsh, M. Pitney, T. Lehmann, and T. J. Hamilton, "Instantaneous vo2 from a wearable device," *Medical Engineering Physics*, vol. 52, pp. 41–48, 2018.

[123] A. De Brabandere, T. O. De Beeck, K. H. Schütte, W. Meert, B. Vanwanseele, and J. Davis, "Data fusion of body-worn accelerometers and heart rate to predict vo2max during submaximal running," *Plos one*, vol. 13, no. 6, 2018.

[124] H. Loe, Ø. Rognmo, B. Saltin, and U. Wisløff, "Aerobic capacity reference data in 3816 healthy men and women 20–90 years," *PloS one*, vol. 8, no. 5, e64319, 2013.

[125] B. Londeree and S. A. Ames, "Trend analysis of the% vo2 max-hr regression.," *Medicine and science in sports*, vol. 8, no. 2, pp. 123–125, 1976.

[126] B. Londeree, T. Thomas, G Ziogas, T. Smith, and Q. Zhang, "% vo2max versus% hrmax regressions for six modes of exercise.," *Medicine and science in sports and exercise*, vol. 27, no. 3, pp. 458–461, 1995.

[127] B. A. Franklin, J. Hodgson, and E. R. Buskirk, "Relationship between percent maximal o2 uptake and percent maximal heart rate in women," *Research quarterly for exercise and sport*, vol. 51, no. 4, pp. 616–624, 1980.

[128] P. B. Adamson, W. T. Abraham, R. C. Bourge, M. R. Costanzo, A. Hasan, C. Yadav, J. Henderson, P. Cowart, and L. W. Stevenson, "Wireless pulmonary artery pressure monitoring guides management to reduce decompensation in heart failure with preserved ejection fraction," *Circulation: Heart Failure*, vol. 7, no. 6, pp. 935–944, 2014.

[129] A. S. Desai, A. Bhimaraj, R. Bharmi, R. Jermyn, K. Bhatt, D. Shavelle, M. M. Redfield, R. Hull, J. Pelzel, K. Davis, *et al.*, "Ambulatory hemodynamic monitoring reduces heart failure hospitalizations in "real-world" clinical practice," *Journal of the American College of Cardiology*, vol. 69, no. 19, pp. 2357–2365, 2017.

[130] E. J. Benjamin, P. Muntner, A. Alonso, M. S. Bittencourt, C. W. Callaway, A. P. Carson, A. M. Chamberlain, A. R. Chang, S. Cheng, S. R. Das, *et al.*, "Heart disease and stroke statistics-2019 update a report from the american heart association," *Circulation*, 2019.

[131] M. M. H. Shandhi, B. Semiz, S. Hersek, N. Goller, F. Ayazi, and O. T. Inan, "Performance analysis of gyroscope and accelerometer sensors for seismocardiography-based wearable pre-ejection period estimation," *IEEE journal of biomedical and health informatics*, vol. 23, no. 6, pp. 2365–2374, 2019.

[132] B. C. Mani and S. S. Chaudhari, "Right heart cardiac catheterization," *StatPearls [Internet]*, 2020.

[133] H. Swan, W. Ganz, J. Forrester, H. Marcus, G. Diamond, and D. Chonette, "Catheterization of the heart in man with use of a flow-directed balloon-tipped catheter," *New England Journal of Medicine*, vol. 283, no. 9, pp. 447–451, 1970.

[134] S. Bangalore and D. L. Bhatt, "Right heart catheterization, coronary angiography, and percutaneous coronary intervention," *Circulation*, vol. 124, no. 17, e428–e433, 2011.

[135] J. Pan and W. J. Tompkins, "A real-time qrs detection algorithm," *IEEE transactions on biomedical engineering*, no. 3, pp. 230–236, 1985.

[136] A. L. Goldberger, L. A. Amaral, L. Glass, J. M. Hausdorff, P. C. Ivanov, R. G. Mark, J. E. Mietus, G. B. Moody, C.-K. Peng, and H. E. Stanley, "Physiobank, physiotoolkit, and physionet: Components of a new research resource for complex physiologic signals," *circulation*, vol. 101, no. 23, e215–e220, 2000.

[137] H. Sakoe and S. Chiba, “Dynamic programming algorithm optimization for spoken word recognition,” *IEEE transactions on acoustics, speech, and signal processing*, vol. 26, no. 1, pp. 43–49, 1978.

[138] A. E. Hoerl and R. W. Kennard, “Ridge regression: Biased estimation for nonorthogonal problems,” *Technometrics*, vol. 12, no. 1, pp. 55–67, 1970.

[139] M. Kudo and J. Sklansky, “Comparison of algorithms that select features for pattern classifiers,” *Pattern recognition*, vol. 33, no. 1, pp. 25–41, 2000.

VITA

Md Mobashir Hasan Shandhi was born in Rajbari, Bangladesh, in October 1987. He received his B.S. degree in electrical and electronic engineering from Bangladesh University of Engineering and Technology, Bangladesh, in 2011, and his M.Sc. degree in electrical and computer engineering from the University of Utah, Salt Lake City, UT, USA. He is currently pursuing a Ph.D. degree in electrical and computer engineering at Georgia Institute of Technology, Atlanta, GA, USA.

He joined the Ph.D. program at Georgia Tech in 2016. From May 2016, he joined the Inan Research Lab supervised by Dr. Omer T. Inan. His primary research is in the area of wearable health care monitoring for patients with heart failure. His other research interests include biomedical sensing systems, signal processing, and machine learning to develop cardiovascular and neurological health monitoring systems for clinically relevant applications.